Interaction between Seabed Soil and Offshore Wind Turbine Foundations

Hansen, Nilas Mandrup

Publication date:
2012

Document Version
Publisher's PDF, also known as Version of record

Interaction between Seabed Soil and Offshore Wind Turbine Foundations

PhD Thesis

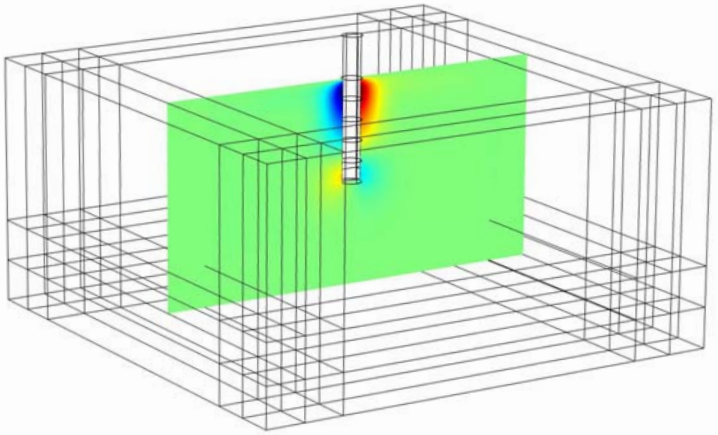

Nilas Mandrup Hansen
DCAMM Special Report No. S143
March 2012

DTU Mechanical Engineering
Department of Mechanical Engineering

Interaction between Seabed Soil and Offshore Wind Turbine Foundations

Nilas Mandrup Hansen

March 2012

Department of Mechanical Engineering
Section for Fluid Mechanics, Coastal and Maritime Engineering
Technical University of Denmark

Published in Denmark by
Technical University of Denmark

Section for Fluid Mechanics, Coastal and Maritime Engineering
Department of Mechanical Engineering
Technical University of Denmark
Nils Koppels Alle, Building 403, DK–2800 Kgs. Lyngby, Denmark
Phone +45 4525 1411, Telefax +45 4588 4325
E-mail: info.skk@mek.dtu.dk
WWW: http://www.mek.dtu.dk/

Publication Reference Data

Hansen, N. M.
Interaction between Seabed Soil and Offshore Wind Turbine Foundations
PhD Thesis
Technical University of Denmark, Department of Mechanical Engineering
DCAMM Special Report, no. S141
March, 2012
ISBN: 978-87-90416-80-5
Keywords: Pile foundation, soil reaction modulus, COMSOL, Biot's consolidation equations, Experimental work, Liquefaction

Preface

The present Ph.D. thesis is submitted as part of the requirement for obtaining the Ph.D. degree from the Technical University of Denmark. The Ph.D. has been conducted at the Department of Mechanical Engineering, Section for Fluid Mechanics, Coastal and Maritime Engineering. The main supervision was undertaken by professor B. Mutlu Sumer.

The present study is the result of contributions from many individuals. First and most importantly, I would like to thank Mutlu Sumer for sharing his experience and wisdom. It has been an educational experience.

I would also like to give special thanks to co-supervisor professor Jørgen Fredsøe for useful discussions during the project, to associate professor Ole Hededal and Ph.D. student Rasmus Tofte Klinkvort for assistance within the field of geotechnics, to professor Dong-Sheng Jeng at Dundee University for kindly providing the foundation of the numerical model, to Niels-Erik Ottesen Hansen for his comments in relation to offshore windfarms and to my colleague postdoc Niels Gjøl Jacobsen for many enlightening discussions during the entire project.

Also I would like to thank the entire staff at the Section for Fluid Mechanics, Coastal and Maritime Engineering. Special thanks are given to the staff at the sections experimental lab facility, including the former colleagues Henning Jespersen and Jan Larson for support during the experimental setup.

In addition, I would like to thank the Danish Council for Strategic Research (DFS)/Energy and Environment and the Technical University of Denmark for providing the financial support, making this Ph.D. study possible.

And finally, I would like to thank my wonderful wife and daughter for their patience and encouragement, especially when times were hard, throughout the past three years.

Kgs. Lyngby, March 2012

Nilas Mandrup Hansen

Abstract

Today, monopiles are widely used as foundation to support offshore wind turbines (OWT) in shallow waters. The stiffness of monopiles is one of the important design aspects. Field observations show that some monopiles, already installed in the field, behaves more stiff than predicted by the current design recommendations. The present study addresses the pile/seabed interaction problem, related to the stiffness of the monopile by means of a numerical model and experimental investigations.

The numerical model is a 3D model. COMSOL Multiphysics, a finite-element software, is used to calculate the soil response. The model is based on the Biot consolidation theory which involves a set of four equations, the first three equations describing the equilibrium conditions for a stress field, and the fourth one, the so-called storage equation, describing the conservation of mass of pore water with the seepage velocity given by Darcy's law (Sumer and Fredsøe, 2002, chap. 10). The constitutive equation for the soil considered in the model is the familiar stress-strain relationship for linear poro-elastic soils. The so-called no-slip boundary condition is adopted on the surface of the rocking pile.

The numerical model is validated against the laboratory experiments. The experimental setup includes a container (a circular tank with a diameter of 2 m and a height of 2.5 m), and a stainless steel model pile (with a diameter of 20 cm). Coarse sand ($d_{50} = 0.64$ mm) is used in the experiments.

Pore-water pressures, pile displacements and forces on the pile are measured in the experiments. The pore-water pressure is measured at 12 points over a mesh extending 0.75 m in the vertical and 0.10 m in the radial direction (the measurement points closest to the pile being at 2 cm from the edge of the pile), using Honeywell pressure transducers. The pile displacement is measured, using a conventional potentiometer, while the force is measured with a tension/compression S-Beam load cell.

The model, validated and tested, is used to calculate the soil response for a set of conditions, normally encountered in the field. The results are presented in terms of non-dimensional p-y curves, obtained from the numerical simulations. A parametric study is undertaken to observe the influence of various parameters on the latter.

The parametric study shows that, for a given displacement, y, the soil

resistance p, increases with increasing S, a non-dimensional parameter responsible for generation and further dissipation of the pore-water pressure. The parametric study also shows that, again for a given y, the soil resistance increases with decreasing bending stiffness of the pile, expressed in terms of a non-dimensional quantity s. Finally, the soil resistance increases, when the non-dimensional foundation depth decreases.

Resumé

I dag er monopæle brugt i vid udstrækning som fundament til offshore vindturbiner opført i lavt vand. Et vigtigt aspekt i monopælens design er dens stivhed. Feltmålinger har vist, at nogle monopæle, som allerede er installeret, opfører sig mere stift end forudset af den nuværende design anbefaling. Dette studie undersøger problematikken omkring pæl/havbunds interaktionen, relateret i forhold til stivheden af monopælen ved brug af en numerisk model og eksperimentelle undersøgelser.

Den numeriske model er en 3D model. COMSOL Multyphysics, som er et Finite Element program, er brugt til at beregne jordens respons. Modellen er baseret på Biot's konsoliderings teori, hvilke involverer et sæt af fire ligninger, hvor de tre første ligninger beskriver ligevægtsbetingelserne i et stress felt og den fjerde, den såkaldte storage ligning, beskriver bevarelsen af porevand, hvor porevandets gennemstrømningshastighed er beskrevet ved Darcy's lov (Sumer and Fredsøe, 2002, chap. 10). Den konstitutive ligning som er brugt til at beskrive jordens opførsel er det velkendte spændings-tøjningsforhold for en linear poro-elastisk jord. En no-slip betingelse er brugt som randbetingelse på overfladen af den rokkende pæl.

Den numeriske model er valideret imod eksperimentelle forsøg. Den eksperimentelle forsøgsopsætning inkluderer en beholder (en rund beholder med en diameter på 2 m og en højde 2.5 m), og et rustfrit stålrør (med en diameter på 20 cm). Groft sand ($d_{50} = 0.64$ mm) er blevet brugt i forsøgene.

Porevandtrykket, pælens flytning og kræfterne på pælen blev målt i forsøgene. Porevandtrykket er målt i 12 punkter over et net som udbreder sig 0.75 m i vertikal retning og 0.10 m i horisontal retning (det tætteste målepunkt var 2 cm fra pælens overflade), ved brug af Honeywell tryk transducere. Pælens flytning blev målt med et almindeligt potentiometer og kraften blev målt med en træk/tryk lastcelle.

Modellen, når den er valideret og testet, bruges derefter til at beregne jordens respons for en række betingelser, normalt mødt i felten. Resultaterne bliver præsenteret i form af nogle dimensionsløse $p-y$ kurver, udarbejdet på baggrund af de numeriske simuleringer. Et parameter studie udføres for at observere påvirkningen af forskellige parameter på de føromtalte $p-y$ kurver.

Parameterstudiet viser, at for en given flytning y, stiger jordens modstand p med stigende S, en dimensionsløs parameter ansvarlig for produktio-

nen og yderligere spredningen af porevandtrykket. Parameterstudiet viser yderligere, igen for en givet flytning y, at jordens modstand stiger med faldende bøjningsstivhed af pælen, udtrykt i form af en dimensionsløs størrelse s. Til sidst, jordens modstand øges, når den dimensionsløse funderingsdybde mindskes.

Contents

Nomenclature

The following nomenclature lists the symbols used in the report if not stated otherwise.

Greek Characters

α	Constant, typically $0.5 - 0.7$ for sand
β	Compressibility of the pore fluid
β	Slope of the failure line (Appendix E)
$\boldsymbol{\sigma}$	Stress vector
$\boldsymbol{\varepsilon}$	Strain vector
χ	Dimensionless parameter indication soil anisotropy and degree of saturation
δ	Boundary layer thickness (Sec. 4.1.2)
δ	Combined wave and soil parameter (Sec. 4.1.1)
ℓ	Length scale of diffusion (Sec. 5)
ϵ	Normal strain (Appendix D)
ϵ_p	Bending strain in the pile (Sec. 5)
η	Non-dimensional soil depth
γ	Specific weight of water
γ'	Submerged specific weight of the soil
γ_{liq}	Specific weight of the liquefied soil
γ_t	Total specific weight of the soil
$\gamma_{xy},\ \gamma_{yz},\ \gamma_{xz}$	Shear deformations
λ	Wave number

λ_L Lagrange multiplier (Sec. 5)

∇^2 Laplace operator

ν Poisson's ratio for the soil

ν_p Poisson's ratio for the pile

ω Angular frequency

ρ Soil density

ρ_p Pile density

ρ_w Density of water

σ Normal stress

σ' Effective stress

σ'_0 Mean initial effective stress

σ'_3 Confining pressure

σ_p Fluctuating component of pore-water pressure

σ'_x Effective normal stress in the x-direction

σ'_z Effective normal stress in the z-direction

$\sigma'_{3,ref}$ Reference confining pressure

$\sigma_x,\ \sigma_y,\ \sigma_z$ Normal stresses

τ Shear stress

$\tau_{xy},\ \tau_{yz},\ \tau_{xz}$ Shear stresses

θ Angle (Defined in Fig. 1.2)

$\tilde{\sigma}_x + \hat{\sigma}_x$ Effective normal stress i x-direction, normalized with the bed pore-water pressure

$\tilde{\sigma}_z + \hat{\sigma}_z$ Effective normal stress i z-direction, normalized with the bed pore-water pressure

ε Non-dimensional boundary layer thickness (Sec. 4.1.2)

ε_a Triaxial axial strain (Appendix E)

ε_p Triaxial volume strain (Appendix E)

ε_q Triaxial shear strain (Appendix E)

ε_r Triaxial radial strain (Appendix E)

$\varepsilon_x,\ \varepsilon_y,\ \varepsilon_z$ Strains

φ Soil friction angle

Roman Characters

$< >$ Used to denote ensemble averaged quantities

$< P >$ Ensemble averaged pore-water pressure (In excess of hydrostatic pressure)

C Elasticity matrix

$\overline{P}$ Period averaged pore-water pressure (In excess of hydrostatic pressure)

$\tilde{p} + \hat{p}$ Pore-water pressure normalized with the bed pore-water pressure

$_{i,\ j}$ subindex

A Constant $A = 0.9$ for cyclic loading (Sec. 5)

A Cross sectional area of permeameter

b A depth variable $b = 0.25, 0.50, 0.75, 1.00$

b Intersect between failure line and the abscissa (Appendix E)

c' Effective cohesion

$C_1,\ C_2,\ C_3$ Constants (Sec. 5)

C_H Hazen coefficient

C_n Non-dimensional coefficients

C_p Soil resistance in non-dimension form (Sec. 5)

C_u Uniformity coefficient

c_v Coefficient of consolidation

D Pile diameter

d Seabed depth in TC1

D_c Diffusion coefficient from the theory of diffusion and dispersion

D_r Relative density

d_s Specific gravity of the soil grains

d_{10} Grain size in which 10 % of the soil is finer

d_{50} Grain size in which 50 % of the soil is finer

d_{60} Grain size in which 60 % of the soil is finer

E Young's modulus of the soil

e Void ratio

e_d Foundation depth

E_p Young's modulus of the pile

e_x Load eccentricity (Sec. 5)

e_{liq} Void ratio of the liquefied soil

e_{max} maximum void ratio

e_{min} minimum void ratio

$E_{py,DNV}$ Soil reaction modulus from DNV (2004)

$E_{py,num}$ Soil reaction modulus from numerical model

E_{py} Reaction modulus for a pile under lateral loading (Sec. 5)

E_{ref} Reference Young's modulus for soil

E_{URL} Young's modulus for the soil (unloading/reloading) (Appendix E)

F Force excerted on pile head

f Source term (Sec. 5)

F_x Volume force in x-direction

F_y Volume force in y-direction

F_z Volume force in z-direction

G Shear modulus of the soil

g Acceleration of gravity

H Wave height (Sec. 5)

h Geometric head (Appendix B)

h Water depth

H_W Wave height in TC1

i	Imaginary number
I_p	Second area moment of inertia
k	Soil permeability
K'	Bulk modulus of elasticity of pore water
K_0	Coefficient of lateral earth pressure
k_T	Modulus of subgrade reaction (Sec. 5)
K_w	True bulk modulus of elasticity of water
L	Distance between pressure tappings
L_c	Critical length (Sec. 5)
L_s	Beam span
L_W	Wave length in TC1
M	Bending moment
m	Stiffness ratio
N	Normal force (Appendix D)
N	Number of periods
n	Soil porosity
$n_1,\ n_2,\ n_3$	Normal vector components
P	Pore-water pressure (In excess of hydrostatic pressure)
p	Soil resistance (Sec. 5)
p_0	pressure exerted on the seabed by waves
p_b	Amplitude of pressure exerted on the seabed by waves
P_r	Raw pore-water pressure
P_{max}	Maximum PWP when soil is liquefied
p_{ult}	Ultimate lateral soil resistance (Sec. 5)
Q	Lateral force exerted by waves (Sec. 5)
Q	Point load (Appendix D)
Q	Water discharge

q	Deviator stress (Appendix E)
q	Uniform load
r	Distance from pile wall
r_0	Pile radius
S	Spreading parameter (Sec. 5)
s	Strain parameter (Sec. 5)
S_r	Saturation degree
s_t	Total specific gravity of the sediment
T	Period of the rocking pile
t	Time
t	Total time of discharge (Appendix B)
T_W	Wave period in TC1
t_w	Wall thickness of the pile (Sec. 5)
u	Soil displacements in the x-direction
u_p	pile displacements in x-direction
v	Soil displacements in the y-direction
V_D	Pile head velocity
v_p	pile displacements in y-direction
W	Seabed width in TC1
w	Soil displacements in the z-direction
w_p	pile displacements in z-direction
x	x-coordinate
X_D	Displacement of the pile head
x_D	Amplitude of the pile head displacement
y	Distance from neutral axis (Appendix D)
y	Lateral displacement of the pile as function of soil depth (Sec. 5)
y	y-coordinate

y_s	Length scale
z	Distance below the soil surface (Sec. 5)
z	z-coordinate
z_R	Transition depth (Sec. 5)

Abbreviations

BCE	Biot consolidation equations
EWEA	European Wind Energy Association
FE	Finite element
HTI	Heat transfer interface
MCI	Mathematics coefficient form interface
OHVS	Offshore high voltage station
OWT	Offshore wind turbine
PDE	Partial differential equation
PWP	Pore-water pressure (in excess of hydrostatic pressure)
SMI	Solid mechanics interface
TC1	Test case 1

Chapter 1

Introduction

1.1 Statement of the Problem

Monopiles are presently designed according to the well-known p-y method adopted in most design recommendations, e.g. DNV (2004). It is rarely the ultimate lateral bearing capacity, which is the decisive factor in design of a monopile foundation. This may also be seen in the low failure rate of monopiles already placed in the field.

More importantly is the stiffness of the monopile foundation due to possible fatigue failure. Field observations have shown that some monopiles behaves more rigid than predicted by the current design recommendations. Therefore there is a need for better understanding of the pile / soil interaction problem and especially the influence of various soil parameters.

1.2 Motivation of the Problem

In January 2008 the European Commission published a "climate and energy package" which included the 20-20-20 targets. The targets were to cut the emission of greenhouse gases by 20 %, to cut the energy consumption by 20 % of projected 2020 levels and finally to increase the use of renewables to 20 % of total energy production by the year 2020 (European Commission, 2008).

In year 2000 the European offshore wind energy's share of the electricity demand was 0.0 %. In year 2009 the offshore wind contributed with 0.2 % of the European electricity demand. The European Wind Energy Association (EWEA) forecast that the share is to increase up to 4.3 % by year 2020 and 16.7 % by year 2030 (EWEA, 2009).

Today, several options exist for foundation of an offshore wind turbine (OWT). These are the gravity-based foundation, the monopile, the tripod

and the jacket type foundation. See e.g. Cuéllar (2011). A new OWT foundation may also be mentioned, namely the bucket type foundation (Ibsen and Liingaard, 2009). The monopile foundation is currently the preferred choice as OWT foundation, mainly due to low production cost.

Today, monopiles of approximately $5-6$ m in diameter have been installed in the North Sea. At Horns Rev II, the OWT foundations were 3.9 m in diameter and installed at a water depth up to 17 m. Going in deeper waters, the diameter of the piles may increase up to 7.5 m in order to fulfill the requirements for sufficient bearing capacity (Achmus *et al.*, 2009). Besides the requirement of sufficient bearing capacity, fatigue failure is also an important aspect. Here estimates of the accumulated pile head deflection and rotation, and the stiffness of the foundation are of vital importance.

Monopiles may in general be installed by one of the following three methods (DNV and Risø, 2001); 1) driving using pilling hammer where a ram is dropped on the head of the monopile, 2) driving using vibrators or 3) driving using drilling or excavation of seabed material. Common for all three driving methods are the maximum possible pile diameter, pile length and wall thickness. At present, the largest pile possible to install in the field, using pilling hammer method, due to limitations of driving equipment is around 6 m in diameter having a length of approximately 100 m and a wall thickness of approximately 120 mm. In addition, the transportation of the large pile diameter also implies difficulties.

Therefore there is a growing interest for better understanding of lateral loaded piles. The engineers need tools that can more accurately predict both the long term response of a lateral loaded pile as well as the short term response including the stiffness of the OWT pile foundation.

1.3 Existing work

Work on lateral loaded piles have been conducted during the last hundred years. Karl Terzaghi, who may be considered as the forefather of soil mechanics started some pioneering work on laterally loaded piles and introduced the coefficient of subgrade reaction used in the current design recommendations when deriving the $p-y$ curves.

The existing methods on the analysis of laterally loaded piles may be divided into following five groups; (1) the limit state method; (2) the subgrade reaction method; (3) the p-y method; (4) the elasticity method and (5); the Finite Element Method (Fan and Long, 2005). The limit state method will not be discussed in the content of the present work, since it is simply an equilibrium method between driving forces (lateral loads) and stabilizing forces

(passive soil resistance) as for instance in Broms (1964). Also the elasticity method will not be discussed.

The subgrade reaction method may also be termed the Winkler approach or the Beam on Elastic Foundation approach. It describes a method where the pile is assumed to be supported by a series of discrete springs, each spring having its own spring characteristics. The behavior of each spring is assumed linear and can be formulated as (Matlock and Reese, 1960),

$$p = E_{py} y \tag{1.1}$$

where p is the soil resistance in terms of force per unit length, y is the pile lateral deflection and E_{py} is termed the reaction modulus and represents the slope in the p-y curve. The reaction modulus E_{py} may be expressed as,

$$E_{py} = k_T z \tag{1.2}$$

where z is the distance below the soil surface and k_T is the coefficient of subgrade reaction, originally formulated by Terzaghi (1955). The p-y method is a further development of the subgrade reaction method, where the linear springs are replaced by a set of non-linear springs as in Reese *et al.* (1974).

The p-y method do has some shortcomings when used for design of OWT pile foundations. Among others, one of the shortcomings of the p-y method is that it has been based on data obtained from long slender flexible piles whereas piles installed in the field behaves more rigidly (Leblanc *et al.*, 2010). Despite the shortcomings, the p-y method currently represents the current state-of-the-art for design of monopiles in the offshore industry (Leblanc *et al.*, 2010). The p-y method has been adopted in the design recommendations for OWT foundations, e.g. in DNV (2004).

With the advancement of computers, finite elements models for the analysis of lateral loaded piles have gained more attention recent years. FE-models are considered as an effective tool for modelling important physics such as pile/soil interface, 3D boundary conditions and soil nonlinearity (Kim and Jeong, 2011). Without any claim of being complete, some work already conducted, related to the pile response from lateral loading are shortly presented below.

Randolph (1981) developed a 2D finite element model for the analysis of a lateral loaded pile. The soil was modelled as an elastic continuum and the pile was modelled as an elastic beam. Since the model was a 2D model, important physics such as 3D boundary conditions could not be captured. Yang and Jeremic (2002) developed a 3D FE-model where the soil was modelled as an elasto-plastic material. The yield surface of the sand was modelled with the Drucker-Prager yield surface and the pile was modelled as a linear-elastic

material. The results were used to compute a set of $p - y$ curves. The p-y curves were obtained from static one way loading tests. Others researchers, e.g Taha *et al.* (2009) modelled the soil as a Mohr-Coulomb elasto-plastic material. Kim and Jeong (2011) and Zania and Hededal (2011) considered the soil as a Mohr-Coulomb elasto-plastic material with the non-associated flow rule adopted. In Zania and Hededal (2011) rigid piles were considered and the effect of friction between the pile and soil surface was investigated. Common for the preceding works, are that the soil has been modelled as a material without voids, hence the pore-water pressure (PWP), in excess of hydrostatic pressure has been left out in the considerations. Therefore short term effects on the soil response have been left out in the preceding works.

Cuéllar (2011) give a review on research work conducted in relation to short term response arising from cyclic loading. In Cuéllar (2011) a numerical model with the capability of simulating the PWP in the soil during cyclic loading was developed. The model utilized the Biot's consolidation equations (Biot, 1941) to handle the PWP generation during cyclic loading. The model included a residual component to handle build-up of PWP, thus the model had provisions to estimate the liquefaction potential for piles under cyclic loading (see e.g. Sumer and Fredsøe (2002) for further description of the liquefaction phenomena.). The model also contained a set of constitutive equations used to describe the stress behavior of the soil from arbitrary imposed soil deformations. However in the work by Cuéllar (2011) the focus was on the soil susceptibility to liquefaction. Taiebat (1999) also developed a numerical model able of handling the PWP during cyclic loading. However the model was not validated against experimental test, nor was the numerical model used to evaluate the soil response in terms of p-y relationships.

1.4 The Niche

From the preceding review of existing work, it seems clear that numerical models are a viable tool to model laterally loaded piles which allows features, such as pile/soil interface, 3D boundary conditions and soil nonlinearity, to be considered. When modelling lateral loaded piles, the equations governing the soil behavior, are usually without a component describing the pore-water flow. The pile is exposed to a one-way loading, thus the dynamic effect from the pore-water flow in the voids of the soil skeleton, is neglected. Despite the lack of the pore-water flow, the models seems to perform well when comparing e.g the stiffness of the foundation, with field measurements.

When it comes to poro-elastic models, able to handle the pore-water during cyclic loading, focus appears to be on soil liquefaction rather than the stiffness of the pile. In addition, calibration and validation of the models rely

on measurements obtained from triaxial tests on soil specimens.

The niche, as it appears from the previous literature survey, is to obtain the soil response, for full-scale conditions, including the pore-water flow and soil stiffness by considering the soil as a linear poro-elastic material governed by the Biot's consolidation equations and to validate the model using data obtained in lab-scale experiments.

1.5 The Purpose

The purpose of the present study is to develop a numerical model simulating a cyclic lateral loaded pile in a seabed, where the voids in the soil skeleton are filled with water. The numerical model should be able to simulate field conditions. The model should be based on the Biot's consolidation equations capable of handling the PWP developing during the cyclic loading of the pile.

The model should be validated against lab-scale experiments performed under controlled conditions. Once the model is validated, it should be scaled to field conditions and soil properties normally encountered in the field, should be implemented.

The end-product of the present work, should be a parametric study, investigating the influence of various parameters on the soil resistance curves (p-y curves) describing the stiffness of the pile foundation. The soil resistance curves should be presented in terms of the non-dimensional quantities describing the pile / soil interaction.

1.6 Methodology and Terminology

1.6.1 Methodology

In the present work, a literature study on pile / soil interaction under influence of cyclic loading (Chap. 1) has been carried out. Common knowledge and background of the pile/soil interaction problem has been gained. Based on Biot's consolidation equations, a 3D numerical model, originally described in Jeng *et al.* (2010) is further developed and described (Chap. 2).

A series of experimental tests are performed in order to obtain data for model validation (Chap. 3). In the experimental test a model pile (20 cm in diameter) is placed in a container with sand. The model pile are then moved in a cyclic fashion in order to simulate the cyclic loading of a monopile. Two series of tests are performed. One test on coarse sand and one on coarse silt. The PWP is measured during the cyclic loading. The coarse sand experiment is used in the model validation exercise, while the coarse silt experiment is

for mostly academic purpose.

The numerical model is validated (Chap. 4) by 1) a simplified 2D model where the PWP under progressive waves from analytical solutions is compared with the output from the numerical model and 2) the numerical model is developed in 3D, and used to simulate the experimental test, and the PWP is compared.

Once the numerical model is validated, it is developed further, to simulated field conditions (Chap. 5). A set of non-dimensional parameters, governing the pile / soil interaction are developed. A parametric study is performed and based on the parametric study, a set on non-dimensional soil resistance curves are developed and the influence of the non-dimensional parameters are investigated.

1.6.2 Terminology

To ease the reader, this small section provides an overview of the terminology and definitions used throughout the report. In the present study an offshore *pile* foundation is investigated. Pile foundations offshore are normally termed monopile foundations. The pile foundation usually supports the tower of an offshore wind turbine (OWT). However the pile foundation may also be used to support other structures such as offshore high voltage structures (OHVS), e.g transformer stations. In the present report the wording *model pile* and *pile* will be used to denote the model pile used in the experimental tests and the pile used in the numerical simulations, respectively.

In a soil, where the voids between the soil grains are filled with water, the total stress will be composed of two parts, namely the contact stresses between the individual soil grains (effective stress) and the stresses from the pore-water. If the pore-water is still, the pore-water pressure (PWP) will be equal the hydrostatic pressure. However, throughout this report, the term PWP will be used to denote the pressure in the voids of the soil skeleton *in excess of hydrostatic pressure.*

Finally, throughout the report words such as *pile head*, *pile toe*, *pile length*, *foundation depth* and *load eccentricity* will be used. Fig. 1.1 and Fig. 1.2 gives a definition sketch of the terminology used.

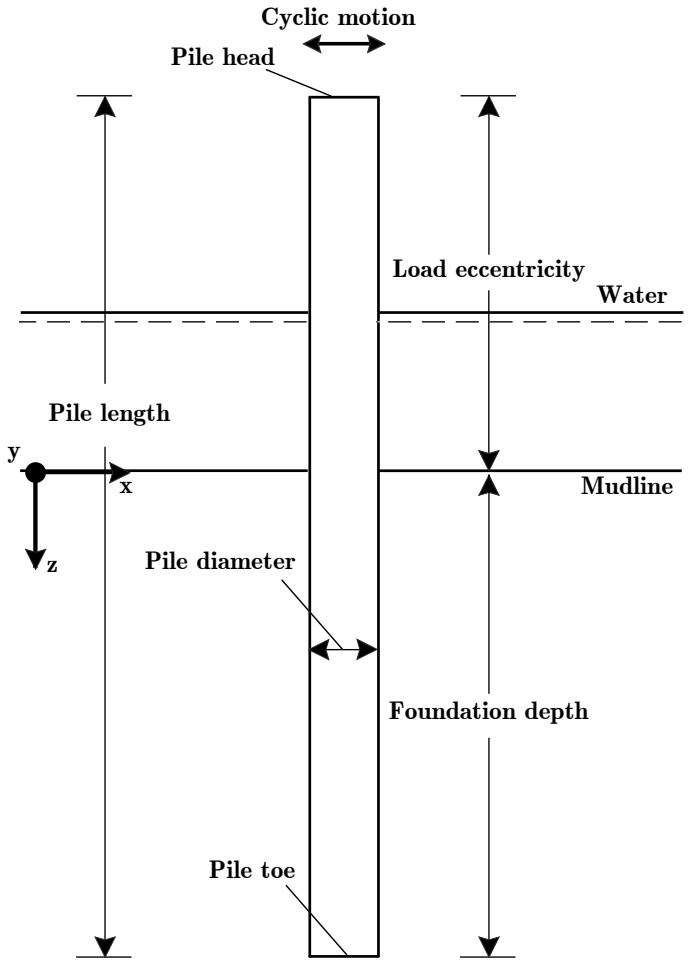

Figure 1.1: *Definition sketch of terminology used (side view).*

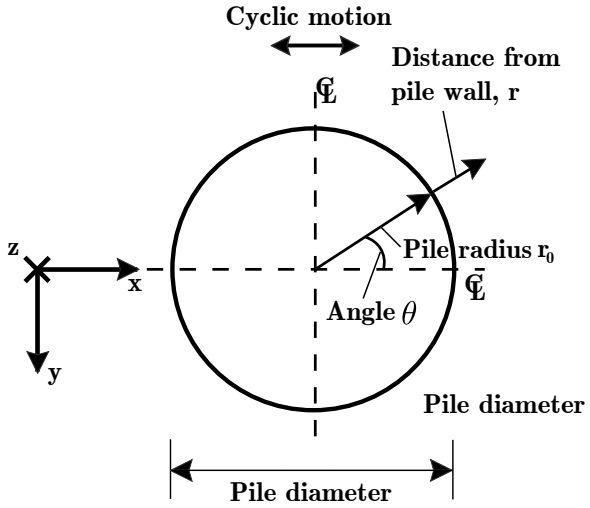

Figure 1.2: *Definition sketch of terminology used (Plan view).*

This page is intentionally left blank.

Chapter 2

Numerical model. Biot Equations

2.1 Introduction

This chapter will present the numerical model used in the present study. First the equations governing the soil response and the pile behavior are described. The boundary conditions are presented. Then the assumptions and the limitations of the numerical model are discussed and finally the implementation of the equations in the commercial software package COMSOL is presented.

The basis of the numerical model was originally developed by Jeng *et al.* (2010) and kindly provided during the present authors visit to the UK. A number of modifications have been made to the original model. Originally the numerical model included the Navier-Stokes equations to handle the water on top of the seabed. Also, the original model utilized an arbitrary Lagrangian-Eulerian moving mesh in order to resolve the free surface of the water. Both features are excluded in the present model.

Three sets of models were developed, all based on the same set of governing equations. One model, a 2D model, was used in a simple test case where the seabed response under a progressive wave was investigated. The test case was used to validate the solution to Biot's consolidation equations. A second model, simulating lab-scale dimensions was developed and validated against experiments. Finally a full-scale model was developed, based on the lab-scale model. In the full-scale model infinite elements were used to simulate the infinite extent of the soil.

2.2 Governing Equations

2.2.1 The Pile

Considering the pile as an elastic pile, its behavior is modelled by linear elasticity. The stress-strain relationships are given by Hooke's Law,

$$\boldsymbol{\sigma} = \mathsf{C}\boldsymbol{\varepsilon} \tag{2.1}$$

where $\boldsymbol{\sigma}$ is the stress vector defined as,

$$\boldsymbol{\sigma} = \begin{pmatrix} \sigma_x \\ \sigma_y \\ \sigma_z \\ \tau_{yz} \\ \tau_{xz} \\ \tau_{xy} \end{pmatrix} \tag{2.2}$$

where σ is the normal stresses, τ denotes the shear stresses and x, y and z refer to the three directions in the Cartesian coordinate system (see 1.1). $\boldsymbol{\varepsilon}$ is the strain vector,

$$\boldsymbol{\varepsilon} = \begin{pmatrix} \varepsilon_x \\ \varepsilon_y \\ \varepsilon_z \\ \varepsilon_{yz} \\ \varepsilon_{xz} \\ \varepsilon_{xy} \end{pmatrix} = \begin{pmatrix} \varepsilon_x \\ \varepsilon_y \\ \varepsilon_z \\ \gamma_{yz}/2 \\ \gamma_{xz}/2 \\ \gamma_{xy}/2 \end{pmatrix} \tag{2.3}$$

Here ε_x, ε_y and ε_z are the strains defined as,

$$\varepsilon_x = \frac{\partial u_p}{\partial x}, \quad \varepsilon_y = \frac{\partial v_p}{\partial y}, \quad \varepsilon_z = \frac{\partial w_p}{\partial z} \tag{2.4}$$

while γ_{xy}, γ_{yz} and γ_{xz} are the shear deformations defined as,

$$\gamma_{xy} = \frac{\partial v_p}{\partial x} + \frac{\partial u_p}{\partial y}, \quad \gamma_{yz} = \frac{\partial v_p}{\partial z} + \frac{\partial w_p}{\partial y}, \quad \gamma_{xz} = \frac{\partial u_p}{\partial z} + \frac{\partial w_p}{\partial x} \tag{2.5}$$

where u_p, v_p and w_p are the components of the pile displacement. For isotropic materials $\gamma_{xy} = \gamma_{yx}$, $\gamma_{yz} = \gamma_{zy}$ and $\gamma_{xz} = \gamma_{zx}$ because of symmetry in the elasticity matrix C. The elasticity matrix C in Eqn. 2.1 is defined as,

$$\mathsf{C} = \frac{E_p}{(1+\nu_p)(1-2\nu_p)} \begin{pmatrix} 1-\nu_p & \nu_p & \nu_p & 0 & 0 & 0 \\ \nu_p & 1-\nu_p & \nu_p & 0 & 0 & 0 \\ \nu_p & \nu_p & 1-\nu_p & 0 & 0 & 0 \\ 0 & 0 & 0 & \frac{1-2\nu_p}{2} & 0 & 0 \\ 0 & 0 & 0 & 0 & \frac{1-2\nu_p}{2} & 0 \\ 0 & 0 & 0 & 0 & 0 & \frac{1-2\nu_p}{2} \end{pmatrix} \tag{2.6}$$

for an isotropic material, where E_p and ν_p are the pile Young's modulus and Poisson's ratio respectively. The transient response of the pile, is govern by the equations of motion, namely,

$$\rho_p \frac{\partial^2 u_p}{\partial t^2} - \frac{\partial \sigma_x}{\partial x} - \frac{\partial \tau_{xy}}{\partial y} - \frac{\partial \tau_{xz}}{\partial z} = F_x \tag{2.7}$$

$$\rho_p \frac{\partial^2 v_p}{\partial t^2} - \frac{\partial \tau_{yx}}{\partial x} - \frac{\partial \sigma_y}{\partial y} - \frac{\partial \tau_{yz}}{\partial z} = F_y \tag{2.8}$$

$$\rho_p \frac{\partial^2 w_p}{\partial t^2} - \frac{\partial \tau_{zx}}{\partial x} - \frac{\partial \tau_{zy}}{\partial y} - \frac{\partial \sigma_z}{\partial z} = F_z \tag{2.9}$$

here ρ_p is the pile density and where F_x, F_y and F_z are the external volume force.

2.2.2 The Seabed

In the present study, the seabed response is assumed to be governed by the *Biot consolidation equations* (BCE),(Biot, 1941). The BCE have been applied for a variety of applications in which the soil response is sought under different types of loadings, see e.g. Ulker *et al.* (2012) or Jeng and Cheng (2000) for analysis of seabed instability under a caison breakwater or instability of a buried pipeline, respectively.

The BCE are based on a number of assumptions by Biot (1941).

1. The soil is an isotropic material,
2. Reversibility of stress-strain relations under final equilibrium conditions,
3. Linearity of stress-strain relations,
4. Small strains,
5. The pore-water is incompressible,
6. The pore-water may contain air bubbles,
7. The pore-water flows through the porous media according to Darcy's law.

When considering the soil as a poro-elastic material, the equations of equilibrium for the soil becomes (see Sumer and Fredsøe (2002) or Biot (1941) for a full derivation of the equilibrium equations.),

$$G\nabla^2 u + \frac{G}{1-2\nu}\frac{\partial \varepsilon}{\partial x} = \frac{\partial P}{\partial x} \tag{2.10}$$

$$G\nabla^2 v + \frac{G}{1-2\nu}\frac{\partial \varepsilon}{\partial y} = \frac{\partial P}{\partial y} \tag{2.11}$$

$$G\nabla^2 w + \frac{G}{1-2\nu}\frac{\partial \varepsilon}{\partial z} = \frac{\partial P}{\partial z} \tag{2.12}$$

where u, v and w are the soil displacements, G and ν are the elastic properties of the soil, namely the shear modulus of elasticity and the Poison ratio, P is the PWP, ∇^2 is the Laplacian operator and ε is the volume expansion,

$$\varepsilon = \frac{\partial u}{\partial x} + \frac{\partial v}{\partial y} + \frac{\partial w}{\partial z} \tag{2.13}$$

Eq. 2.10, 2.11, and 2.12 contains four unknown, namely the soil displacements u, v, w and the PWP P. Assuming that the flow of pore-water through the soil skeleton is governed by Darcy's law coupled with the conservation of mass of the pore-water, a fourth equation can be formulated as,

$$\frac{k}{\gamma}\nabla^2 P = \frac{n}{K'}\frac{\partial P}{\partial t} + \frac{\partial \varepsilon}{\partial t} \tag{2.14}$$

where k is the permeability of the soil, γ is the specific weight of the pore-water, n is the porosity and K' is the bulk modulus of the pore-water,

$$\frac{1}{K'} = \frac{1}{K_w} + \frac{1-S_r}{p_0} \tag{2.15}$$

where K_w is the true bulk modulus of water, S_r is the degree of saturation and p_0 is the absolute pore-water pressure and can be taken equal to the initial value of pressure (Sumer and Fredsøe, 2002). Eq. 2.14 apply for an isotropic material. The term $\frac{n}{K'}\frac{\partial P}{\partial t}$ in Eq. 2.14 represents the compressibility of the pore-water including the gas/air content in the water (Sumer and Fredsøe, 2002). The equations Eq. 2.10, 2.11, and 2.12 (constitutive equations) together with Eq. 2.14 (storage equation) are the Biot consolidation equations.

2.3 Boundary conditions

This section will present the boundary conditions implemented in the numerical models.

2.3.1 Soil in a confined Domain

In the lab-scale numerical model, the vertical walls, the slopes and the bottom of the tank (see Sec. 3) are modelled as impermeable smooth rigid walls. This implies that (1) the soil at the walls is unable to move in the normal (radial)

direction, but is free to move in tangential direction and (2) the flux of the PWP is null. This is expressed as follows,

$$n_1 u + n_2 v + n_3 w = 0 \tag{2.16}$$

and,

$$n_1 \frac{\partial P}{\partial x} + n_2 \frac{\partial P}{\partial y} + n_3 \frac{\partial P}{\partial z} = 0 \tag{2.17}$$

where $\mathbf{n} = [n_1, n_2, n_3]$ is the surface normal vector.

2.3.2 Soil in a unconfined Domain

For the full-scale numerical model the soil domain is modelled as if, it is of infinite extent. This implies that the soil displacements and the PWP attains zero value as the distance increases. Two commonly used methods of simulating infinite domains, are 1) model the geometry of the problem large enough for avoiding boundary effects, or 2) using an "absorption" layer (domain), where energies can be dissipated. The latter method is used in the full-scale model.

Infinite elements are used to simulate the infinite boundaries of the soil domain. The principle of infinite elements, is mapping from one domain to a mapped domain. In the mapped domain, any quantity can be scaled to infinity by a polynomial expression (Zienkiewicz *et al.*, 1983) thus simulating infinite is made possible.

For the full-scale model, the soil displacements are assumed to become zero for infinite extent and the gradient of the PWP is assumed zero. This can be expressed as in Eq. 2.16 for $x, y, z \to \infty$.

A more correct boundary as $x, y, z \to \infty$ would be that the value of PWP attains zero. However since infinite elements are used, it is considered as being of minor importance.

2.3.3 Pile Constraint

In the experimental tests (Sec. 3.1.1) a hinged support is used to ensure zero horizontal displacement of the pile toe. This may simply be written as,

$$u_p = v_p = w_p = 0 \tag{2.18}$$

Applying this constraint as a point constraint, implies rotation in that point is allowed, meaning that the constraint acts as a hinged support.

2.3.4 Pile displacement

The cyclic motion of the pile may be obtained in two ways, namely a force controlled cyclic motion or a displacement controlled cyclic motion. The latter method is used throughout this thesis. In the lab-scale model, a horizontal displacement X_D, measured in the lab-scale experiments (Sec. 3.3.1) is used as input to the displacement in the lab-scale numerical model.

For the full-scale numerical model, the pile displacement is expressed as follows,

$$X_D = x_D \sin \omega t \tag{2.19}$$

where x_D being the amplitude (peak displacement) of the horizontal pile head displacement, t being time and finally ω being the angular frequency,

$$\omega = \frac{2\pi}{T} \tag{2.20}$$

where T being the period of the cyclic motion. The predescribed displacement of the pile is applied as a point displacement at the pile head (see Fig. 5.5)

2.3.5 Free surface

For the mudline a free surface condition is used. This implies no constraints of the soil displacements and no loads. A Dirichlet-type boundary condition is used for the PWP, imposing zero PWP on the mudline.

2.3.6 Pile/soil Interface

The pile/soil interface is modelled as an impermeable no-slip interface. This implies that the displacement of the soil at the pile wall, is identical to the displacement of the pile wall. The effect and consequence of this boundary condition is discussed in Sec. 2.4.

2.4 Assumptions and Limitations

The present numerical model contains a number of assumptions and limitations. These will be presented and discussed below.

The numerical model is a poro-elastic model. This implies that all strains in the soil is reversible. This means that the soil are unable to attain any permanent deformation, hence features such as densification due to the cyclic shearing of the soil grains are omitted. However, since the present study considers the short term response from cyclic loading, it is considered to be sufficient only to model the soil as reversible. However it should be mentioned that work, including the possible densification of the soil due to cyclic

loading, can be found in Cuéllar (2011).

The numerical model does not contain any failure criteria, such as the commonly used Mohr-Coulomb failure criterion. The consequence is, that the numerical model is unable to estimate the ultimate lateral resistance of the soil. In the present work only the stiffness of the pile foundation is considered, and a failure criterion can therefore be omitted.

It is commonly known, that cyclic loading of the soil element with low permeability (poor drainage) will cause the PWP in the soil element to build-up. This build-up is called the residual PWP. In order to obtain a residual PWP, the soil must be able to densify. The Biot equations adopted in the present work can not handle the build-up of PWP, hence residual PWP can not be simulated. For instance, Jeng *et al.* (2010) can be consulted for a second numerical model, where a residual mechanism, in terms of a diffusion equation obtained from the BCE, is implemented. No attempts in the present work, on including the diffusion equation is made.

Finally, the pile/soil interface is modelled with a no-slip boundary condition. As already pointed out by a number of researchers, special attention should be given to the pile/soil interface, e.g. Zania and Hededal (2011), Holeyman *et al.* (2006) and Cuéllar (2011). In Grashuis *et al.* (1990) a description of the soil behavior in a single load cycle is presented. It is stated, that during the cyclic motion of a pile, a gap forms for some portion of the total lateral displacement y. Tensile stresses may occur due to adhesion, however these tensile stresses seems to be limited. In the present model, tensile stresses are allowed. The effect of these tensile stresses have not been investigated further.

2.5 Implementation

This section describes the implementation of the numerical model in the Finite Element software COMSOL Multiphysics (ver. 4.2).

2.5.1 Features used in COMSOL

The numerical model utilizes three main physics interfaces, namely the Solid Mechanics interface (SMI), and the Mathematics Coefficient form PDE (Partial Differential Equations) interface (MCI) or the Heat transfer interface (HTI). The equations governing the pile response (Eq. 2.1-2.9) are implemented in the Solid Mechanics interface.

The seabed response is implemented as follows. The three constitutive equations (Eq. 2.10-2.12) are implemented in the SMI while the storage

equation Eq. 2.14 is implemented in either the MCI or the HTI.

For the numerical model, simulating lab-scale conditions, the walls of the tank are considered as impermeable, which implies zero flux of PWP. This is equivalent to a Neumann-type boundary condition, where zero flux can be specified. Also, in the lab-scale model, the soil is considered to be completely saturated (See 3.1.4). For a complete saturated soil the compressibility term tends towards zero (Yamamoto *et al.*, 1978). To model the saturated seabed response, the term $\frac{n}{K'}\frac{\partial P}{\partial t}$ in Eq. 2.14 is neglected in the numerical model. Since the MCI allows for both specifying a Neumann-type boundary condition and neglecting the compressibility term, it is adopted to model the lab-scale numerical model.

For the full-scale model, the soil should be considered as an infinite soil. The MCI does not include the feature of infinite elements (COMSOL ver. 4.2). Therefore, the HTI is used, since it includes infinite elements. The HTI also allows for neglecting the compressibility term of Eq. 2.14. However it was only possible to obtain a working model in 2D, when the compressibility term was neglected. It should be noted that COMSOL recently (ver. 4.2a) has included infinite elements in the MCI.

2.5.2 Special Issue with Infinite Elements

As described in Sec. 2.5.1, the full-scale numerical model includes infinite elements. As seen from Fig. 5.4 and Fig. 5.5 (Sec. 5.3), two extra layers of soil domains are used. This is necessary, since COMSOL only allows the same infinite elements to be used for one specific physics. Therefore one set of infinite elements is used to dissipate the PWP and a second set of infinite elements is used to dissipate the soil displacements.

2.5.3 Computing Reaction Forces

Weak constraints were used to computed the reaction forces between the pile and the soil. When using weak constraints additional variables are computed in terms of Lagrange Multipliers, λ_L. When applied in the SMI, λ_L can be interpreted as a quantity needed to satisfy a constraint. Therefore λ_L, is equivalent to the reaction force between the pile and the soil.

2.5.4 Discretization, Analysis type and Time-scheme

For the discretization second-order Lagrange elements are used to approximate the dependent variables. Transient studies (time-dependent) are used when computing the soil response due to the cyclic loading. The Generalized-α Method was used for time-stepping scheme. The Generalized-α Method is a one-step, three stage implicit method, where accelerations, velocities and

displacements are uncoupled. The Generalized-α Method is a second order accurate numerical scheme (Chung and Hulbert, 1993). In the numerical model, a fixed time-step of 10^{-4} s was used to ensure convergence.

2.5.5 Hardware and Computational Time

The simulations are performed on a cluster consisting of 64 HP ProLiant SL2x170z G6 nodes. Each node consisted of two Intel Xeon Processor X5550 (quad-core, 2.66GHz, 8MB L3 Cache), with 24GB of memory. The simulations are run on a single node in symmetric multiprocessing environment (SMP), using eight processors.

The computational time for a single computation of the full-scale model, when simulating 20 s real-time seconds is approximately 1-2 days.

This page is intentionally left blank.

Chapter 3

Experimental Investigation of Pile-Soil Interaction

This chapter describes the experimental tests conducted during the scope of this work. Two major tests were conducted. Both tests were on the investigation of the soil behavior during cyclic loading of a pile. The pile simulates an OWT foundation in form of a monopile. Additionally a series of soil tests were completed in order to determine the soil properties. These tests are described in appendix B, appendix C and appendix E.

The objectives with the first major test were to get an understanding of the physical processes in the soil and to obtain data for model validation. As described in Sec. 2.4 the numerical model does not have a component to handle build-up of PWP. As a consequence, a coarse sand ($d_{50} = 0.65$ mm) was used to ensure no build-up of PWP.

For the second major test a coarse silt was used ($d_{50} = 0.07$ mm). The use of coarse silt would ensure build-up of PWP, thus the possibility of reaching liquefaction. Liquefaction may not normally be an issue during design of OWT pile foundations because, during the installation of the pile, the soil will be compacted. Current practiced only mention liquefaction potential in relation to earthquake induced vibrations. However today, some consultancy companies, consider design of OWT pile foundations without scour protection as a viable option (Wittrup, 2012), meaning scour holes around the pile will develop. These scour holes will undergo a sequence of erosion and backfill. After backfill, the scour hole may be filled with a loose soil, thus the soil will be susceptible to liquefaction.

For the two major tests, the experimental setup was nearly similar. However few changes were applied for the tests on coarse silt, including pile support, testing procedure and bending moments measurements. These changes will be described later.

3.1 Method

3.1.1 The Experimental Setup

For the rocking pile experiment (Fig. 3.1) two cylindrical low density polythene tanks were used. Each tank had a volume capacity of 7 m^3. The tank diameter was 2 m and the height was 2.63 m. The two tanks were connected by an overflow PVC pipe placed 2.42 m from the bottom of the tank. The rocking pile experiments were conducted in only one of the tanks. This tank will be termed *Tank A*. The other tank will be termed *Tank B*. Inside Tank A, concrete slopes were established making the bottom of the tank having the same shape as an inverse frustum of a right circular cone.

A 243 cm long stainless steel pile was used to simulate the OWT pile foundation. The outer diameter of the pile was 206 mm and the wall thickness was 3 mm. In the case of the coarse sand experiments, the pile was supported by a hinge connection located 7 cm from the pile toe. The hinge connection ensured zero pile displacement at the pile toe. For the coarse silt experiments a cone fixed to the bed of Tank A was used as support. The purpose of the cone was to guide the pile to the same location when the pile was driven through the soil.

The rocking of the pile was performed by a conventional hydraulic piston. The piston had a load capacity of approximately 5 kN. The piston was placed on a steel tripod, bolted to the concrete floor. The force exerted at the pile head was measured by a tension/compression S-Beam load cell having a capacity of 5 kN. The load cell was placed between the driving piston and the pile 3 cm below the pile head.

3.1.2 Pile Displacement

To measure the pile head displacement, a potentiometer was used to measure the displacement of the pile at the pile head. To measure the deflection along the length of the pile, a total of eight strain gauges were used. The strain gauges were of the type single element 6 mm strain gauge. The strain gauges were placed 300 mm apart, starting 312 mm from the pile head (Fig. 3.1). To avoid water coming into contact with the strain gauges, the strain gauges were covered with ethanoic acid free silicone. To protect the silicone and the strain gauges, a half pipe (PVC) was used to cover the entire vertical of the strain gauges. Silicone was used as bonding and sealing material. Details on the calibration of the strain gauges are found in appendix D.

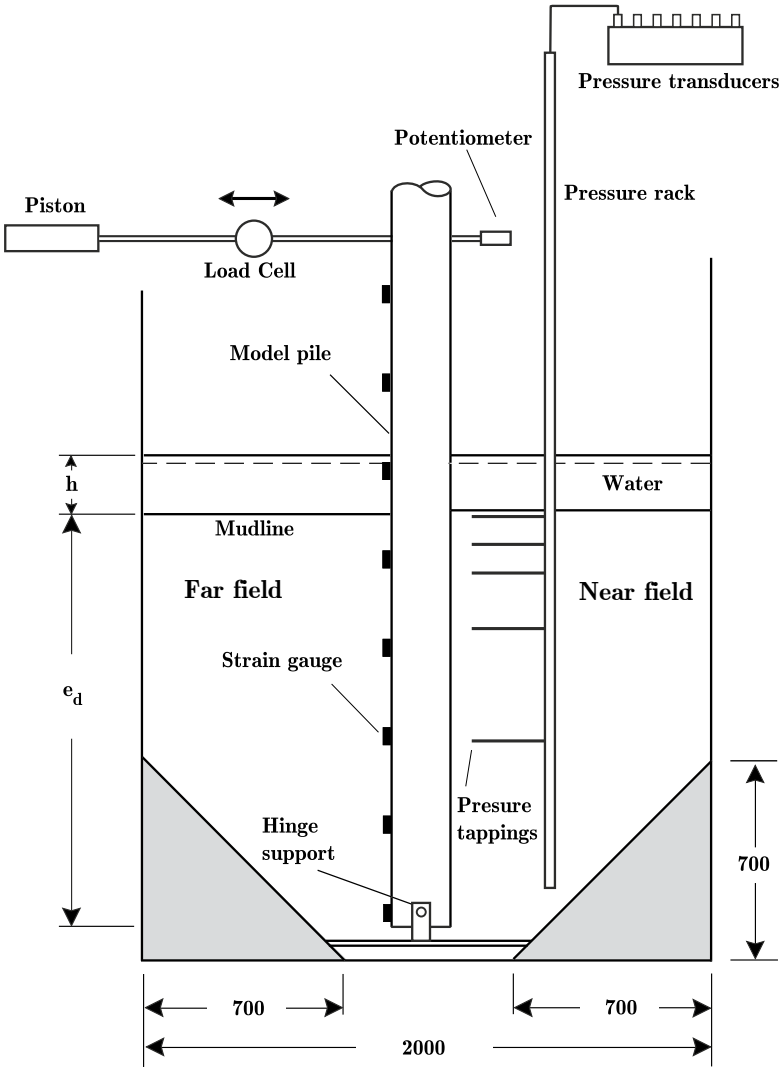

Figure 3.1: *Setup in Tank A used during the coarse sand tests. To keep the figure simple, only the first vertical of the pressure rack is shown. Dimensions shown in the unit mm.*

The pile deflection was calculated, by using the method described by Reese and Impe (2001) and Yang and Liang (2007), namely by fitting a sixth order polynomial to the bending moment distribution followed by a double integration. The integration constants, C_1 and C_2 were determined using the following boundary conditions,

$$x = X_D \quad at\ z = -92.5\ \text{cm} \tag{3.1}$$

$$x = 0 \quad at\ z = 140.0\ \text{cm} \tag{3.2}$$

where x being the horizontal model pile deflection, X_D being the horizontal displacement measured at the pile head and z being the vertical axis.

3.1.3 PWP Measurements

The PWP was measured by using Honeywell, model 26C118 15 PSI temperature compensated pressure transducers (Fig. 3.2). Pressure tappings, with an outer diameter of 10 mm and covered with 38 µm nylon filters, were fixed on a pressure rack placed at $\theta = 0°$ (see Fig. 1.2). A total of 15 pressure tappings were used. The pressure tappings were arranged in five groups consisting of three pressure tappings with an individual vertical spacing of 2 cm. The distance between each group was 10 cm, 10 cm, 20 cm, and 45 cm . They were placed along three verticals with a distance $r = 2$ cm, $r = 7$ cm and $r = 12$ cm from the side wall of the pile (Fig. 3.3). The tubes connecting the pressure tappings to the pressure transducers were made of stainless steel tubes and transparent plastic piezometer tubes. The stainless steel tubes were used in the soil, whereas the plastic tubes were used as connection in free space. This ensured that the pressure in the tubes would be unaffected by pressure variations due to movement of the surrounding soil and a flexible pressure measurements system with respect to placing the pressure rack at different locations. The wall thickness of the stainless steel tubes was 1 mm and the outer diameter was 4 mm. The wall thickness of the plastic tubes was 1 mm and the outer diameter was 4 mm. The total length of the connections between the pressure tappings and the pressure transducers were approximately 5 m. Care was taken to avoid air bubbles inside the tubes.

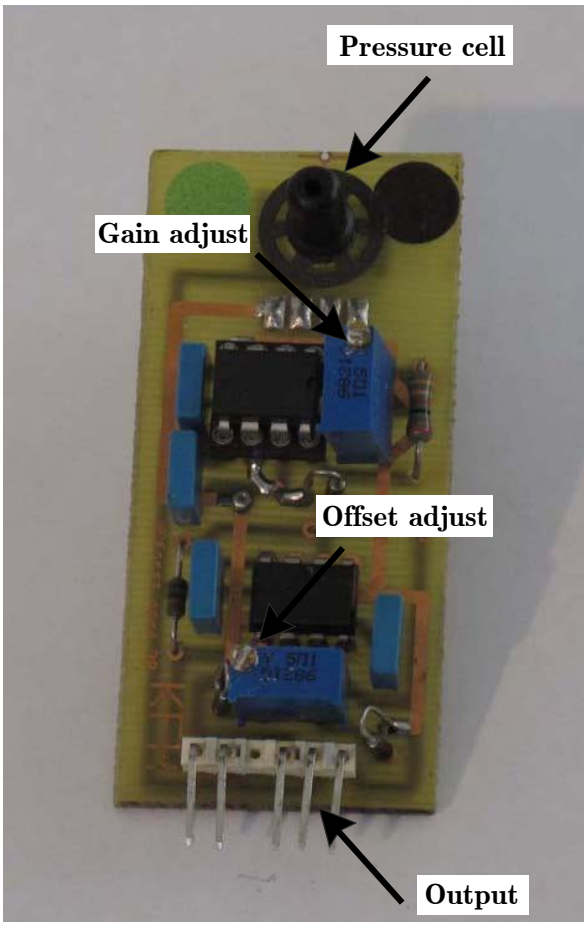

Figure 3.2: *Pressure cell used for PWP measurements*

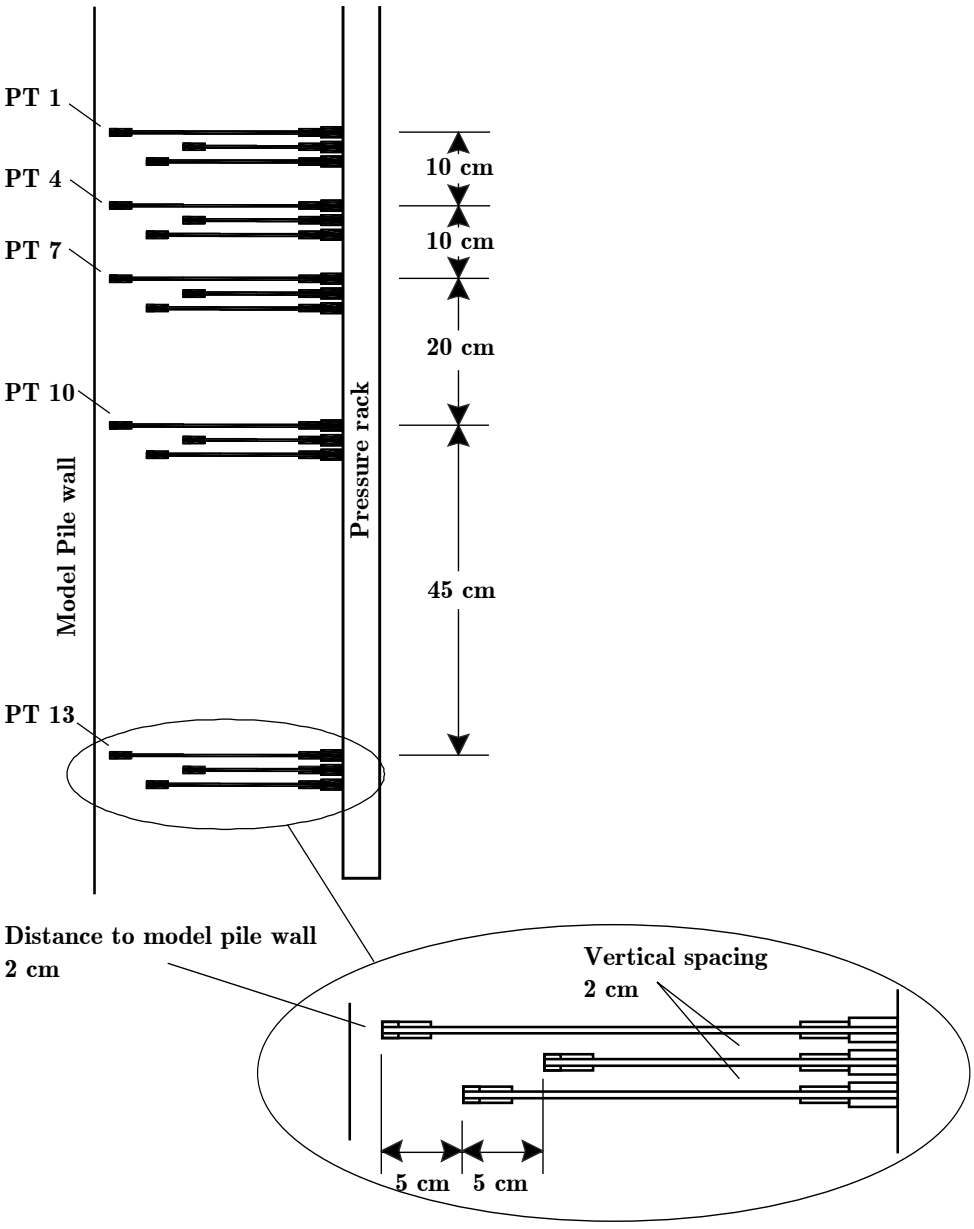

Figure 3.3: *Configuration of the pressure rack used for PWP measurements.*

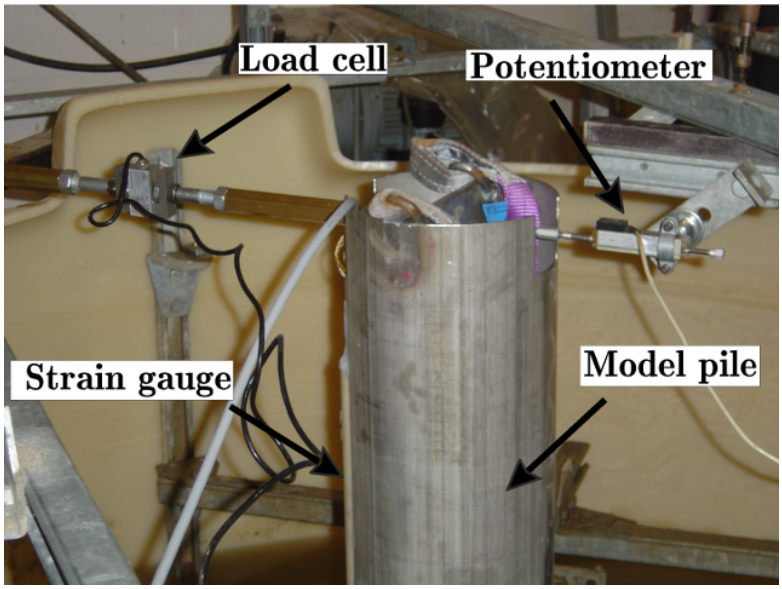

Figure 3.4: *Model pile.*

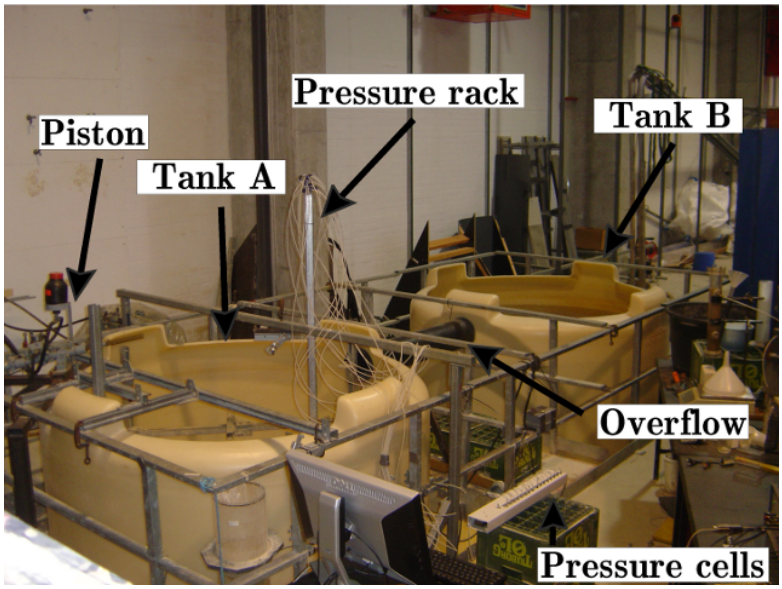

Figure 3.5: *The setup.*

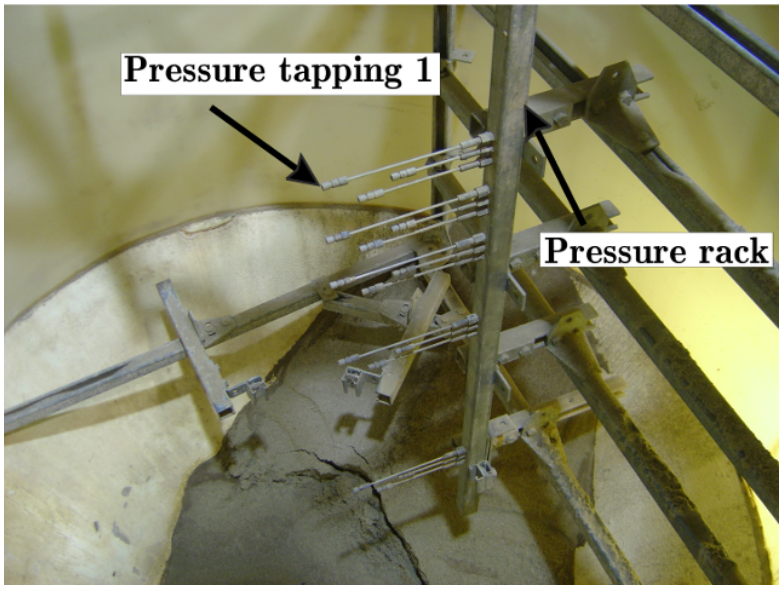

Figure 3.6: *Pressure rack.*

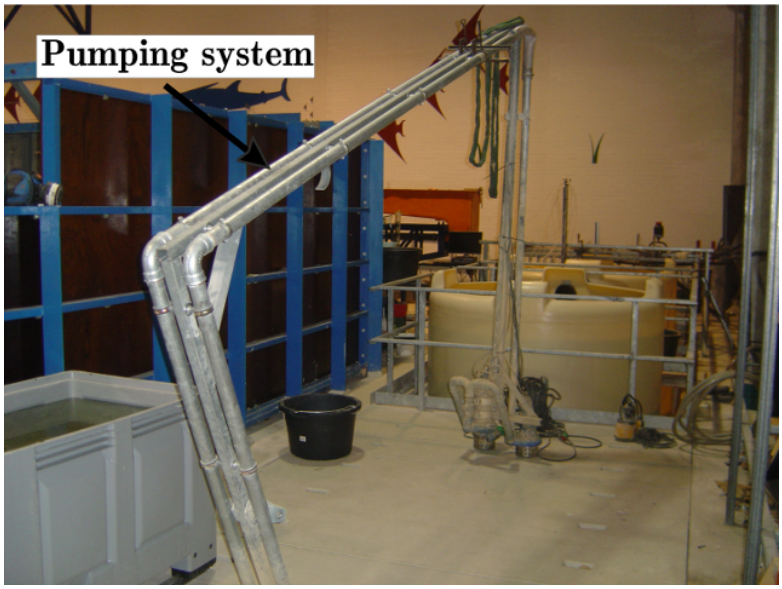

Figure 3.7: *Pumping system.*

3.1.4 Seabed preparation

Prior each test, the seabed was prepared. To prepare the seabed, hydraulic backfilling was used. Initially, the soil and water were placed in Tank B. Tank A was filled with water. An overflow pipe was connecting the two tanks. To pump the mixture of soil and water from Tank B, to Tank A, a pumping arrangement was used (Fig. 3.8). The pumping arrangement consisted of three submersible pumps (maximum delivery rate = 24 m^3/h). Two pumps were used to suck a mixture of soil and water from Tank B to Tank A. The third pump was used to loosen the soil in Tank B by jetting water towards the seabed. The slurry material was ejected from the outlet of the pumping arrangement below the water surface. The soil grains then loosely settled with its fall velocity. This method ensured, that no air was trapped inside the soil, hence a fully saturated seabed was likely created. A nearly identical method for preparing the seabed has been reported in Rietdijk *et al.* (2010).

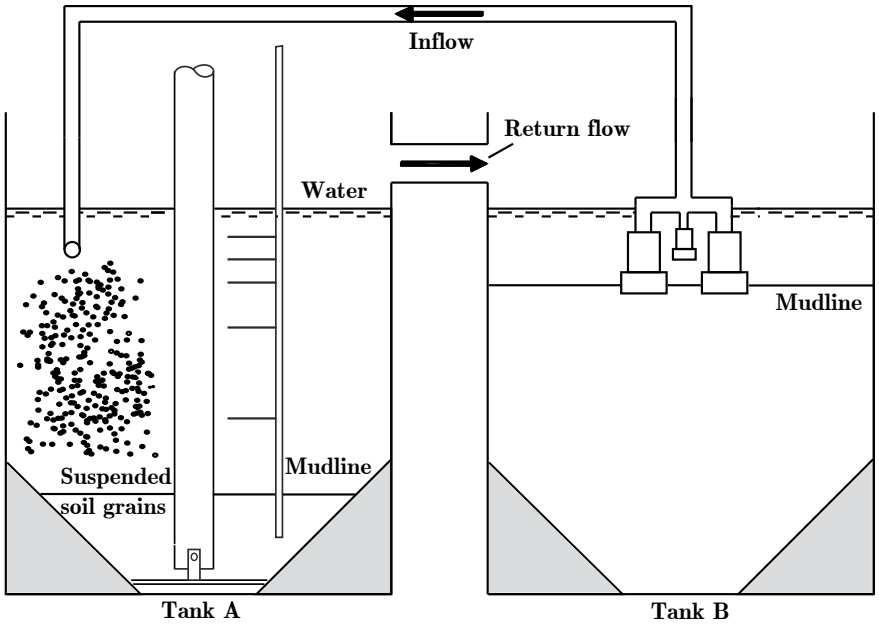

Figure 3.8: *Pumping arrangement used for seabed preparation. Coarse sand setup.*

The seabed preparation procedure, for the coarse sand experiments, was as follows; (1) The model pile was installed in Tank A. (2) Tank A was filled with water, while Tank B was filled with soil and water. (3) The three pumps were switched on and the pumps were lowered following the decreasing mudline. (4) When the pumps reached the bottom of Tank B, the pumping continued for one hour. This ensured, that only suspended sediment was left in Tank B. (5) After turning off the pumps, the suspended sediment was left to settle

in Tank A for approximately 30 minutes. (6) The water level in Tank A was then lowered to approximately 10 cm from the mudline, by using a submersible pump. (7) The surface of the mudline was gently leveled by using a wood plate and the distance between the pile head and the mudline was measured.

For the coarse silt experiments, the procedure of preparing the seabed was nearly identical. However, it is necessary to start from step 1. (1) Tank A was filled with water, while Tank B was filled with soil and water. (2) The three pumps were switched on and the pumps were lowered following the decreasing mudline. (3) When the pumps reached the bottom of Tank B, the pumping continued for one hour. (4) The model pile was then driving through the loosely packed seabed via a guiding system down to the support cone. (5) The suspended sediment was left to settle in Tank A for two days. (6) The water level in Tank A was then lowered to approximately 5 cm from the mudline making it possible to measure the distance between the pile head and the mudline. (7) Tank A was then refilled with water to the level of the overflow pipe.

3.1.5 Visualization

In the coarse silt experiments, video recordings from the inside of the model pile were adopted. A transparent acrylic pile with an outer diameter of 200 mm was used as model pile. The model pile was placed in Tank A prior filling the tank with soil. In this way, no soil would be inside the pile. To ensure clean water inside the model pile, the model pile was filled with clean water. To guide the video camera inside the model pile, a guiding arrangement was established. A flashlight was used to illuminate the inside of the model pile.

3.1.6 Test Conditions

This small section gives the test conditions used for both the coarse sand and the coarse silt experiments. The test conditions for the visualization of the coarse silt experiments are not given herein. All values correspond to initial test conditions.
The values tabulated for the pressure tappings correspond to the initial distance from the pressure tapping to the mudline.

	Unit	Coarse sand experi-ments	Coarse silt experi-ments
Amplitude of pile head displacement	$[mm]$	2.4	3.3
Period of cyclic loading T	$[s]$	3	3
Foundation depth e_d	$[cm]$	147	143
Soil depth	$[cm]$	154	155
Water depth	$[cm]$	10	56
Pressure tapping PT 1	$[cm]$	0.0	0.0
Pressure tapping PT 2	$[cm]$	0.0	0.0
Pressure tapping PT 3	$[cm]$	0.0	0.0
Pressure tapping PT 4	$[cm]$	1.5	1.4
Pressure tapping PT 5	$[cm]$	3.5	3.4
Pressure tapping PT 6	$[cm]$	5.5	5.4
Pressure tapping PT 7	$[cm]$	11.5	11.4
Pressure tapping PT 8	$[cm]$	13.5	13.4
Pressure tapping PT 9	$[cm]$	15.5	15.4
Pressure tapping PT 10	$[cm]$	31.5	31.4
Pressure tapping PT 11	$[cm]$	33.5	33.4
Pressure tapping PT 12	$[cm]$	35.5	35.4
Pressure tapping PT 13	$[cm]$	76.5	76.4
Pressure tapping PT 14	$[cm]$	78.5	78.4
Pressure tapping PT 15	$[cm]$	80.5	80.4

Table 3.1: *Test conditions. Distances tabulated for the pressure tappings correspond to the vertical distance from the pressure tapping to the mudline.*

3.1.7 Data Treatment and Analysis

The raw data (PWP time-series) from the experiment did contain a significant amount of "noise". See Appendix A for a typical unfiltered PWP time-series. The noise consisted of both high and low frequency noise. To filter the data a Savitzky-Golay smoothing filter was used (Press *et al.*, 2007). To implement the Savitzky-Golay smoothing filter a build-in matlab routine was used. A second order $k = 2$ polynomial regression with a window length of 53 discrete data points was used.

The rocking pile experiments, may not be considered as stationary process throughout the entire experiments, since the soil properties changes with time. But the experiments might be considered as stationary if a sufficiently small number of periods are considered, however the number should still be large enough to give reliable statistical quantities.

The PWP may be analyzed in terms of a mean PWP as function of phase $< P >$ and may be calculated with the so-called ensemble average, which is written as (Sumer, 2007),

$$< P > (\omega t) = \frac{1}{N} \sum_{j=1}^{N} P[\omega(t + (j-1)T)] \tag{3.3}$$

Likewise, the fluctuating component of the PWP as function of phase may be defined as,

$$\sqrt{\overline{(P - < P >)'^2}} = \sigma_P = \left(\frac{1}{N-1} \sum_{j=1}^{N} [P[\omega(t + (j-1)T)] - < P > (\omega t)]^2 \right)^{\frac{1}{2}} \tag{3.4}$$

where N being the number of periods. A sensitive analysis showed that a sample $N > 40$ was sufficient to give statistical reliable data.

3.2 Soil Properties

The soil used in the experimental tests were coarse sand ($d_{50} = 0.64$ mm) and coarse silt ($d_{50} = 0.07$ mm). The soil properties are presented in Tab. 3.2 and Tab 3.3.

The grain size distributions (Fig. 3.9) were determined through a conventional sieve analysis for particles larger than or equal to 0.063 mm. The distributions of particle sizes less than 0.063 mm were determined through the hydro-suspension method. Both methods are described in DGF Laboratoriekomité (2001).

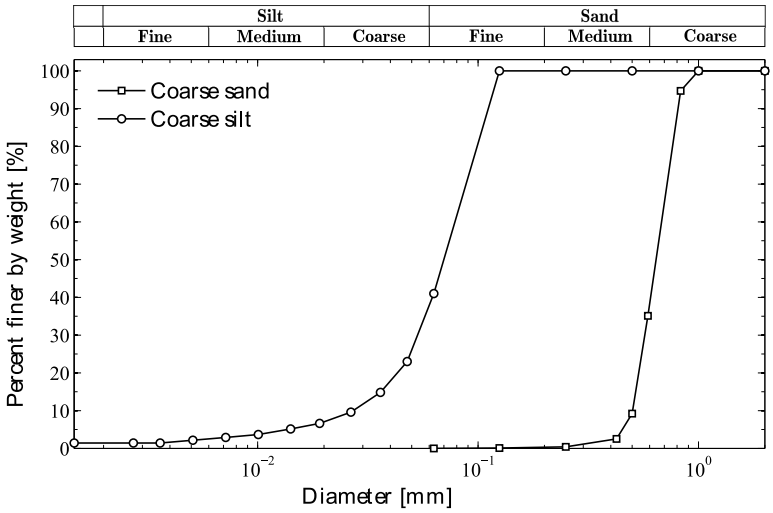

Figure 3.9: *Grain size distributions*

The coarse sand and coarse silt had an uniformity coefficient ($C_u = d_{60}/d_{10}$) of 1.4 and 2.9, respectively. The coarse sand may be termed as a well sorted soil.

The void ratio e_{max} is when the soil is in its loosest condition and e_{min} is when the soil is in its densest condition. The void ratio e_{max} and the specific gravity of the soil grains, d_s, were determined by the standard methods provided by the Danish Geotechnical Society's Lab Committee (DGF Laboratoriekomité, 2001). The minimum void ratio e_{min} was determined by vibrating a known mixture of soil and water in a beaker until the minimum void ratio was reached.

For the coarse sand experiments, the initial void ratio could not be determined from traditional soil sampling. Instead the initial void ratio was determined in the following two ways. (1) the void ratio was calculated based on the Tank A dimensions and the known total amount of sand in the

tank, thus the void ratio may be considered, as a crude estimation of an average void ratio. (2) the sand was gently poured down in a beaker containing water. This should simulate the preparation of the seabed bed. The beaker was gently tapped a few times for the soil grains to settle loosely.

To determine the void ratio for the coarse silt, the traditional soil sampling method was used to determine the before and after void ratios. From the traditional soil sampling, only the void ratio in the upper 0 cm − 20 cm could be determined. To estimate the void ratio variation as function of soil depth, a long acrylic tube was used as a sampler. From these tests, the void ratio seemed to be slightly higher (soil being less compacted) than measured with the traditional sampling method. However both methods indicate that the soil in the coarse silt experiments may be termed as medium dense soil (Lambe and Whitman, 1969, pg. 31). The void ratio from the traditional soil sampling was adopted. See appendix C for further details.

The strength- and elastic properties for the coarse sand were determined by conducting a number of drained triaxial tests. It was found that the Young's modulus was little influenced by the relative density D_r. An approximate expression for the Young's modulus of the coarse sand may be given as (Appendix E),

$$E = E_{ref} \left(\frac{\sigma'_3}{\sigma'_{3,ref}} \right)^{\alpha} \tag{3.5}$$

where $E_{ref} = 91$ MPa, $\sigma_{3,ref} = 100$ kPa and $\alpha = 0.61$. For a stress level of 1 m ($\sigma'_3 = 9.5$ kPa) the Young's modulus for the coarse soil will be 22 MPa. Some scatter were observed when determining the Poisson's ratio. An average Poisson's ratio of 0.20 was adopted. The friction angle φ was seen to vary from 40.3° ($D_r = 0.50$) to 44.7° ($D_r = 0.80$). Here a friction angle of 42° was adopted. In the case of coarse silt, an Young's modulus of 5 MPa, a Poisson's ratio of 0.29 and a friction angle of 35° were adopted from the paper of Sumer *et al.* (2012), since identical material was used.

A number of permeability tests on the coarse sand were conducted for different relative densities. The permeability may be determined as,

$$k \quad = \quad -0.15 \cdot D_r + 0.45 \text{ cm/s} \tag{3.6}$$

Thus the coarse sand may initially be termed, a high permeable sand ($k = 0.37$ cm/s). See appendix B for further details. The permeability coefficient for the coarse silt was adopted from the paper of Sumer *et al.* (2012). The coarse silt may be termed as a medium permeable sand ($k = 0.0015$ cm/s).

It may be noticed that the degree of saturation equals unity. This implies that the soil do not contain any gas/air bubbles. As described in Sec. 3.1.4,

the seabed was prepared in a way similar to what was done in Sumer *et al.* (1999) making it reasonable to assume that the seabed should be gas/air bubbles free. This assumption will later be discussed in Sec. 4.2.3

Parameter	Symbol	Value	Before test
Grain size	d_{50}	0.64 mm	
Specific gravity of soil grain	d_s	2.64	
Uniformity coefficient	$C_u = d_{60}/d_{10}$	1.4	
Maximum void ratio	e_{max}	0.88	
Minimum void ratio	e_{min}	0.60	
Degree of saturation	S_r	1.00	
Young's modulus of elasticity	E	22 MPa	
Poisson's ratio	ν	0.20	
Friction angel	φ	42°	
Permeability coefficient	k	0.37 cm/s	
Void ratio	e	–	0.73
Porosity	$n = e/(1+e)$	–	0.42
Total specific weight of sediment	$\gamma_t = (s+e)/(1+e) \cdot \gamma_w$	–	19.5 kN/m^3
Total specific gravity of sediment	$s_t = \gamma_t/\gamma_w$	–	1.95
Submerged specific weight of sediment	$\gamma' = \gamma_t - \gamma_w$	–	9.5 kN/m^3
Relative density	$D_r = (e_{max} - e)/(e_{max} - e_{min})$	–	0.55

Table 3.2: *Soil properties, coarse sand*

Parameter	Symbol	Value	Value	
			Before test	After test
Grain size	d_{50}	0.07 mm		
Specific gravity of soil grain	d_s	2.67		
Uniformity coefficient	$C_u = d_{60}/d_{10}$	2.9		
Maximum void ratio	e_{max}	1.20		
Minimum void ratio	e_{min}	0.57		
Degree of saturation	S_r	1.00		
Young's modulus of elasticity	E	5 MPa		
Poisson's ratio	ν	0.29		
Friction angel	φ	35°		
Permeability coefficient	k	0.0015 cm/s		
Void ratio	e	–	0.94	0.86
Porosity	$n = e/(1+e)$	–	0.48	0.46
Total specific weight of sediment	$\gamma_t = (s+e)/(1+e) \cdot \gamma_w$	–	$18.61 kN/m^3$	$18.98 kN/m^3$
Total specific gravity of sediment	$s_t = \gamma_t/\gamma_w$	–	1.86	1.90
Submerged specific weight of sediment	$\gamma' = \gamma_t - \gamma_w$	–	$8.61 kN/m^3$	$8.98 kN/m^3$
Relative density	$D_r = (e_{max} - e)/(e_{max} - e_{min})$	–	0.41	0.54

Table 3.3: *Soil properties, coarse silt*

3.3 Experimental Results

3.3.1 Coarse Sand

The cyclic motion of the model pile introduce cyclic shear deformations in the soil. The cyclic shearing rearrange the soil grains. PWP will be generated due to the reduction/expansion of the soil grains during the cyclic shearing. The PWP generated during the cyclic loading, is governed by the Biot equations.

Pore-water Pressure during cyclic Loading

Fig. 3.10 shows the time-series of the PWP measured at PT 10. Also shown is the associated pile head displacement and the force exerted by the hydraulic piston. The PWP is seen to build-up initially. However, the accumulated PWP is seen to be dissipated rapidly. This will be discussed later. From Fig. 3.10.b it may be noticed that the pile head displacement decreases slightly, starting from an amplitude of $x_D = 2.4$ mm to $x_D = 1.9$ mm. The decrease in amplitude is considered of minor importance. Finally, the force is seen to increase as the rocking of the pile continues. This is expected, since the soil becomes more compact during the cyclic loading.

Fig. 3.12 shows a close-up. (marked A in Fig. 3.10) of the time-series. From the figure, the following two observations may be seen. (1) The PWP is seen to build-up initially. This is indicated by defining the period average PWP $\overline{P}$ as,

$$\overline{P} = \frac{1}{T}\int_t^{t+T} P\ dt \tag{3.7}$$

The period averaged PWP is however quickly dissipated, which is expected due to the high permeability of the soil. (2) The PWP is seen to oscillate with a frequency twice the frequency of the cyclic loading. This will be discussed in a short while.

Fig. 3.13 shows another close-up (marked B in Fig. 3.10). Here it can be seen, that the period averaged PWP has attained a constant value. It may also be seen, that the PWP still oscillates with a frequency twice the frequency of the cyclic loading. The explanation of the double frequency is as follows,

Considering the pile at *position 1* (reference to Fig. 3.11). The pile has moved to its outmost position in the far field (furthers away from the pressure rack). The soil surrounding the pile is completely in contact with the pile walls. As the pile begins to move towards the pressure tappings, the pore-water in front of the pile is pressurized (A in Fig. 3.13.a). Until *position 2* is reached, the pile and the soil surrounding it, are in contact. When passing

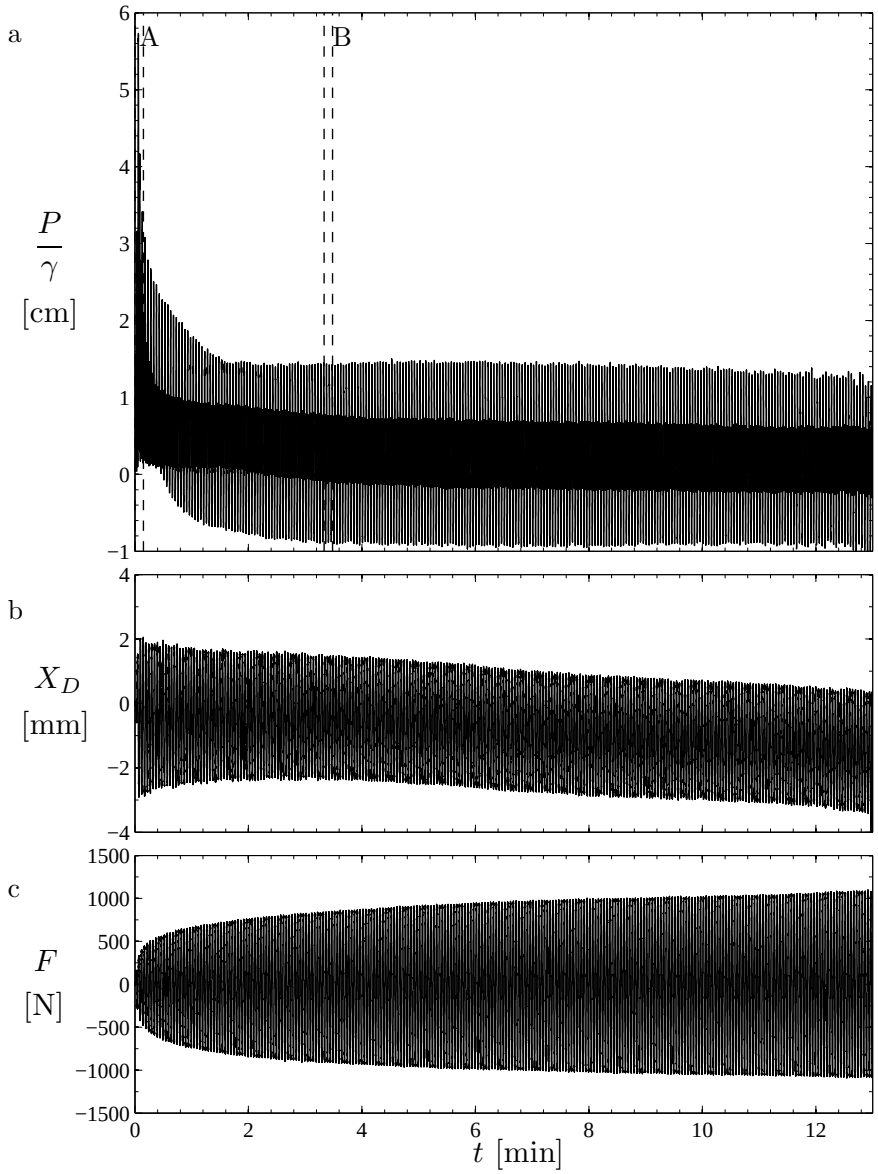

Figure 3.10: *Time-series of coarse sand experiment. a: Pore-pressure time-series (PT 10). Measured a at vertical* 2 cm *from the pile and* $z = 31.5$cm *below the mudline. b: Pile head displacement.* (+) *pile motion towards the pressure tappings /* (−) *pile motion away from the pressure tappings. c: Applied force,* (+) *tension force /* (−) *compression force.*

position 2 a small gap forms on the backside of the pile wall, which is filled with pore-water (already available) and suction is generated at the backside of the pile. This suction is felt immediately at the pressure tappings (B in Fig. 3.13.a). When the pile comes to a full stop at *position 3* the PWP is dissipated and the soil grains in the meantime gradually, fill the gap. When the pile move from *position 3* to *position 4* the pore water in front of the pile (in the far field) is pressurized. This pressure is felt in the near field (C in Fig. 3.13.a). When the pile passes *position 4*, once again, a gap is forming, this time at the pile wall in the near field. The suction associated with the formation of the gap is clearly seen in the pressure time-series (D in Fig. 3.13.a). The suction is now more pronounced since the suction appears at the near field where the pressure tappings are located. When the pile comes to a full stop at *position 5*, the PWP is now again dissipated. This sequence of events concludes one period.

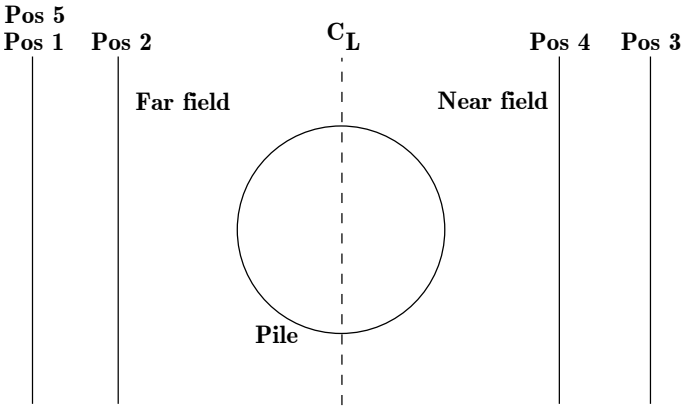

Figure 3.11: *Illustration of pile motion, plan view*

PWP generated in the soil is governed by a diffusion mechanism with a diffusion coefficient equal to c_v, the coefficient of consolidation which can, to a first approximation, be estimated from (Sumer and Fredsøe, 2002),

$$c_v = \frac{Gk}{\gamma} \tag{3.8}$$

The length scale y_s associated with the diffusion of the PWP may be estimated as (Sumer, 2007),

$$y_s^2 = 2c_v t \tag{3.9}$$

By fixing the length scale y_s to 30 cm, the time scale t for the pressure to be sensed, can be estimated by combining Eq. 3.8 and 3.9. The time scale found is in the order of $t = \mathcal{O}(0.015s)$, which is immediately.

Finally, by comparing Fig. 3.13.a and 3.13.c it may be noticed, that the PWP and the velocity of the pile motion, are in phase. This indicates the soil being fully saturated. This will be discussed later in Sec. 4.2.3.

Fig. 3.14 shows the PWP measured at the vertical 2 cm from the pile wall. It is seen, that the PWP measured throughout the soil depth is in phase. This also apply for the PWP measured for increasing distance r away from the pile (Fig. 3.15).

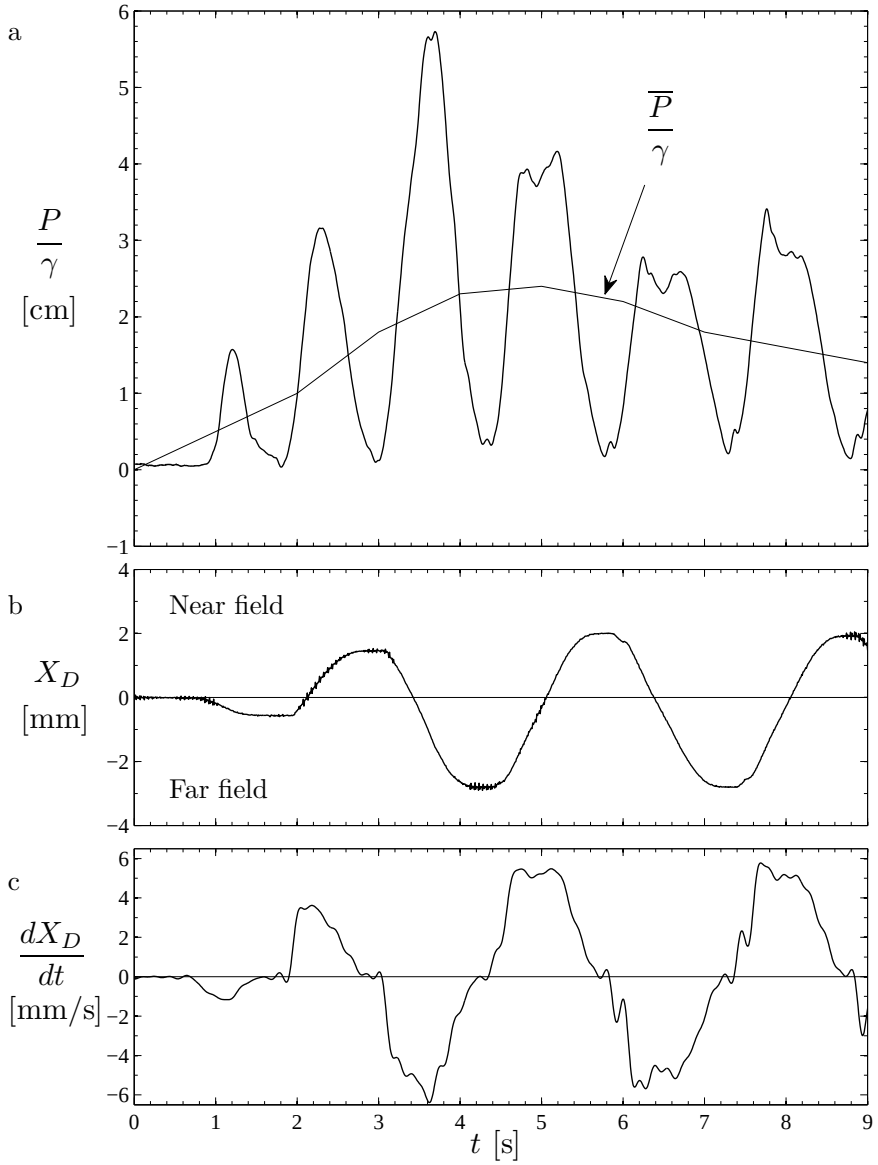

Figure 3.12: *Time-series of coarse sand experiment (Section A). a: Pore-pressure time-series (PT 10). b: Pile head displacement.* (+) *pile motion towards the pressure tappings /* (−) *pile motion away from the pressure tappings. c: Applied force,* (+) *tension force /* (−) *compression force.*

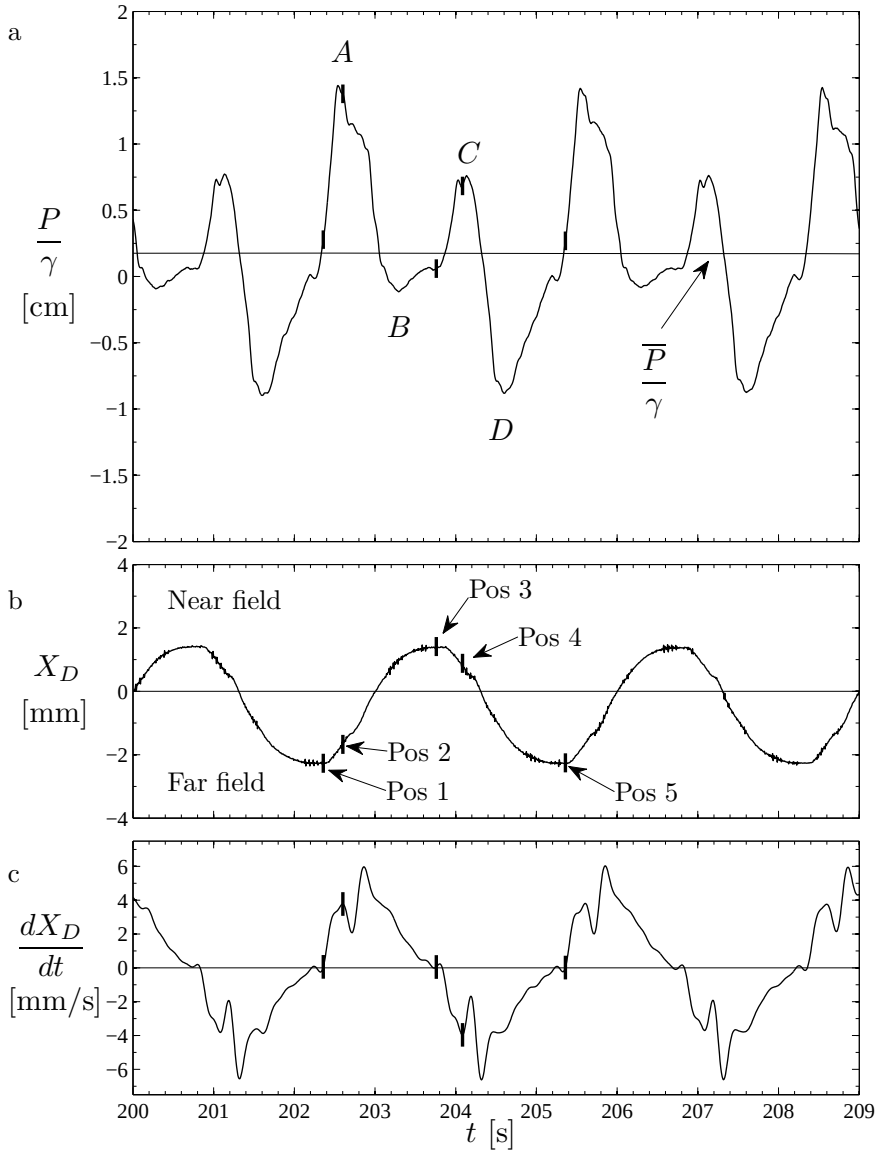

Figure 3.13: *Time-series of coarse sand experiment (Section B). a: Pore-pressure time-series (PT 10). b: Pile head displacement. (+) pile motion towards the pressure tappings / (−) pile motion away from the pressure tappings. c: Applied force, (+) tension force / (−) compression force.*

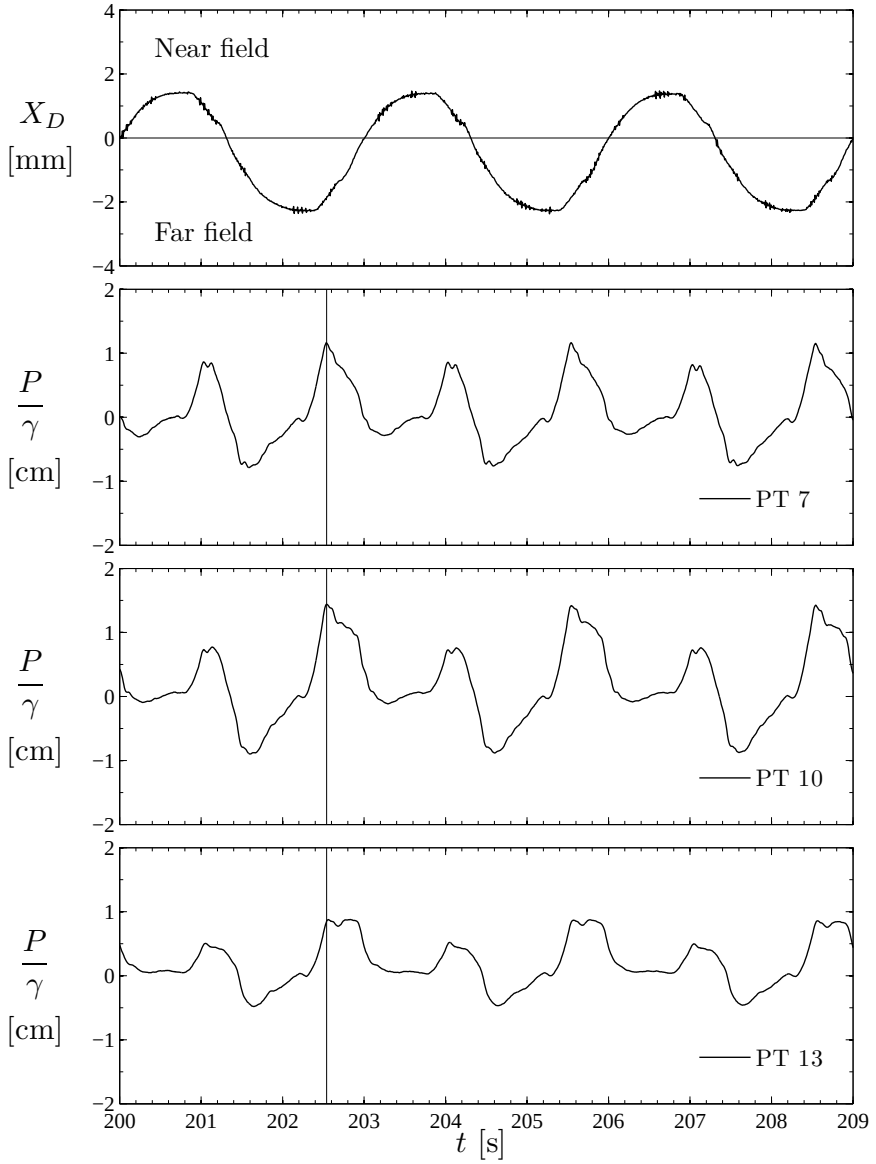

Figure 3.14: *PWP time series measured at a vertical distance* $r = 2$ cm, $z = 11.5$ cm, $z = 31.5$ cm *and* $z = 76.5$ cm.

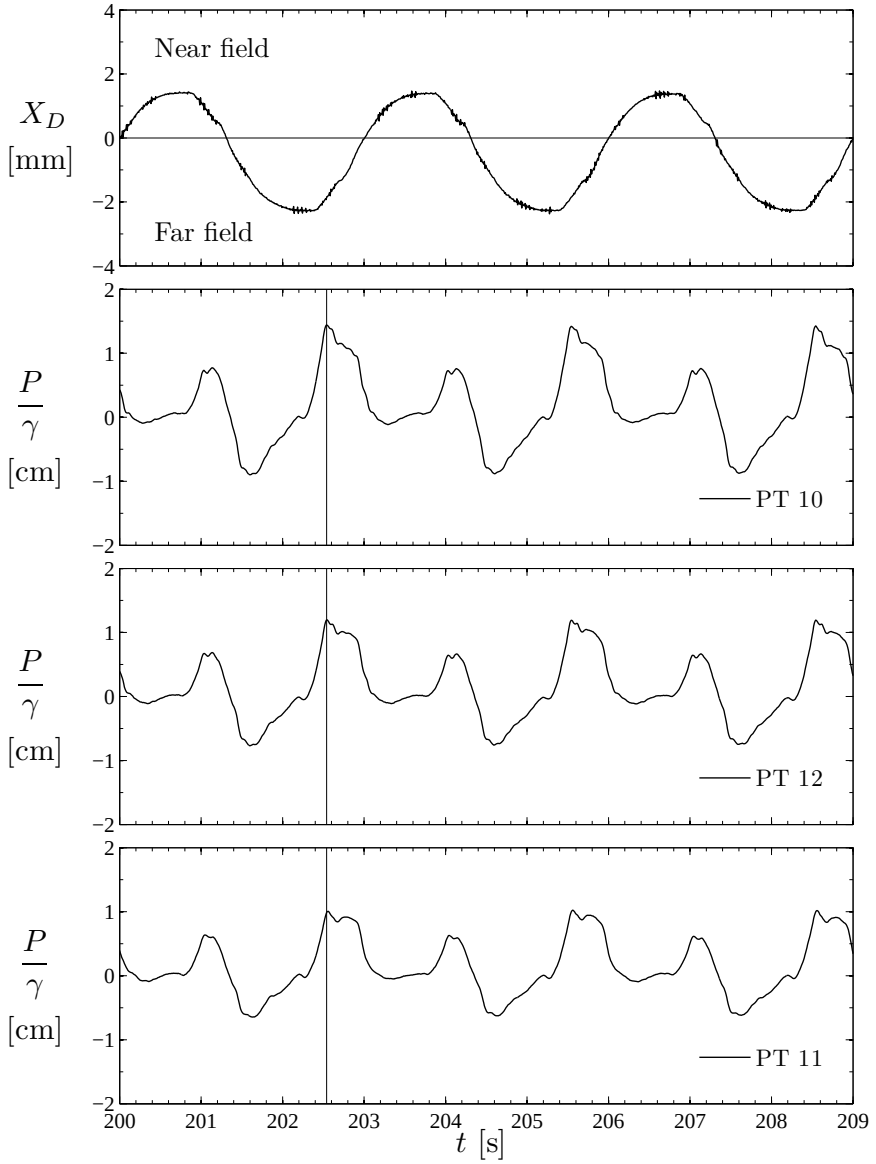

Figure 3.15: *PWP time series measured at a horizontal distance* $r = 2$ cm, $r = 7$ cm *and* $r = 12$ cm

Vertical Pore-water Pressure Distribution

Fig. 3.16 displays the vertical PWP distribution measured at three radial distances r at $\theta = 0°$. The distributions represent a snapshot in time of the PWP at phase $\omega t = 316°$ equivalent to the time instant of maximum PWP. Considering the magnitude of the vertical distributions, it may be noticed, that the PWP decreases as the radial distance increases. A result which would be expected. It shows that the generation of PWP is strongly dependent of the local soil displacements, since the soil displacements clearly must decrease when the radial distance increases.

The results also show that the PWP tends towards zero when approaching the mudline. This is a result which also would be expected. This means that although the local soil displacements increases when approaching the mudline, the PWP can not obtain any increase in PWP, because PWP is dissipated instantaneously.

Finally the result also shows that the PWP decreases when approaching the pile toe. Clearly as z approaches the pile toe, the displacements becomes smaller, thus the PWP decreases.

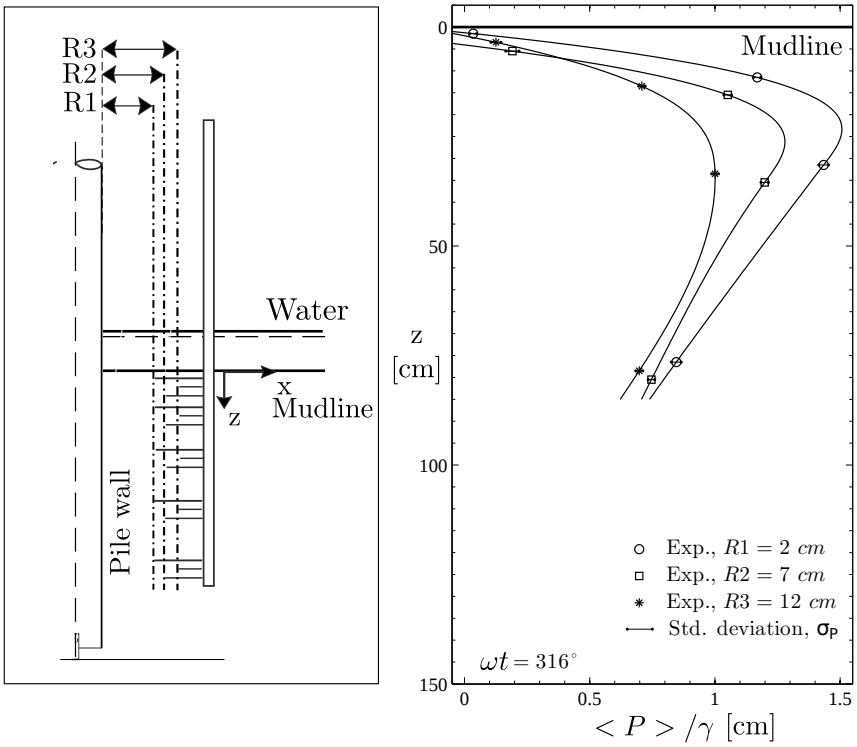

Figure 3.16: *Vertical pore-water pressure amplitude distributions measured at a radial distance,* $R1 = 2$ cm, $R2 = 7$ cm *and* $R3 = 12$ cm *from the pile wall. Marks represent the point measurements. Solid line represents a "eye-fit" to the experimental data.*

Pile Deflection under Cyclic Loading

As described in Sec. 3.1.2, the maximum pile deflection may be obtained from the bending moment distribution (Fig. 3.17.A) at phase $\omega t = \pi/2$. As described in appendix D, only four out of eight strain gauges were functioning, namely strain gauge B, C, E and F. The final four strain gauges had to be manually fitted to the experimental moment distribution. The procedure of fitting the data from the final four strain gauges to the moment distribution is outlined in the following,

- Strain gauge A; From the pile head to the mudline, the moment distribution must be a straight line since moment is expressed as **Moment** = **Force** x **Arm**, thus the moment must be linearly increasing from zero at the pile head to the location of the mudline.
- Strain gage D and G; The moment distribution can be represented by a 6^{th}-order polynomial. The data points for strain gauge D and G were placed such that they followed the shape of the polynomial.
- Strain gauge H; At the pile toe, zero moment is expected.

After double integration of the moment distribution and utilizing the known boundary conditions, the model pile deflection (Fig. 3.17.B) can be obtained. Also plotted in Fig. 3.17.B is the rigid pile deflection. It may be noticed that the deflection of the model pile is extremely small. The maximum deflection is approximately 0.05 mm at $z = 0.44$ m, thus the pile performs almost as a rigid pile.

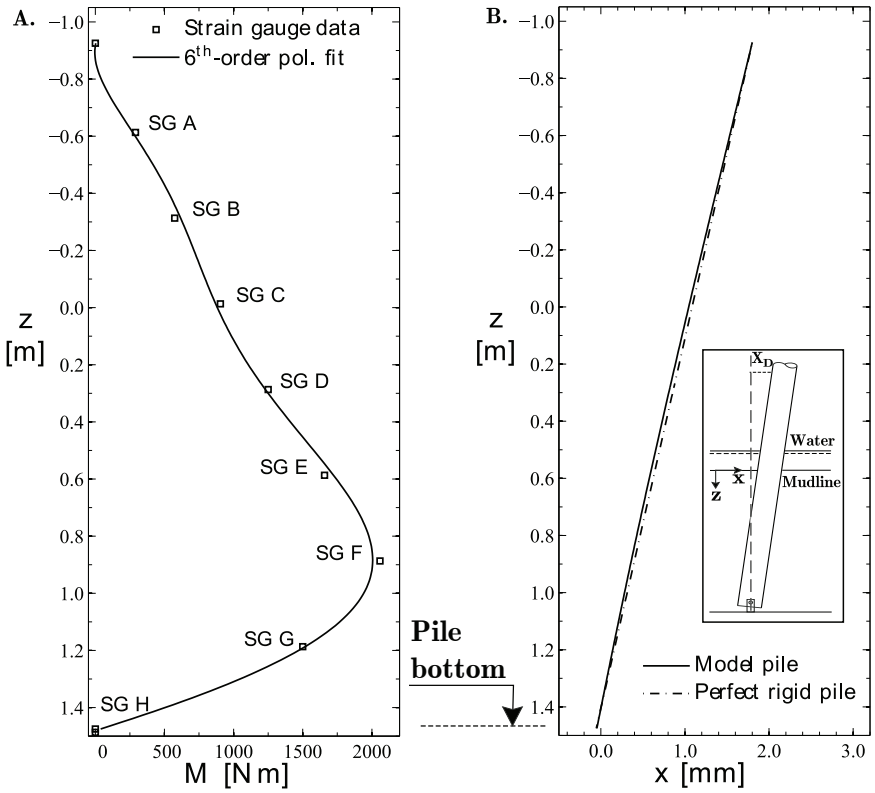

Figure 3.17: *(A.) Moment distribution obtained from the strain gauges. Stain gauge A, D ,G and H is fitted to the* 6^{th}*-order polynomial. (B.) Pile deflection curve at* $\omega t = \pi/2$.

3.3.2 Coarse Silt

It is commonly known, if the build-up of PWP exceeds the overburden pressure, the soil will become liquefied. If the build-up of PWP is due to shear deformations in the soil, the process may be called *residual liquefaction*. For residual liquefaction to occur, the soil must be a loose soil and the permeability must be small. Another type of liquefaction exist, namely *momentarily liquefaction*, involving an upward-directed pressure gradient. However the latter will not be discussed in the content of the present section. See Sumer and Fredsøe (2002) for a detailed description for the physics of liquefaction, both the residual and momentarily liquefaction.

The key findings in the coarse silt experiments may be summarized in the following terms, namely build-up of PWP, liquefaction, dissipation of PWP and compaction front. First the build-up of PWP will be discussed.

Build-up of Pore-water Pressure

Fig. 3.18 presents the PWP time-series for PT 13 ($z = 74.4$ cm below the mudline) together with the associated pile head displacement and the force exerted on the pile head by the driving piston. The PWP is in excess of hydrostatic pressure. Fig. 3.18 clearly shows that the PWP builds-up when the pile motion starts. The pile motion introduce shear deformations in the soil, which leads to rearrangement of the soil grains. This rearrangement happens at the expense of pore volume. The water in the pores are therefore pressurized. Liquefaction may be induced by waves, earthquakes or simply by the cyclic loading of a rocking structure, e.g. a caisson breakwater (Sumer *et al.*, 2008).

The time series also show the behavior of the pile head displacement. It can be noticed that the displacement of the pile head decreases from an initial amplitude $x_D = 3.3$ mm to a more constant amplitude of $x_D = 0.5$ mm. The decrease in the amplitude is clearly associated with the increasing force. The capacity of the piston was simply too small. Finally, the time-series display a sudden offset for both the displacement of the pile head and the force, at about $t = 5$ min. No explanation for this offset has been found. However the effects from the sudden offset and the decreasing amplitude are considered negligible in the analysis of the current experiment, since the analysis should only be regarded as a qualitative analysis.

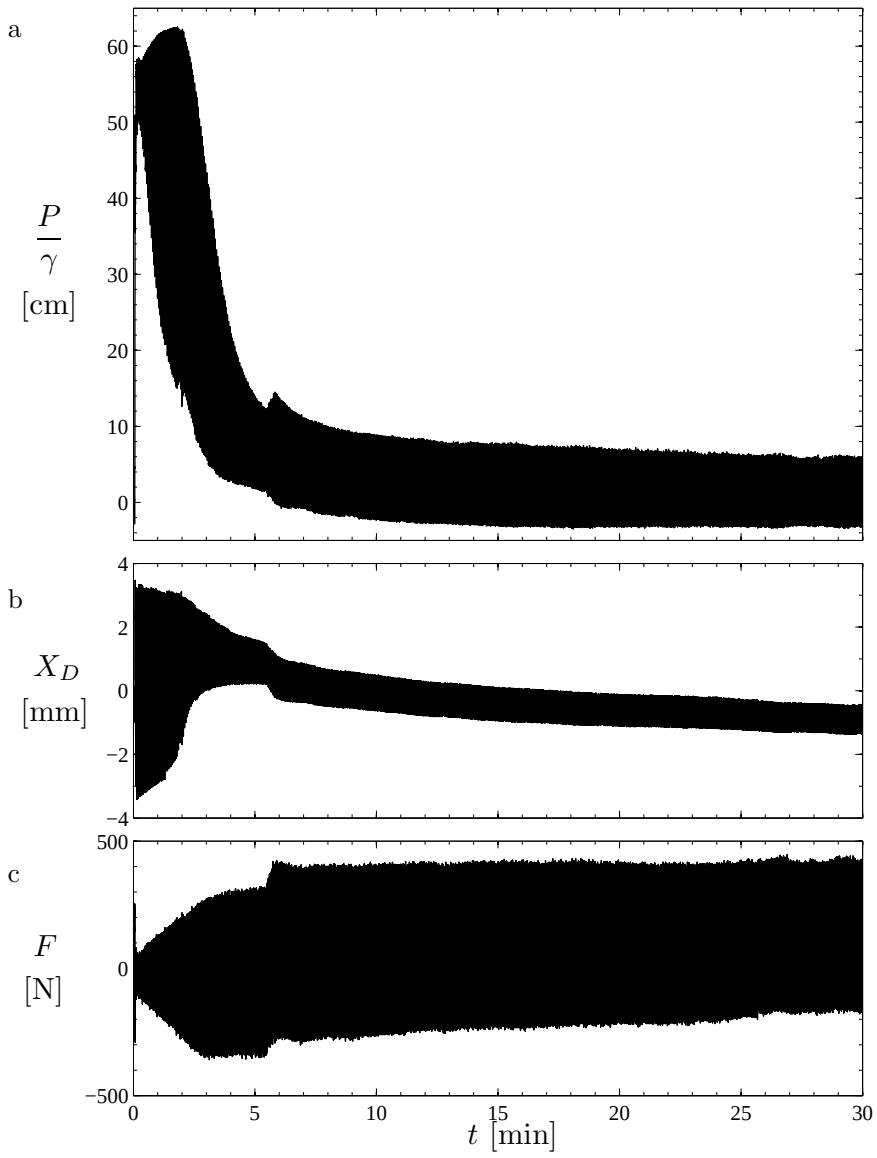

Figure 3.18: *Time-series of coarse silt experiment. a: PWP time-series (PT 13). Measured a at vertical* 2 cm *from the pile. b: Pile head displacement. c: Exerted force*

Liquefaction

Fig. 3.19 displays a close up of the time-series, now including the PWP measured at $z = 11.4$ cm, 31.4 cm, 76.4 cm (PT 7, PT 10 and PT 13). The dotted lines in Fig. 3.19 indicates the onset of liquefaction.

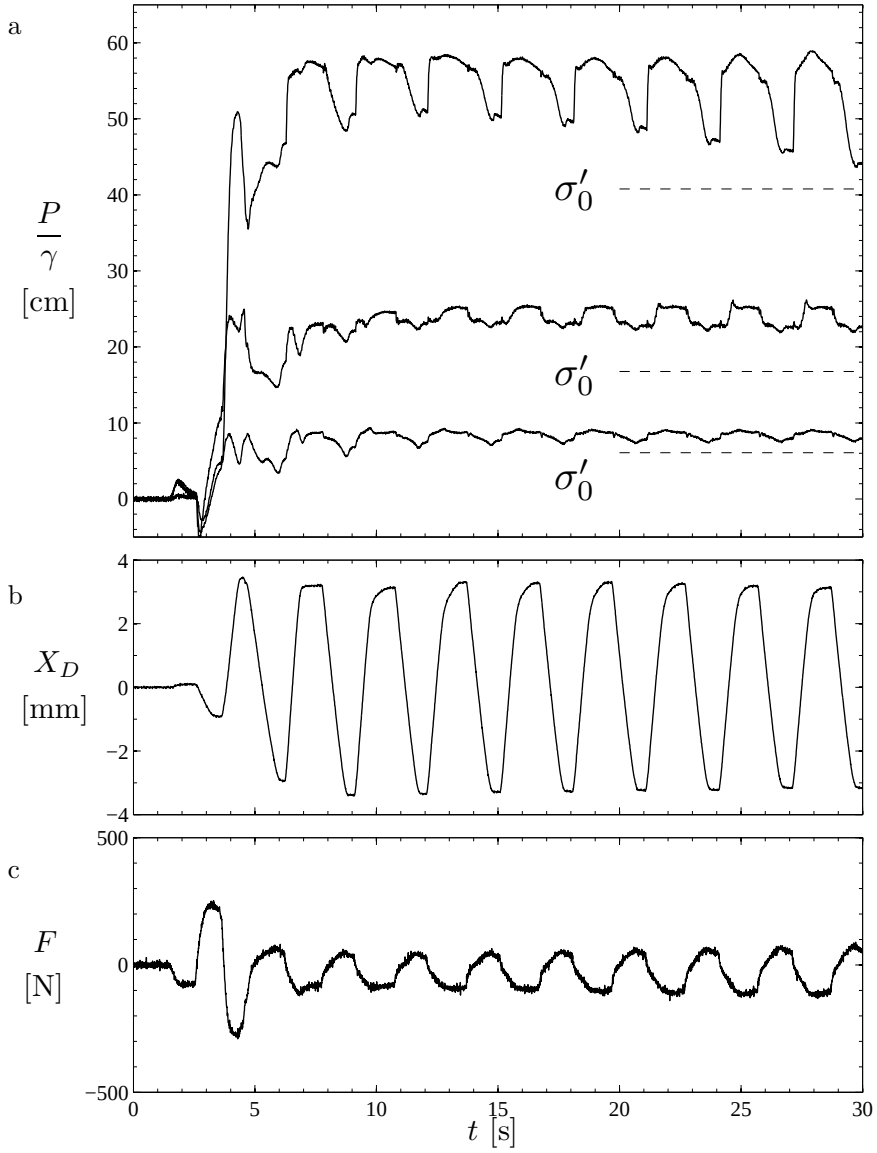

Figure 3.19: *Time-series of coarse silt experiment (Close-up). a: PWP time-series (PT 7, PT 10 and PT 13). Measured a at vertical* 2 cm *from the pile. b: Pile head displacement. (+) pile motion towards the pressure rack c: Exerted force. (+) tension force.*

In the present study, the onset of liquefaction criterion has been taken as the

mean initial effective stress σ'_0, namely,

$$\sigma'_0 = \gamma' z \frac{1 + 2K_0}{3} \tag{3.10}$$

where the coefficient of lateral earth pressure K_0 may by found from Jaky's equation, namely $K_0 = 1 - \sin\varphi$. Recent studies, (Sumer *et al.*, 2012) and (Sumer *et al.*, 2011), have stated that the mean initial effective stress (Eq. 3.10) may be used as a first approximation for the onset of liquefaction. Seen from Fig. 3.19, the PWP builds up and exceeds the criterion for the onset of liquefaction within the first two periods of the pile motion.

Considering the maximum value of the PWP (Fig. 3.20). When the PWP exceeds the criterion for onset of liquefaction, the contact stresses between the soil grains vanish. However, the PWP increases even beyond the criterion for onset of liquefaction. This observation has been discussed in e.g Sumer *et al.* (2006a) among other works. The maximum pressure, when the soil is liquefied may be estimated as follows (Sumer, 2013),

$$P_{max} = (\gamma_{liq} - \gamma) z \tag{3.11}$$

where γ_{liq} is the specific weight of the liquefied soil. When the soil is liquefied, it can be assumed, that the void ratio of the liquefied soil e_{liq} equals the maximum void ratio e_{max}. Therefore the specific weight of the liquefied soil may be determined as (Sumer *et al.*, 2006a),

$$\gamma_{liq} = \frac{S_r + e_{max}}{1 + e_{max}} \gamma \tag{3.12}$$

The level of the maximum pressure P_{max} is shown in Fig. 3.20. It can be seen, that the maximum value the PWP attains, compares well with the maximum pressure P_{max}. However the PWP measured does exceed the maximum pressure defined by Eq. 3.11. It is believed that the discrepancy is related with a non-constant liquefied soil density. Sumer *et al.* (2006a) argued that the liquefied soil density is not constant, but is rather increasing with the soil depth (In Sumer *et al.* (2006a), γ_{liq} was approximately 7% larger at the impermeable bed compared with γ_{liq} obtained from e_{max}). The current results also indicates that γ_{liq} increases with depth.

Pore-water Pressure Dissipation and Compaction Front

Excellent studies on the liquefaction process has been given in e.g. Sumer *et al.* (2006b), including PWP dissipation and compaction of the liquefied soil. However, for completeness of the experimental work with coarse silt, a small discussion on the PWP dissipation and soil compaction will be given herein.

For the analysis of the PWP dissipation and the compaction front, a test, where the stainless steel model pile was replaced with a transparent acrylic

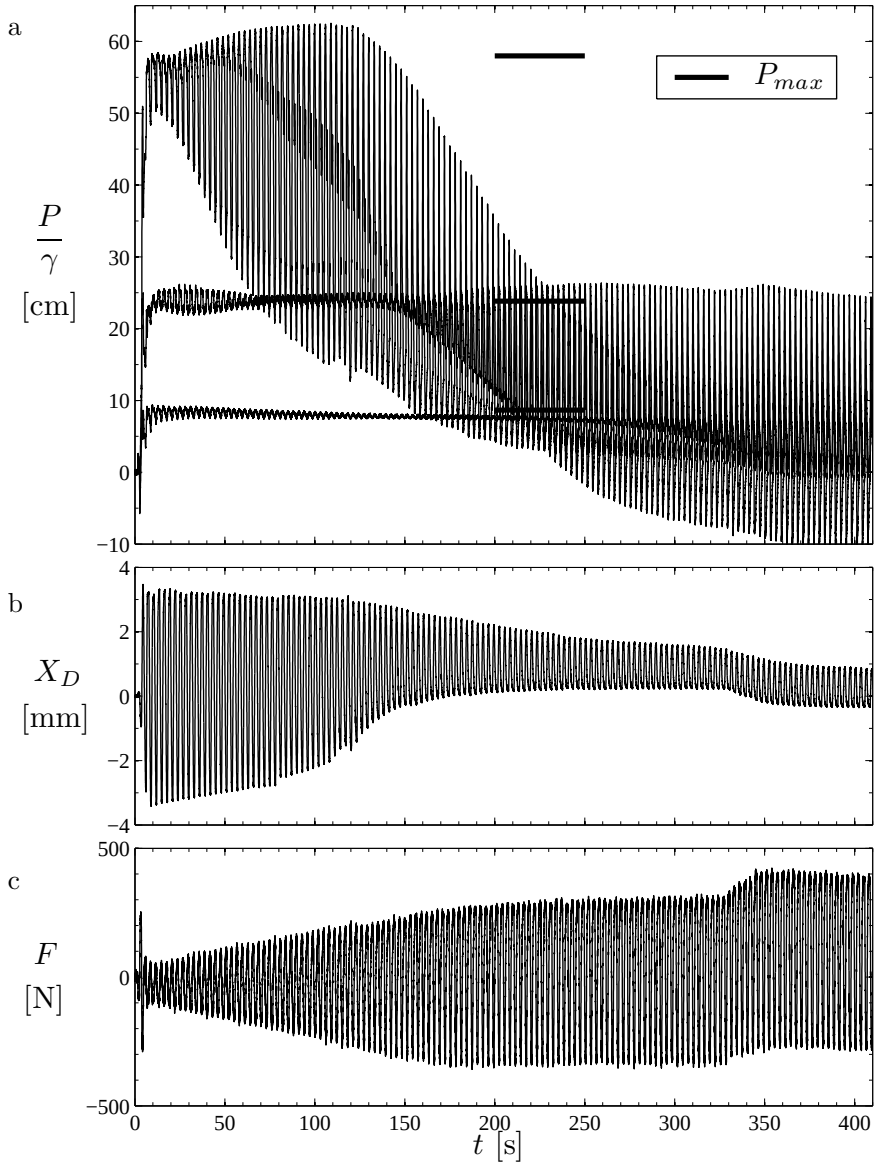

Figure 3.20: *Time-series of coarse silt experiment (A wider zoom). a: PWP time-series (PT 7, PT 10 and PT 13). Measured a at vertical* 2 cm *from the pile. b: Pile head displacement. (+) pile motion towards the pressure rack c: Exerted force. (+) tension force.*

pile, was conducted in order to be able to video monitoring the soil from inside the model pile. The bending stiffness of the acrylic pile was approximately 1.6% of the stainless steel pile. However it is believed that in conjucting with the present analysis, the bending stiffness is of minor importance.

Fig 3.21 shows the period averaged excess PWP (Eq. 3.7) measured at PT 7, PT 10 and PT 13 (z = 10.8 cm, 30.8 cm, 75.8 cm). Also shown is the criterion for onset of liquefaction. Fig. 3.21 covers the entire liquefaction

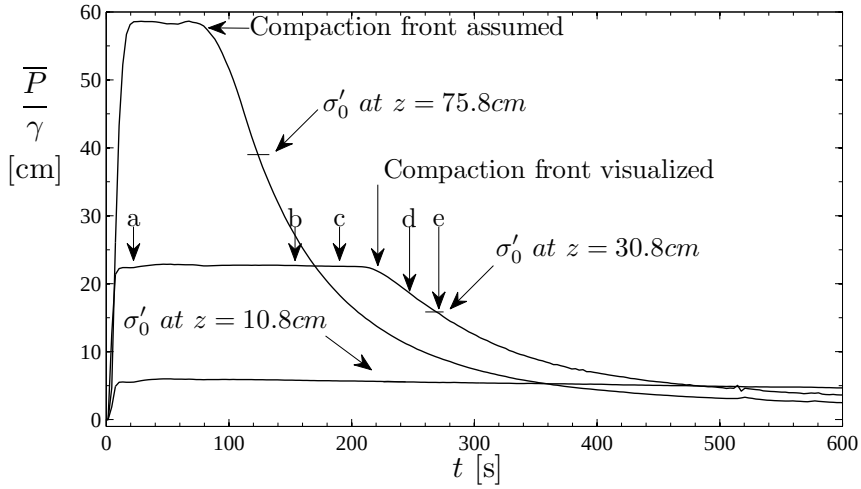

Figure 3.21: *Period averaged PWP for acrylic model pile test.*

process, namely the build-up of PWP, liquefaction, compaction, and dissipation of PWP. For a detailed description for the entire liquefaction process, See Sumer *et al.* (2006b).

When the soil is liquefied, a *compaction front* will appear starting at the impermeable bed, due to settlement of the soil grains and an upward directed flow of pore-water between the soil grains (Sumer *et al.*, 2006b). To monitor the compaction front, a video recording was synchronized with the PWP time series. Fig. 3.23, Fig. 3.24 and Fig. 3.25 show a sequence of snapshots, starting from the soil being liquefied to compaction of the liquefied soil, including the progression of the compaction front.

When the soil is liquefied, the soil grains begins to move downwards towards the impermeable base. The fall velocity of the soil grains decreases as the liquefaction process continues. Initially the fall velocity of the soil grains is approximately 1.4 mm/s. Prior the arrival of the compaction front, the fall velocity of the soil grains have decreased, now being approximately 0.3 mm/s. The decrease of the fall velocity is associated with the so-called hindered settlement (Fredsøe and Deigaard, 2002). As liquefaction continues, the concentration of soil particles increase.

Considering Fig. 3.25.f. Here the progress of the compaction front is visualized. The compaction front develops in an approximately 50° angle, starting from the lower right corner. This may be explained with reference to Fig. 3.22. During the rocking of the pile, the soil in the vicinity of the pile, is exposed to shear deformations. However, the shear deformations are most pronounced in front of the pile, whereas at an angle 90° to the pile, the shearing will be less pronounced. Therefore, it is likely for the soil to liquefy deeper in front of the pile compared to 90° of the pile. When the compaction front progress, it will be with an angle due to the difference in liquefaction depth.

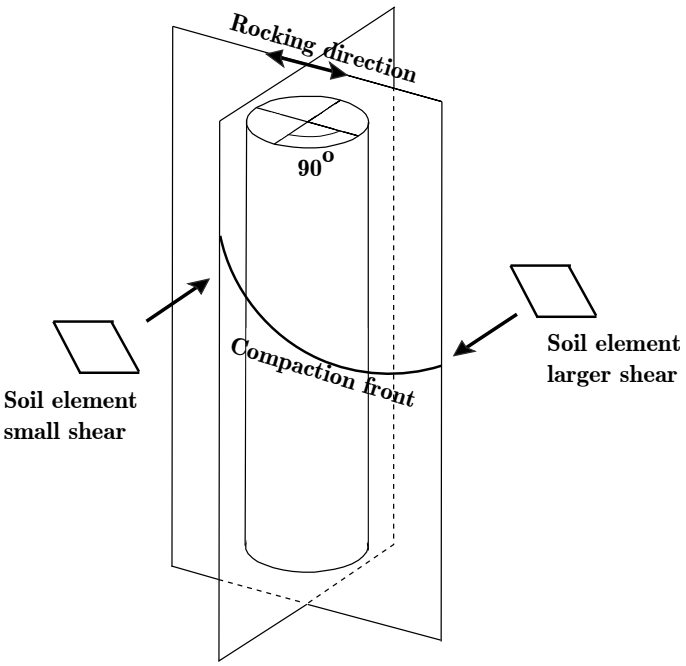

Figure 3.22: *Schematic of the liquefaction front around the pile.*

Finally, the velocity of the compaction front may be estimated from Fig. 3.21 and Fig. 3.25.f. The compaction front arrives at $z = 30.8$ mm at approximately $t = 227$ s. This correspond to the time instant, where the period-average PWP starts to decrease. Even after the compaction front has passed, the soil is still liquefied (Fig. 3.21). Assuming that the compaction front arrives when the period averaged PWP at $z = 75.8$ mm starts to decrease, the velocity of the compaction front can be estimated from the distance between the pressure tappings.

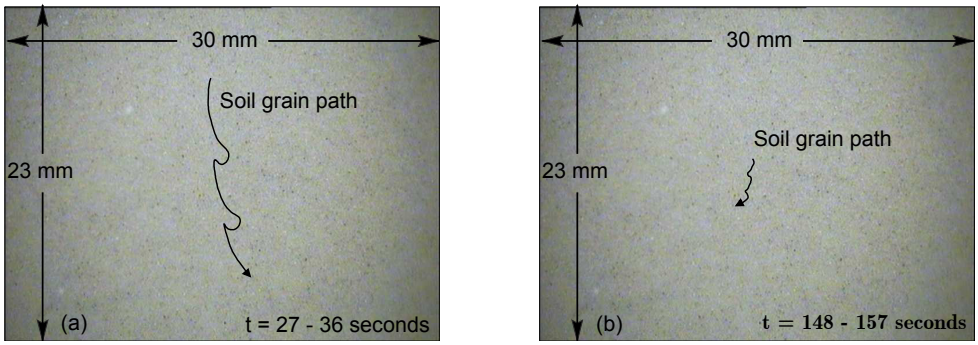

Figure 3.23: *(a-b): Sequence of the liquefaction process.*

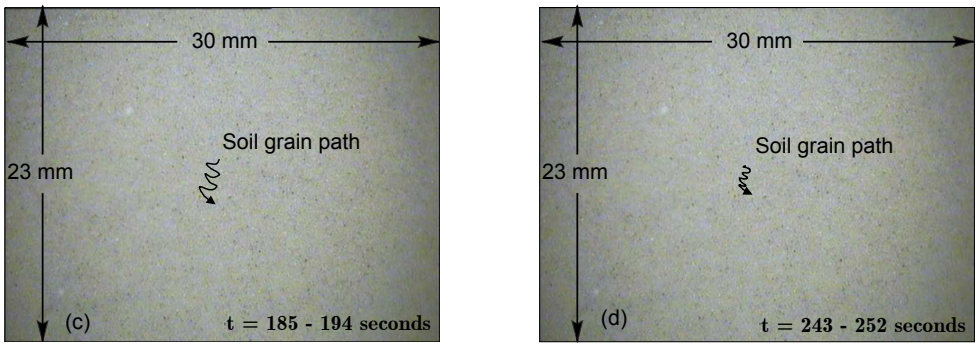

Figure 3.24: *(c-d): Sequence of the liquefaction process.*

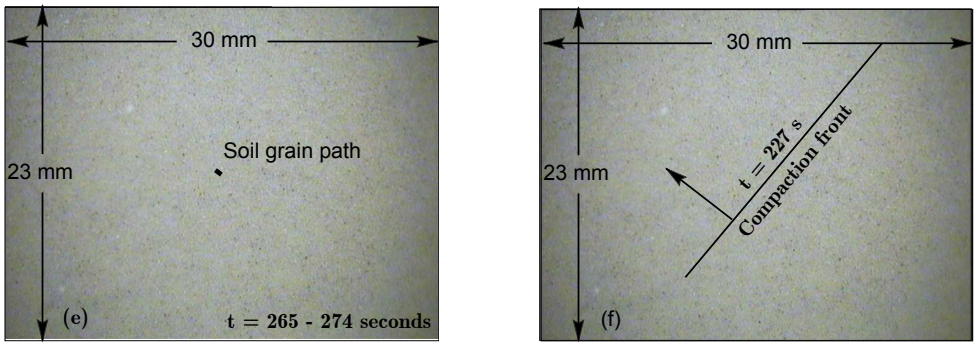

Figure 3.25: *(e): Sequence of the liquefaction process. (f) Visualization of the progressive compaction front.*

The velocity of which the pressure is dissipated, may also be estimated in the same way. The results are summarized in Tab. 3.4. It is seen, that the velocities of the compaction front and the PWP dissipation, are nearly identical to a first approximation. From Fig. 3.21 it may be noticed, that the soil at $z = 10.8$ cm appear to be non-liquefied before the soil at $z = 30.8$ cm. This is not expected. It is believe that the criterion of liquefaction is wrongly estimated.

	Compaction front	PWP dissipation
PT13-PT10	3.3 mm/s	3.2 mm/s

Table 3.4: *Comparison of the velocity of the compaction front and the PWP dissipation.*

Chapter 4

Model Validation

The validation of the numerical model had to rely on a comparison between the numerical model and the data obtained from the experimental work since neither analytical solutions or experimental data currently exist (to the authors knowledge). To support the validation of the numerical model, a simple test case (TC) was run with the objective of validating the numerical solution of the Biot's consolidation equations against existing analytical solutions.

4.1 Wave-induced pore-water pressure under Progressive Waves

In the test case (TC) used, a 2D isotropy seabed under progressive waves was considered. Fig. 4.1 shows the schematic of the test case.

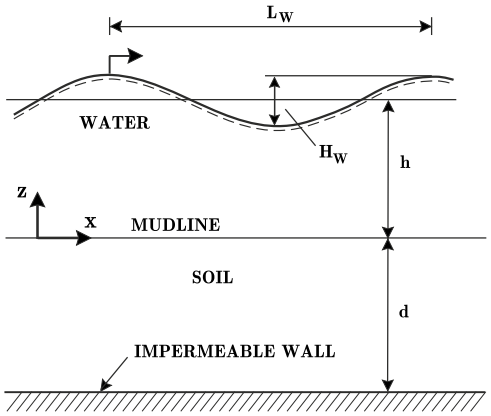

Figure 4.1: *Skectch of test case for soil response in a seabed of finite thickness under progressive waves. For seabed response of infinite thickness, the walls surrounding the seabed, were replaced by the infinite elements.*

Both soil response in a seabed of finite thickness and infinite thickness was

considered. For soil response in the seabed of infinite thickness, the walls surrounding the seabed were replaced by infinite boundary elements (Sec. 2.3.2).

For the soil response in a seabed of finite thickness, the vertical walls surrounding the seabed were treated as slip impermeable walls. This implies that the normal displacement on the side walls is zero. However by extending the width W of the seabed, the effect from the vertical boundary conditions becomes negligible. At the bottom of the seabed a no-slip condition was assumed. Finally zero flux of the PWP through any of the walls was assumed. The boundary conditions for the soil displacements at the bottom of the seabed and the zero pressure gradients are similar to the ones used in Liu and Garcia (2007),

$$u = 0 \quad at\ x = [0, W] \tag{4.1}$$

$$u = v = 0 \quad at\ x = -d \tag{4.2}$$

$$\frac{\partial P}{\partial x} = 0 \quad at\ x = [0, W] \tag{4.3}$$

$$\frac{\partial P}{\partial y} = 0 \quad at\ z = -d \tag{4.4}$$

where u and v are the components of the soil displacements in the x-direction and z-direction and P is the excess pore-water pressure (PWP). To simulate seabed infinity in the x-direction, a seabed width of 24 m was used. The thickness of the seabed was expressed as $d = bL_W$ where L_W denotes the wave length and $b = 0.25, 0.50, 0.75, 1.00$. The wave length $L_W = 1.25$ m, wave height $H_W = 0.0524$ m and the wave period $T_W = 0.9$ s. The water depth $h = 0.533$ m. The true bulk modulus of elasticity of pore-water $K_w = 2 \cdot 10^9$ N/m^2 and the density of the water $\rho_w = 1030$ kg/m^3.

At the mudline the soil displacements were free to move and the PWP equaled the pressure exerted on the bed by the progressive waves p_o,

$$p_0 = p_b \cdot e^{i(\lambda x - \omega t)} \tag{4.5}$$

where λ is the wave number and where the amplitude of the pressure p_b exerted on the bed by the progressive waves is given by,

$$p_b = \gamma \frac{H_W}{2} \frac{1}{\cosh \lambda \cdot h} \tag{4.6}$$

where γ is the specific weight of water. The soil parameters used in the present validation exercise were porosity $n = 0.4$, permeability coefficient $k = 8.4 \cdot 10^{-4}$ m/s, Poisson's ratio $\nu = 0.25$, saturation degree $S_r = 0.95$, soil density $\rho = 1483$ kg/m^3 and soil Young's modulus $E = 4.8 \cdot 10^7$ N/m^2

4.1.1 Solution to the Biot Consolidation Equations for Finite Depth

Analytical solutions for the wave-induced soil response in an unsaturated anisotropic seabed of finite thickness, based on Biot's consolidation equations, were presented by Hsu and Jeng (1994). Solutions for soil response under progressive waves, as well as standing waves, for both saturated and unsaturated conditions were presented. The wave-induced PWP from progressive waves is given by,

$$\begin{aligned} P &= \frac{p_b}{(1-2\nu)}\{(1-\chi-2\nu)(C_2e^{\lambda z}-C_4e^{-\lambda z}) \\ &+ (1-\nu)(\delta^2-\lambda^2)(C_5e^{\delta z}+C_6e^{-\delta z})\}e^{i(\lambda x-\omega t)} \end{aligned} \tag{4.7}$$

and the effective normal stresses are given by,

$$\begin{aligned} \sigma'_x = &- p_b\Bigg\{\left[(C_1+C_2\lambda z)+\frac{2\nu\chi}{1-2\nu}C_2\right]e^{\lambda z}+\left[(C_3+C_4\lambda z)\right. \\ &\left.-\frac{2\nu\chi}{1-2\nu}C_4\right]e^{-\lambda z}+\left[\lambda^2-\frac{(\delta^2-\lambda^2)\nu}{1-2\nu}\right] \\ &(C_5e^{\delta z}+C_6e^{-\delta z})\Bigg\}e^{i(\lambda x-\omega t)} \end{aligned} \tag{4.8}$$

$$\begin{aligned} \sigma'_z = &p_b\Bigg\{\left[(C_1+C_2\lambda z)-\frac{2\chi(1-\nu)}{1-2\nu}C_2\right]e^{\lambda z}+\left[(C_3+C_4\lambda z)\right. \\ &\left.+\frac{2\chi(1-\nu)}{1-2\nu}C_4\right]e^{-\lambda z}+\frac{1}{1-2\nu}\left[\delta^2(1-\nu)-\lambda^2\nu\right] \\ &(C_5e^{\delta z}+C_6e^{-\delta z})\Bigg\}e^{i(\lambda x-\omega t)} \end{aligned} \tag{4.9}$$

where δ is a combined wave and soil parameter, χ is a dimensionless parameter indicating the soil anisotropy and degree of saturation and C_i is a set of coefficients. For an isotropy unsaturated soil, δ and χ can be expressed as,

$$\delta^2 = \lambda^2-\frac{i\omega\gamma}{k}\left[n\beta+\frac{(1-2\nu)}{2G(1-\nu)}\right] \tag{4.10}$$

$$\chi = \frac{(1-2\nu)n\beta}{n\beta+\frac{1-2\nu}{G}} \tag{4.11}$$

In the case of a completely saturated isotropy soil ($S_r = 1$), the compressibility of the pore fluid $\beta \to 0$ (defined as G/K'), hence the dimensionless parameter $\chi \to 0$. The combined wave and soil parameter δ reduces to,

$$\delta^2 = \lambda^2-\frac{i\omega\gamma(1-2\nu)}{2k(1-\nu)G} \tag{4.12}$$

For further details of the analytical solutions and the constants C_i, See Hsu and Jeng (1994). The computation of the constants C_i was based on the source-code kindly provided by Professor Dong-Sheng Jeng of the University of Dundee (UK).

Solution for Saturated Soil

The numerical solution to the Biot consolidation equations compared to the analytical solutions of Hsu and Jeng (1994) is shown in Fig. 4.2. Plotted is

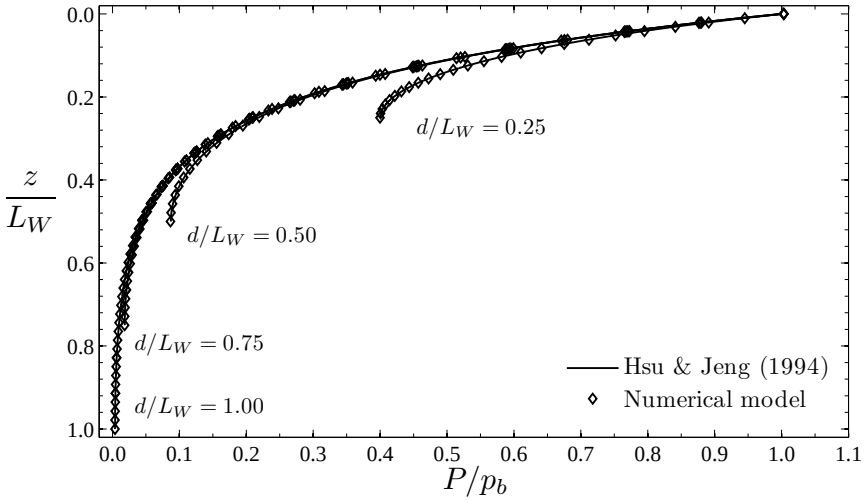

Figure 4.2: *Vertical excess pore-water pressure distributions for an isotropy saturated seabed of finite depth. Comparison between present numerical solution and the analytical solution from Hsu and Jeng (1994).*

the vertical distribution of the PWP (normalized by the maximum pressure at the mudline p_b) at $\omega t = \pi/2$. The results are in good agreement, thus validating the numerical solution when neglecting the compressibility of water including the gas/air content ($\partial P/\partial t = 0$). The effects from wall proximity are clearly seen as depth decreases. The gradient of the excess PWP is indeed null at the bottom of the seabed.

The effective normal stresses σ'_x and σ'_z together with the PWP for a soil depth of $d = 0.50L_W$ are shown in Fig. 4.3. Again the numerical and analytical results are in fine agreement.

Solution for Unsaturated Soil

Following the same line as for the case of fully saturated conditions, the vertical distribution of PWP, in the case of unsaturated conditions, is shown in Fig. 4.4.
It can be noticed that the results are in fine agreement with the analytical

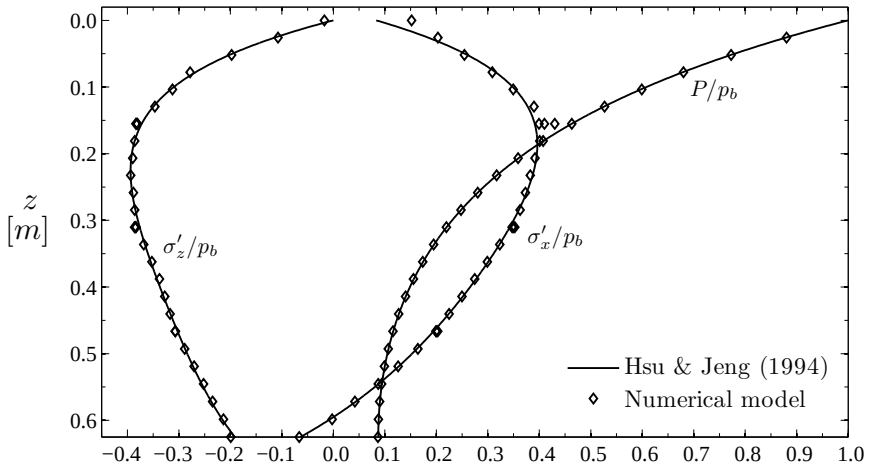

Figure 4.3: *Vertical distribution of the normal effective stresses and excess pore-water pressure for a saturated soil depth of $d = 0.5L_W$. Comparison between present numerical solution and analytical solution from Hsu and Jeng (1994).*

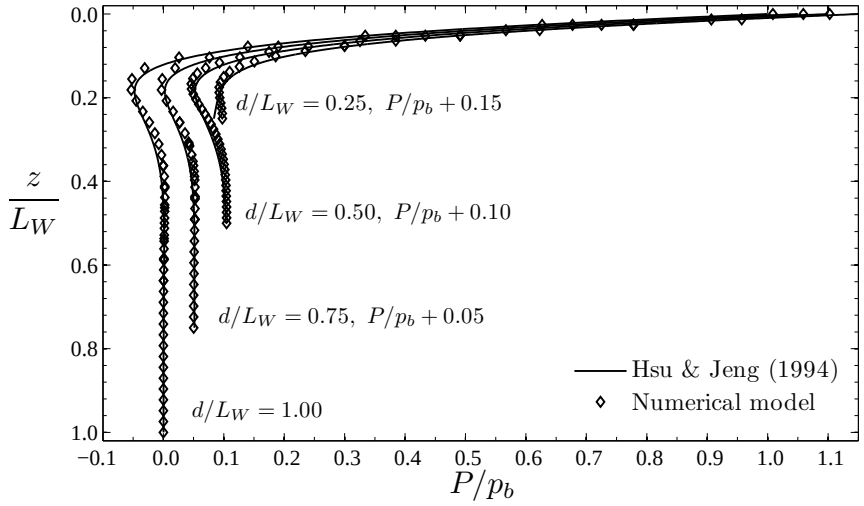

Figure 4.4: *Vertical excess pore-water pressure distributions for an isotropy unsaturated seabed of finite depth. Comparison between present numerical solution and the analytical solution from Hsu and Jeng (1994).*

solutions from Hsu and Jeng (1994), although small discrepancies can be observed. Especially for a soil depth of $d = 0.25L_W$. However, from the results, it can be concluded that the numerical solution of the Biot equations seems valid. Regarding the effective normal stresses, σ'_x and σ'_z, the comparison with the analytical solution shows fine agreement (Fig. 4.5).

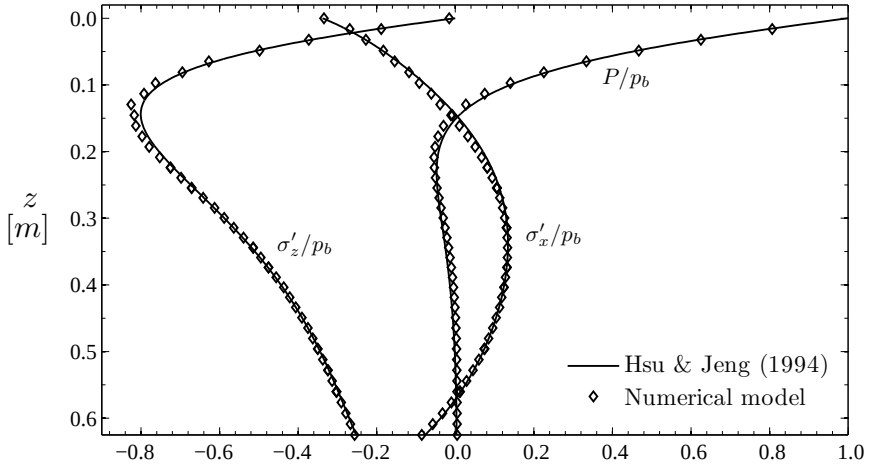

Figure 4.5: *Vertical distribution of the normal effective stresses and excess pore-water pressure for a unsaturated soil depth of $d = 0.5L_W$. Comparison between present numerical solution and analytical solution from Hsu and Jeng (1994).*

4.1.2 Solution to the Biot Consolidation Equations for Infinite Depth

The soil response in an unsaturated and fully saturated seabed of infinite thickness based on the Biot consolidation equations, has been calculated by various authors, e.g Madsen (1978), Yamamoto *et al.* (1978), Mei and Foda (1981) and Hsu *et al.* (1993). Here, the solution by Mei and Foda (1981) is adopted. The wave-induced PWP and effective normal stresses in an infinite seabed under progressive waves are given by,

$$\tilde{p} + \hat{p} = \left\{ \frac{1}{1+m} e^{\eta} + \frac{m}{1+m} e^{\frac{(1-i)\eta}{\sqrt{2}\varepsilon}} \right\} e^{i(\zeta-\tau)} \tag{4.13}$$

$$\tilde{\sigma}_x + \hat{\sigma}_x = \left\{ \left[\frac{-m}{1+m} - \eta \right] e^{\eta} + \frac{\nu}{1-\nu} \frac{m}{1+m} e^{\frac{(1-i)\eta}{\sqrt{2}\varepsilon}} \right\} e^{i(\zeta-\tau)} \tag{4.14}$$

$$\tilde{\sigma}_z + \hat{\sigma}_z = \left\{ \left[\frac{-m}{1+m} + \eta \right] e^{\eta} + \frac{m}{1+m} e^{\frac{(1-i)\eta}{\sqrt{2}\varepsilon}} \right\} e^{i(\zeta-\tau)} \tag{4.15}$$

where the sum $\tilde{p} + \hat{p}$ is the PWP normalized with the pressure at the bed. The sums $\tilde{\sigma}_x + \hat{\sigma}_x$ and $\tilde{\sigma}_z + \hat{\sigma}_z$ are the effective normal stresses in horizontal and vertical direction respectively, normalized with the bed pressure. The

stiffness ratio m is given by,

$$m = \frac{nG}{(1-2\nu)\beta} \tag{4.16}$$

In non-dimensional form, the soil depth $\eta = -z/(L_W/(2\pi))$ and the boundary layer thickness $\varepsilon = \delta/(L_W/(2\pi))$ where δ is given as,

$$\delta = \sqrt{\frac{k}{\omega}} \left\{ \frac{n}{\beta} + \frac{1}{G} \frac{1-2\nu}{2(1-\nu)} \right\}^{-1/2} \tag{4.17}$$

Finally $\zeta = kx$ and $\tau = \omega t$.

Solution for Saturated Soil

The numerical solution for saturated soil response for infinite depth, compared with the analytical solution from Mei and Foda (1981) is shown in Fig. 4.6. In general the numerical solution is in fine agreement with the analytical solutions. Small deviations near the bottom of the seabed are seen. It should be noticed that the solution for $d = 0.25L_W$ is not shown. The numerical solution for this case did not converge.

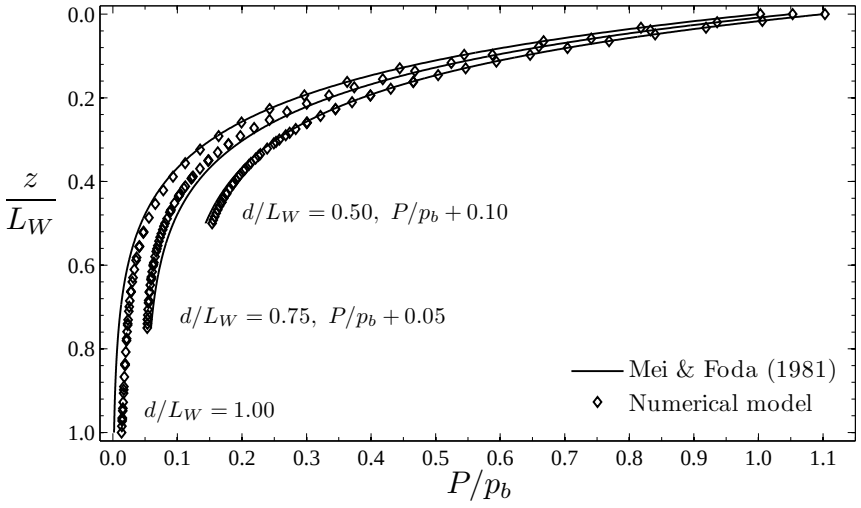

Figure 4.6: *Vertical excess pore-water pressure distributions for an isotropy saturated seabed of infinite depth. Comparison between present numerical solution and the analytical solution from Mei and Foda (1981).*

Also the vertical normal stress distributions are shown in Fig. 4.7, together with the PWP for $d = 0.5L_W$. The numerical solution compares well with the analytical solution. From this it may be concluded, that the use of *infinite boundary elements* as described in Sec. 2.3.2 seems to be a possible solution to simulate infinitely large soil domains.

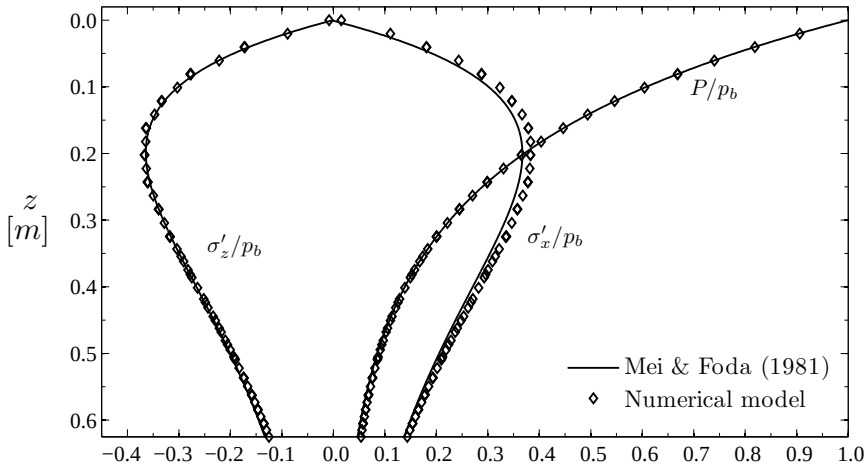

Figure 4.7: *Vertical distribution of the normal effective stresses and excess pore-water pressure for a saturated soil depth of $d = 0.5L_W$. Comparison between present numerical solution and analytical solution from Mei and Foda (1981).*

Solution for Unsaturated Soil

The unsaturated soil response in infinite depth is shown in Fig. 4.8. The numerical solution compares well with the analytical solution of Mei and Foda (1981). The deviations are slightly larger compared with the soil response of finite depth.

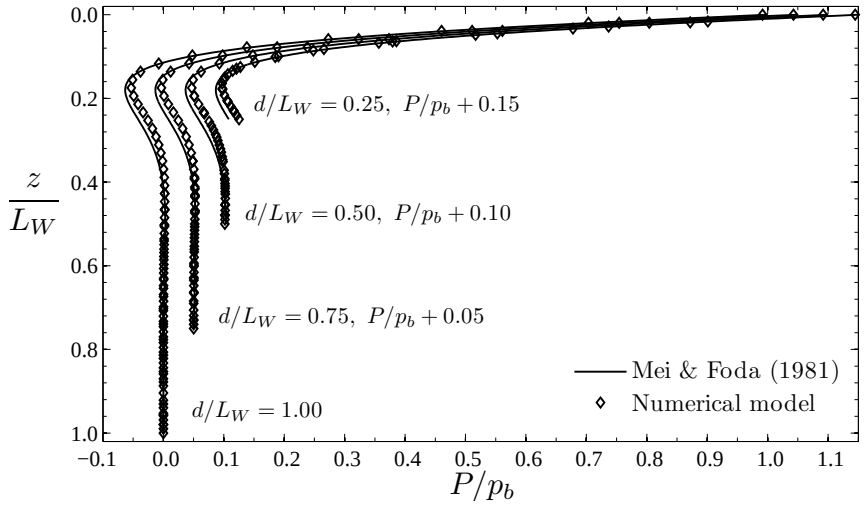

Figure 4.8: *Vertical excess pore-water pressure distributions for an isotropy unsaturated seabed of infinite depth. Comparison between present numerical solution and the analytical solution from Mei and Foda (1981).*

The vertical normal stress distributions are shown in Fig. 4.9. The normal

effective stress distribution in the x-direction is seen not to compared well with the numerical solution. However it is the authors belief that the analytical solution, for this particular set of test conditions, is not able to capture the correct effective normal stresses in the horizontal direction (σ'_x) along a vertical line. To support this statement, the following should be noticed.

The present case is similar to the case of unsaturated soil response for finite soil depth (Sec 4.1.1) except that the bottom of the seabed is infinite. Therefore the effective normal stress distributions should be comparable, at least near the mudline. In the present case the effective normal stresses near the mudline computed from the numerical model, are indeed comparable, although not the same (Fig. 4.5 and Fig. 4.9). Therefore the numerical solution seems more valid than the analytical solution for the present set of conditions.

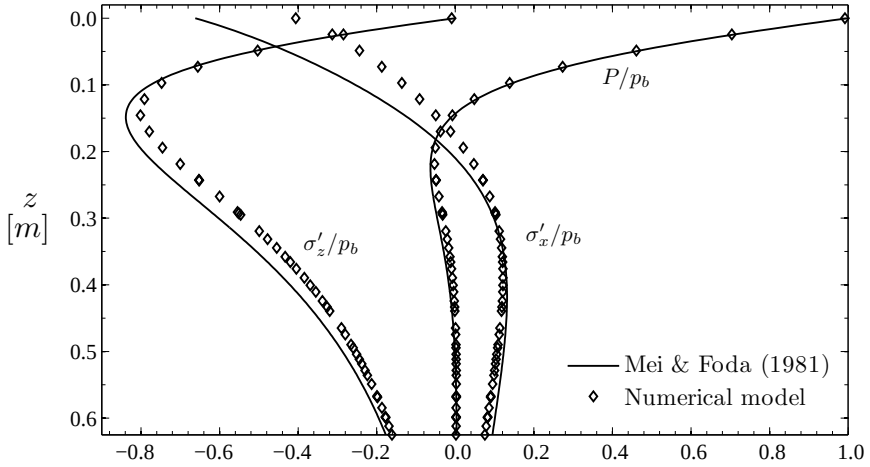

Figure 4.9: *Vertical distribution of the normal effective stresses and excess pore-water pressure for a unsaturated soil depth of $d = 0.5L_W$. Comparison between present numerical solution and analytical solution from Mei and Foda (1981).*

4.2 Cyclic Motion of Monopile Foundation

In this section, the numerical model is validated against the experimental data for the coarse sand experiments. The background for the numerical model is presented in chap. 2.

4.2.1 Model Geometry and Boundary Conditions

Fig. 4.10 shows a 3D representation of the geometry implemented in the numerical model validation exercise (only showing the one half of the geometry). The dimensions of the numerical model are identical as those in the experimental test.

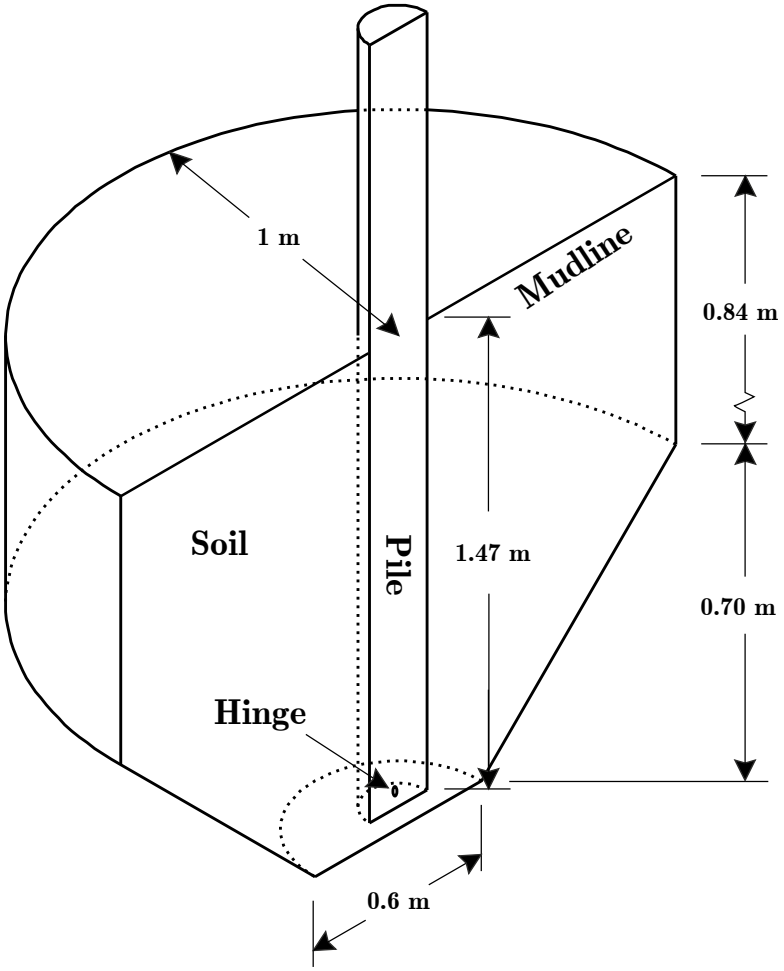

Figure 4.10: *3D representation of model geometry used for model validation exercise. Only one half of the geometry is shown.*

The side walls and the bottom of the soil were modelled as smooth rigid impermeable walls, thus no normal directed soil displacements, nor flux of PWP

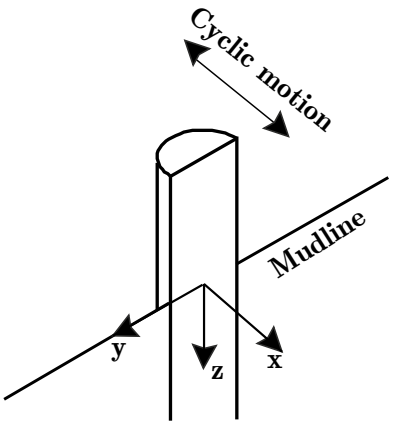

Figure 4.11: *3D representation of model geometry used for model validation exercise (close up).*

were allowed through the walls. See Sec. 2.3.1 for further description. The pile toe was supported by a hinged connection allowing the pile to rotate. See Sec. 2.3.3. The hinge introduce reaction forces in the hinge. However, for the present validation exercise, this is not important, since only the PWP is considered. The pile soil interface was considered as a no-slip interface. The consequence is discussed in Sec. 4.2.3. At the mudline, soil displacements are not constrained and the PWP is null (in excess of hydrostatic pressure).

4.2.2 Input Parameters

The input parameters are listed in Tab. 4.1. From the strain gauge readings (Sec. 3.3.1), it could be concluded, that the model pile behaved as a rigid pile (only small deflections were observed). To ensure a rigid pile response in the numerical calculations, the pile's Young's modulus is increased significantly compared to the model pile.
The input parameters are identical to the soil properties determined from the soil investigations (Sec. 3.2). Young's modulus of the soil was expressed by Eq. 3.5.

The pile head displacement measured in the experimental test (Sec. 3.3.1) was used as input for the pile head displacement in the numerical model, where the peak displacement $< x_D >= 0.0018$ m and the period $T = 3$ s. It should be noticed that the pile head displacement was taken as the ensemble-averaged displacement, namely $< X_D >$ defined in Eq. 3.3 for 40 consecutive periods.

Parameter	Symbol	Value	Unit
Peak displacement	$< x_D >$	0.0018	$[m]$
Period	T	3.0	$[s]$
Young's modulus (Pile)	E_p	$2 \cdot 10^{13}$	$[Pa]$
Poisson's ratio (Pile)	ν_p	0.33	$[-]$
Density (Pile)	ρ_p	7850	$[kg/m^3]$
Relative density	D_r	0.55	$[-]$
Porosity	n	0.42	$[-]$
Saturation degree	S_r	1	$[-]$
Permeability coefficient	k	0.0037	$[m/s]$
Young's modulus (Soil)	E	see text	$[Pa]$
Poisson's ratio (Soil)	ν	0.20	$[-]$
Density (Soil)	ρ	968	$[kg/m^3]$
Bulk modulus (Water)	K_w	$2.3 \cdot 10^9$	$[Pa]$
Acceleration of gravity	g	9.81	$[m/s^2]$

Table 4.1: *Input parameters used for model validation.*

4.2.3 Time-Series Validation of Pore-water Pressure

Fig. 4.12.a shows the applied pile head displacement for both the experimental data and the numerical computations, while Fig. 4.12.b shows the associated velocity of the pile head displacement for two consecutive periods. Fig. 4.12.c shows the time-series of the PWP, at a distance of 2 cm from the pile, 31.5 cm below the mudline (PT 10). In the following the symbol P will denote both the ensemble-averaged PWP $< P >$ from the experiments, and the PWP computed from the numerical model.

From the PWP comparison, the following observations may be noticed; 1) the PWP and the velocity of the pile head displacement $< V_D >$ are in phase. This may easily be seen at the zero-crossings. This supports the fact that the soil during the experimental test was indeed fully saturated. 2) The computed PWP coincides fairly well for a narrow range of the PWP time-series, namely $t = 2.40$ s $- 2.65$ s in the first period, and likewise $t = 5.40$ s $- 5.65$ s in the second period. For the remaining part of the time-series, the experimentally measured PWP and the computed PWP are significantly different. The explanation for this discrepancy is as follows,

One significant difference between the numerical model and the experimental test, is the pile/soil interface. In the numerical model, a no-slip interface was used, whereas in the experimental test, a gap between the pile and the surrounding soil forms when the pile moves away from the soil. This gap forms twice during one period (Fig. 4.13). Now returning to the comparison exercise. The range, in which the two time-series collapse, is the

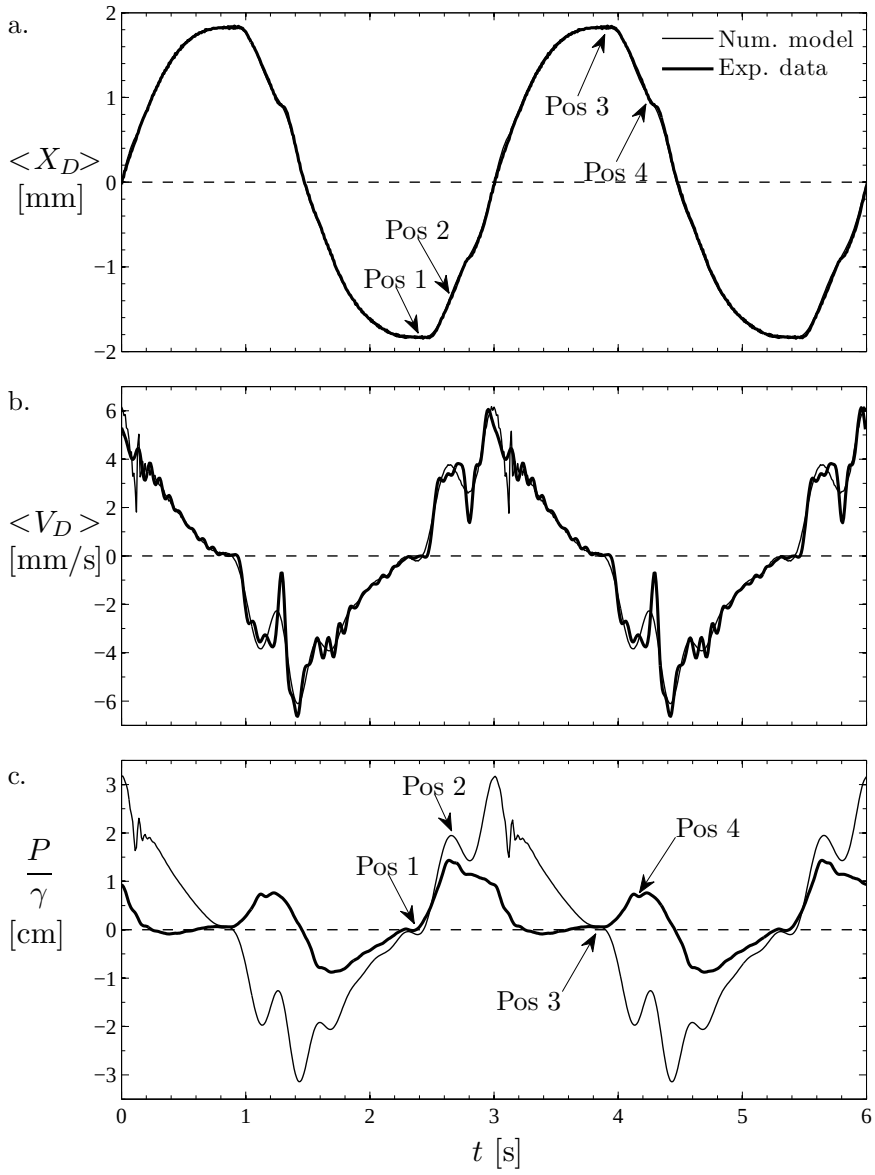

Figure 4.12: *Time-series of PWP at PT 10. Numerical model results and experimental data compared. a: Pile head displacement, b: Pile head velocity,* $< V_D >$ *denotes the velocity* $d < X_D > /dt$ *and c: PWP.* $z = 31.5$ cm, $r = 2$ cm.

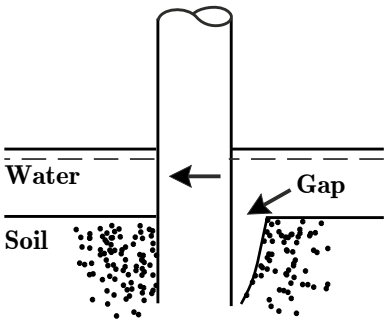

Figure 4.13: *Illustration of gap forming at the backside of the pile. The gap is grossly exaggerated for illustration purposes.*

range where the interface between the pile and the soil in the experimental tests, resembles the pile/soil interface in the numerical model (*position 1* and *position 2*). See Fig. 3.11. Once the gap in the experimental test forms (between *position 2* and *position 3*), the model fails to simulate the measured PWP. Between *position 3* and *position 4* no gap is formed. Here it would be expected that the two time-series once again collapse. However, in the numerical model there is a no-slip condition at both pile walls. In the experimental test, the no-slip condition is only maintained at the pile wall in the far field. The effect from the no-slip interface at the pile wall in the far field is seen as the PWP is pressurized, whereas the effect from the no-slip condition in the near field, in the numerical model, is seen as suction in the PWP time-series.

4.2.4 Model Tuning

From Sec 4.2.3, it could be seen that the numerical model predicts the PWP well in the range $t = 2.40\,\text{s} - 2.65\,\text{s}$. The PWP in the numerical model, is approximately 37% larger than the measured PWP in the experimental test. In this section, the numerical model was tuned to fit the experimental measured data for the range $t = 2.40\,\text{s} - 2.65\,\text{s}$.

The numerical model includes three groups of parameters. First group contains the loading parameters, the second group contains the length and dimensions of the model (foundation depth, pile length etc.) and the third group contains the soil properties. Among the three groups, the soil properties are considered as being attached with the most uncertainty. Therefore, tuning of the numerical model was done via the soil properties.

The soil properties included in the numerical model (included in Biot's consolidation equations) are the following; the shear modulus G, the Poisson's ratio ν, the permeability of the soil k, the saturation degree S_r, the porosity n, the specific weight of the water γ and the true bulk modulus of

elasticity of water K_w. From the coarse sand test, it was concluded that the saturation degree indeed was unity. Therefore the saturation degree S_r will be a constant. The elastic bulk modulus of water Kw is a well determined quantity and is therefore considered as a constant. The parameters G, ν, γ and n was seen to have little influence on the soil response. Therefore only the permeability k was considered as tuning parameter.

Fig. 4.14 shows the PWP at PT 10 for both the numerical model and the experimental data. In the numerical model, three different values of soil permeability were tested, namely $k = 0.33$ cm/s, $k = 0.40$ cm/s and $k = 0.48$ cm/s. The first two permeabilities tested, correspond to the range of measured permeabilities from appendix B, while the latter is the permeability needed in order to achieve coinciding results within 5%.

A permeability coefficient of $k = 0.48$ cm/s may be justified as follows. From appendix B, the permeability as function of void ratio e was determined as,

$$k = 0.53 \cdot e - 0.009 cm/s \tag{4.18}$$

However another relation between the void ratio e and k exist (Ovesen *et al.*, 2007, pg. 66),

$$k_1 = \frac{(1+e_1)e_1^2}{(1+e_2)e_2^2} k_2 \tag{4.19}$$

where k_1 and k_2 is the permeability coefficient at the void ratios e_1 and e_2. Adopting a permeability $k_1 = k_{emin} = 0.33$ cm/s where $e_{min} = 0.64$, the permeability at $e_{insitu} = 0.73$ would theoretically be $k_{insitu} = 0.45$ cm/s thus not far from the value used in the tuned model.

4.2.5 Vertical Distribution of Pore-Water Pressure

The vertical PWP distributions from the experimental data (Sec. 3.3.1) are compared with the PWP computed at time $t = 2.65$ s (Fig. 4.15 and Fig. 4.16). Here the tuned model $k = 0.48$ cm/s is considered. It can be seen, that the shape of the vertical PWP distribution are in principle identical. However, as the vertical distance from the mudline is increased, the results deviates substantially.

No clear explanation for this discrepancy has been found. However the pile in the numerical model behaves more rigid than the model pile in the coarse sand experiments (approximately 50 times more rigid). This may explain the discrepancy, a less rigid pile would impose smaller strains on the soil elements. No further investigation of this has been carried out.

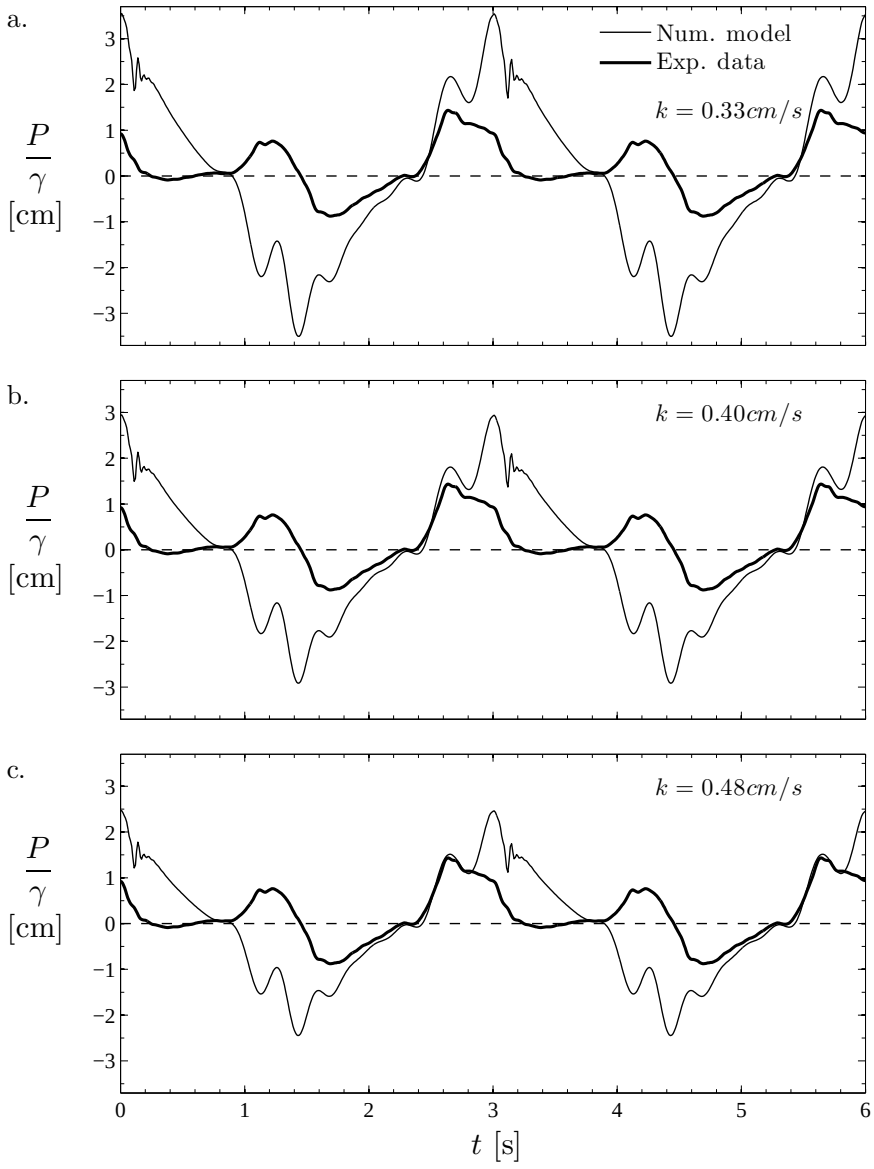

Figure 4.14: *Results for the model tuning exercise of PWP,* $z = 31.5$ cm, $r = 2$ cm

Finally, it should be noticed that in the coarse sand experiments, the PWP decreases as the distance to the pile wall is increased. In the numerical model, the PWP increases as the distance to the pile increases. The latter is unexpected and is related to the reflective boundaries used to simulate the wall of the tank. The reflective boundaries can be avoided using infinite elements.

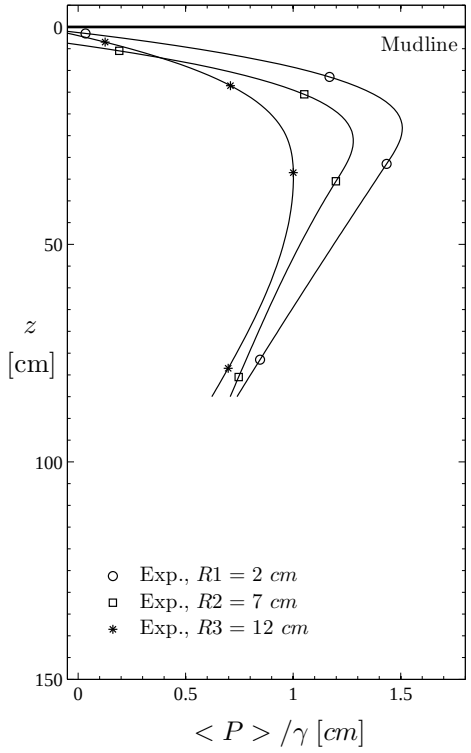

Figure 4.15: *Vertical PWP amplitude distribution, Experiment.*

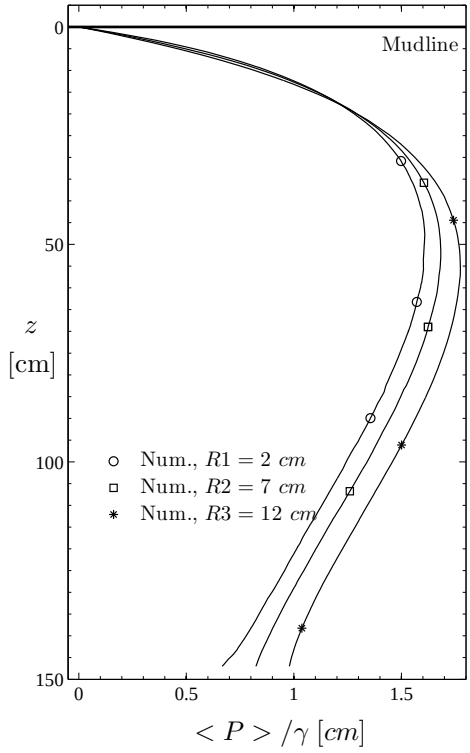

Figure 4.16: *Vertical PWP amplitude distribution, Numerical model.*

4.2.6 Discussion of Mesh Size

Finally a simple validation exercise, where the effect of the number of soil elements was carried out. This validation exercise was however, only performed for the full-scale model. Two full-scale models were used. Here called *model A* and *model B*. Both models having identical soil properties and geometrical dimensions. A 35.3 m long pile placed in 25 m of soil depth, cyclic loaded with an amplitude $x_D = 0.07$ m and a period $T = 10$ s (See Sec. 5.4 for further description).

The soil domain in model A consisted of 9137 tetrahedral elements, while model B consisted of 27598 tetrahedral elements, thus the soil domain was a factor of 3 more refined in model A. In model A, the minimum mesh size

in the vicinity of the pile was 0.99 m, while for model B the minimum mesh size was 0.69 m. To compare the models, the normal effective stress in the x-direction and the PWP were extracted at $r = 0.5$ m, $\theta = 0°$ and $z = 5$ m.

Fig. 4.17 depicts the results obtained from the comparison exercise. From the figure it can be noticed, that 1) the PWP coincides well, while 2) the normal effective stress σ'_x deviates slightly more. The difference between the two models was 7.1 % for the effective stress, while a difference of 2.9 % in the PWP was observed.

For the full-scale simulations, model A was chosen since it was considered to give sufficient accuracy in the numerical computations. It should be noticed, that the number of degrees of freedom was DOF = 403267 for model B while model A only had DOF = 297035.

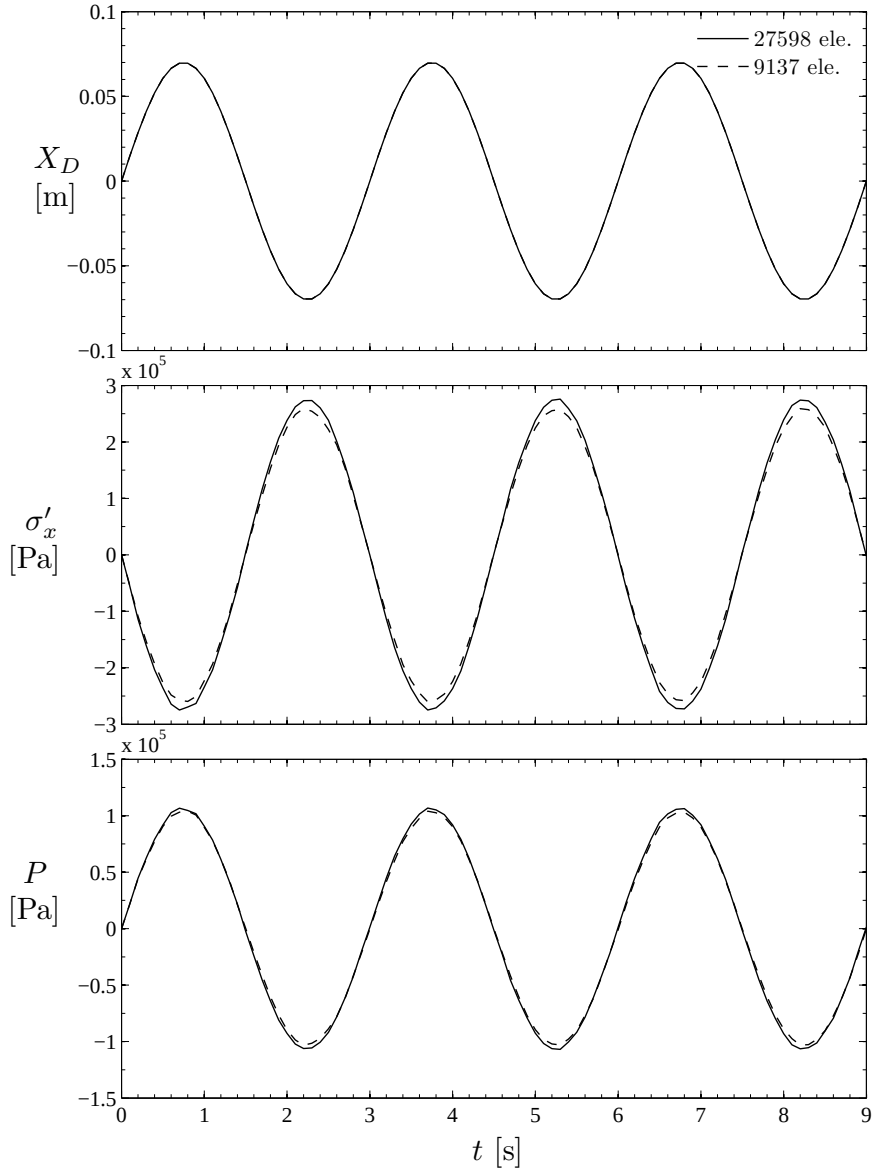

Figure 4.17: *Comparison of the effective normal stress σ'_x and the PWP in model A and model B.*

This page is intentionally left blank.

Chapter 5

Numerical Model for Full-Scale Conditions

5.1 Introduction

This chapter will present the numerical findings when simulating field conditions for an OWT pile foundation. A key finding is the soil response to the pile motion in terms of the familiar soil resistance curves, more commonly known as p-y curves.

Although p-y curves are a widespread concept within OWT pile foundations, or lateral loaded piles in general, a short description of the concept and use of the p-y curves will be given herein.

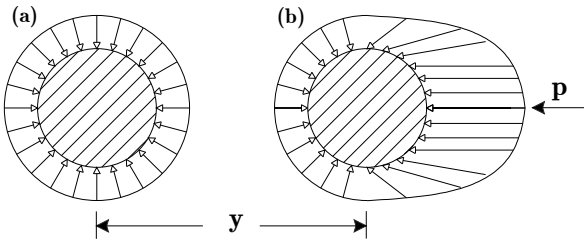

Figure 5.1: *Distribution of stress on the pile wall where the stress vectors correspond to the resultant forces per unit area, (a) before and (b) after lateral deflection, from Reese and Impe (2001).*

The concept of the p-y curves is presented with reference to Fig. 5.1 and Fig. 5.2. Consider a pile driven through the soil (assuming no deflections of the pile to occur when installing the pile). See Fig. 5.1.a where a thin slice of the plan view of the pile is shown. The distribution of the stress vectors (which are uniformly distributed before deflection occurs) corresponds to the resultant forces per unit area, made up of both the normal component and the tangential component, not to be confused with the familiar pressure distribu-

tion in hydrodynamics. When displacing the pile a distance y, a nonuniform stress distribution will be as sketched in Fig. 5.1.b. The resultant of the integration of the forces will be a stress p (force per unit length) acting opposite the direction of the displacement y. The relation between the resultant stress p and the displacement y, forms the soil resistance curve (p-y curve). Note, here y is used to denote the lateral displacement as function of depth. Fig. 5.2 shows a typical p-y curve. The quantities p and E_{py} is properly termed the *soil resistance* and *reaction modulus for a pile under lateral loading* respectively (Reese and Impe, 2001, pg. 4). The reaction modulus represent the stiffness of the pile foundation. In the present study, only the linear part the p-y curve is considered.

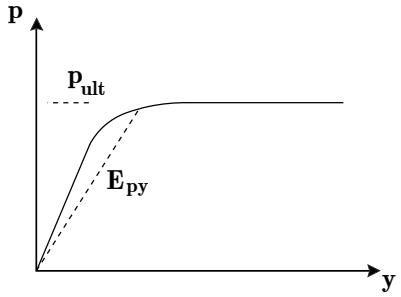

Figure 5.2: *Typical p-y curve, after Reese and Impe (2001).*

The current design recommendations have adopted the p-y method. The method of computing a set of p-y curves is here shortly presented according to DNV (2004). The static ultimate lateral soil resistance p_{ult} is given as,

$$p_{ult} = \begin{cases} (C_1 z + C_2 D)\gamma' z & \text{for } 0 < z \leq z_R \\ C_3 \gamma' z & \text{for } z > z_R \end{cases} \tag{5.1}$$

where D is the pile diameter, γ' is the submerged specific weight of the soil, z is the distance below the soil surface and z_R is a transition depth, below which the value of $(C_1 z + C_2 D)\gamma' z$ exceeds $C_3 D \gamma' z$. The constants C_1, C_2 and C_3 depends on the friction angle. For a dense soil, these may be taken as $C_1 = 4.5$, $C_2 = 4.2$ and $C_3 = 100$. The p-y curve can be computed from,

$$p = A p_{ult} \tanh\left(\frac{k_T z}{A p_{ult}} y\right) \tag{5.2}$$

where $A = 0.9$ to account for cyclic loading, y is the lateral displacement of the pile and k_T is the initial modulus of subgrade reaction and depends on the relative density and the friction angle. For a dense soil below the water table, $k_T = 40$ MPa/m. Fig. 5.3 depicts a set of p-y curves for a 5 m diameter pile in a dense sand.
It may be noticed that the soil reaction modulus increases as depth increases.

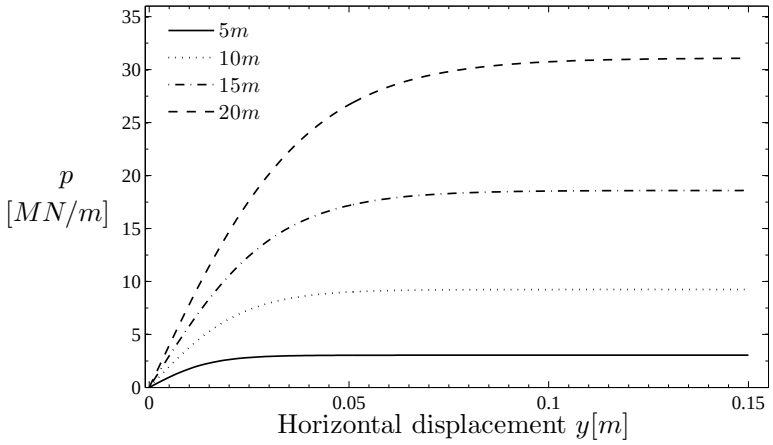

Figure 5.3: *P-y curves based on the DNV-OS-J101. Dense sand below the water table,* $k = 40$ MPa/m*, pile diameter* $D = 5$ m*, submerged unit weight of the soil* $\gamma' = 15.6$ kN/m^3 *and* $C_1 = 4.5$*,* $C_2 = 4.2$ *and* $C_3 = 100$*.*

For the analysis of the lateral loaded pile, the set of p-y curves can be implemented in a FEM-model and the pile response can be calculated by solving the fourth-order differential equation for a beam,

$$E_p I_p \frac{d^4 y}{dz^4} - p(y) = 0, \quad \text{where } z \in [0; e_d] \tag{5.3}$$

where E_p is the pile Young modulus, I_p is the pile area moment of inertia and e_d is the foundation depth.

5.2 Non-Dimensional Quantities

The soil resistance p (force per meter) along the length of the monopile may by a function of the following set of dimensional parameters,

$$p = F(y,\ x_D,\ \nu,\ G,\ S_r,\ K_w,\ e_d,\ e_x,\ n,\ k,\ D,\ T,\ \rho',\ E_p I_p,\ \nu_p,\ g,\ Q) \tag{5.4}$$

where x_D is the amplitude of the rocking motion, ν is the Poisson's ratio of the soil, G is the soil shear modulus, S_r is the saturation degree, K_w is the true bulk modulus of water, e_d is the foundation depth, e_x is the load eccentricity, n is the soil porosity, k is the the soil permeability, T is the period of the rocking motion, ρ' is the submerged density of the soil (in the case of dry conditions, $\rho'(= \rho_t - \rho)$, should be replaced by ρ_t), $E_p I_p$ is the pile bending stiffness, ν_p is the pile Possion's ratio, g is the acceleration of gravity and Q being the lateral force exerted on the pile from waves. From dimensional analysis, the soil resistance p, may be expressed by the following non-dimensional groups,

$$\frac{p}{\frac{1}{2}\rho' D(Dg)} = f(\frac{y}{D}, \frac{x_D}{D}, \nu, S, S_r, \frac{e_d}{D}, \frac{e_x}{D}, n, \nu_p, s) \tag{5.5}$$

First considering the left hand side of Eq. (5.5). The soil resistance may be viewed as a resistance force felt by the pile. Although the resistance force in the case of a rocking pile, may emerge from processes significantly different compared to a body in steady fluid motion, the resistance force may be written as,

$$p = \frac{1}{2}\rho' C_p D(Dg) \tag{5.6}$$

where C_p represents a "resistance" coefficient. Clearly the product (Dg) represents a velocity squared as in the case of steady fluid motion. The above formulation is analogous to that of forces on a cylinder subject to current in fluid mechanics (Sumer and Fredsøe, 2006, pg. 43). Hence the soil resistance p may simply be viewed as a drag force, which on non-dimensional form can be expressed as,

$$C_p = \frac{p}{\frac{1}{2}\rho' D(Dg)} \tag{5.7}$$

The quantity C_p is analogous to the drag coefficient associated with the drag force on a cylinder in fluid motion. Now considering the non-dimensional parameter S. This parameter is written as,

$$S = \frac{(Gk/\gamma)T}{D^2} \tag{5.8}$$

where γ is the specific weight of water. Eq. 5.8 is similar to the expression given in Sumer (2013), namely $S = (Gk/\gamma)T/L^2$. Following the same ideas as in Sumer (2013), the parameter S may be derived in the following way. From the Biot equations, one can obtain the equation governing the diffusion of PWP (diffusion equation), namely (Sumer and Fredsøe, 2002, pg. 470),

$$\frac{\partial P}{\partial t} = c_v \frac{\partial^2 P}{\partial z^2} + f \tag{5.9}$$

where f is a source term representing the amount of PWP generated. c_v is the coefficient of consolidation given as,

$$c_v = \frac{Gk}{\gamma} \frac{2 - 2\nu}{(1 - 2\nu) + (2 - 2\nu)\frac{nG}{K'}} \tag{5.10}$$

It should be noticed that only a 2D process in considered in the preceding two equations. In the case of a saturated soil $G/K' \to 0$. In addition, ν may vary in the range of $0.1 - 0.2$ in the initial stage of loading and $0.3 - 0.4$ during cyclic loading, (Lambe and Whitman, 1969, pg. 160). Therefore, as a first approximation, the coefficient of consolidation c_v can be simplified as,

$$c_v = \frac{Gk}{\gamma} \tag{5.11}$$

Now, from the theory of diffusion and dispersion, a measure of spreading in terms of a length scale ℓ, may by given as $\ell^2 = 2D_c t$, where D_c is a diffusion coefficient and t is time (Sumer, 2007). Considering a period T and substituting the diffusion coefficient D_c with the coefficient of consolidation c_v, a measure of the distance, the pore-water pressure spreads over one period may be given as $\ell^2 = (Gk/\gamma)T$. The pile diameter D is on the other hand a characteristic length scale of the problem. Therefore the parameter S may be interpreted as the degree of spreading of PWP during one period. Large values of S implies that the PWP is spread over a wider distance, thus the magnitude of PWP is "small", while small values of S implies the magnitude of PWP to be "larger" (a similar expression is given in Bhattacharya *et al.* (2011), namely $k/((1/T)D)$ which express the PWP generation and dissipation in terms of length scales).

Finally consider the non-dimensional group $Qe_xD/(E_pI_p)$. Bhattacharya *et al.* (2011) formulated the bending strain ϵ_p in a monopile under lateral load as being a function of the following non-dimensional group,

$$\epsilon_p = f\left(\frac{Qe_x}{E_pD^2t_w}\right) \tag{5.12}$$

where t_w is the wall thickness of the monopile. Adopting Eq. 5.12 a non-dimensional parameter s can be formulated,

$$s = \frac{Qe_xD}{E_pI_p} \tag{5.13}$$

where s may be termed a strain parameter. See appendix F for the derivation of Eq. 5.13.

5.3 Model Geometry and Boundary Conditions

The model geometry is shown in Fig. 5.4. Note, that only half of the computation domain is shown as well as the pile dimension is grossly exaggerated for illustration purpose. The soil domain is divided into small segments surrounding the main soil domain. The small segments are used as infinite domains as described in Sec. 2.3.2. The boundary conditions may be described with reference to Fig. 5.5 showing a cross-section view of the 3D-model. The inner segments of the soil domain is used to dissipate the PWP. A zero flux boundary condition for the PWP is used. Another feasible, maybe more correct boundary condition would be a Dirichlet-type boundary condition imposing zero pressure at the wall. However the choice of boundary is of less significance when using infinite elements. The outer segments are used to "dissipate" the soil displacements. At infinite soil extension, the soil displacements should be zero. The pile is loaded by a constant pile head deflection X_D according to Eq. 2.19. The pile/soil interface is defined as a no-slip boundary as described in Sec. 2.3.6.

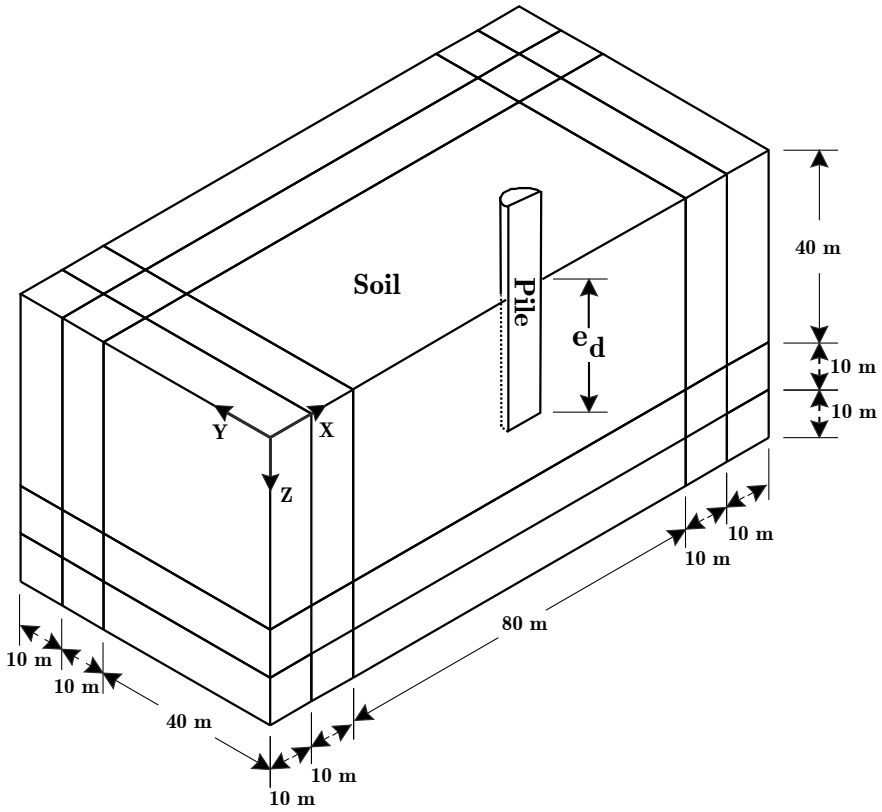

Figure 5.4: *Full-Scale model, definition sketch. Pile dimensions are exaggerated for visualization purpose.*

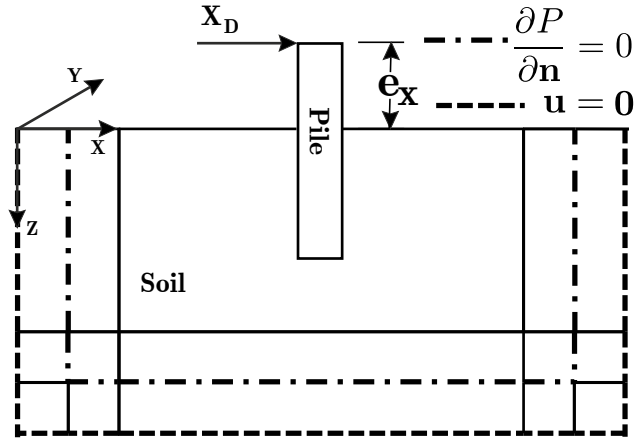

Figure 5.5: *Side-view of the numerical model.*

5.4 Test Conditions and Input Parameters

To simulate field conditions, a 5 m diameter solid steel pile was used in the numerical field simulations. The peak displacement of the pile head was $x_D = 7$ cm. The soil was modelled as an unsaturated dense soil ($S_r = 0.99$). The variation of Young's modulus with depth was expressed accordantly to Eq. 3.5, where the values of $E_{ref} = 177$ MPa, $\sigma'_{3,ref} = 150$ kPa and $\alpha = 0.62$ were adopted from (Eskesen *et al.*, 2010) corresponding to a medium sand. Tab. 5.1 presents the parameters kept constant during all simulations.

Parameter	Symbol	Unit	Value
Pile diameter	D	$[m]$	5.0
Peak displacement	x_D	$[m]$	0.07
Poisson's ratio (Pile)	ν_p	$[-]$	0.33
Density (Pile)	ρ_p	$[kg/m^3]$	7850
Relative density	D_r	$[-]$	0.90
Porosity	n	$[-]$	0.38
Degree of saturation	S_r	$[-]$	0.99
Young's modulus (Soil)	E	$[Pa]$	see text
Poisson's ratio (Soil)	ν	$[-]$	0.20
Density (Soil)	ρ	$[kg/m^3]$	1586
Bulk modulus (Water)	K_w	$[Pa]$	$2.3 \cdot 10^9$
Acceleration of gravity	g	$[m/s^2]$	9.81

Table 5.1: *Constant input parameters for full-scale simulations.*

To determine the load eccentricity, the model pile was assumed to be placed in a water depth $d = 15$ m. Waves with a wave height $H = 8$ m and a period $T = 10$ s was used to calculate the load eccentricity e_x on the pile based on small amplitude linear waves and the Morison Equation (Sumer and Fredsøe, 2006, pg. 130).

The parametric study consisted of 36 studies. An overview of the parametric study is presented in Tab. 5.2. The parametric study was divided into two groups. In the first group, the pile was modelled as a solid pile. In the second group, the pile was modelled as a hollow pile, simulation a 5 m OWT pile foundation with a wall thickness of 5 cm. In those tests, where the rocking period $T = 3$ s, the simulated real-time was 9 s, whereas for the tests of $T = 10$ s, the simulated real-time was 20 s.

	Dimensional parameters					Nondimensional parameters			
Test	T	e_d	e_x	k	E_p	e_d/D	e_x/D	S	s
[#]	$[s]$	$[m]$	$[m]$	$[cm/s]$	$[GPa]$	–	–	–	–
1	10	25	10.3	0.1	210	5	2.1	3.3	$3.8 \cdot 10^{-5}$
2	3	25	10.3	0.1	210	5	2.1	1.0	$3.8 \cdot 10^{-5}$
3	10	25	10.3	0.01	210	5	2.1	0.33	$3.8 \cdot 10^{-5}$
4	3	25	10.3	0.01	210	5	2.1	0.10	$3.8 \cdot 10^{-5}$
5	10	25	10.3	0.0001	210	5	2.1	0.003	$3.8 \cdot 10^{-5}$
6	3	25	10.3	0.0001	210	5	2.1	0.001	$3.8 \cdot 10^{-5}$
7	10	15	10.3	0.1	210	3	2.1	3.3	$3.8 \cdot 10^{-5}$
8	3	15	10.3	0.1	210	3	2.1	1.0	$3.8 \cdot 10^{-5}$
9	10	15	10.3	0.01	210	3	2.1	0.33	$3.8 \cdot 10^{-5}$
10	3	15	10.3	0.01	210	3	2.1	0.10	$3.8 \cdot 10^{-5}$
11	10	15	10.3	0.0001	210	3	2.1	0.003	$3.8 \cdot 10^{-5}$
12	3	15	10.3	0.0001	210	3	2.1	0.001	$3.8 \cdot 10^{-5}$
13	10	35	10.3	0.1	210	7	2.1	3.3	$3.8 \cdot 10^{-5}$
14	3	35	10.3	0.1	210	7	2.1	1.0	$3.8 \cdot 10^{-5}$
15	10	35	10.3	0.01	210	7	2.1	0.33	$3.8 \cdot 10^{-5}$
16	3	35	10.3	0.01	210	7	2.1	0.10	$3.8 \cdot 10^{-5}$
17	10	35	10.3	0.0001	210	7	2.1	0.003	$3.8 \cdot 10^{-5}$
18	3	35	10.3	0.0001	210	7	2.1	0.001	$3.8 \cdot 10^{-5}$
19	10	25	10.3	0.1	16	5	2.1	3.3	$5.0 \cdot 10^{-4}$
20	3	25	10.3	0.1	16	5	2.1	1.0	$5.0 \cdot 10^{-4}$
21	10	25	10.3	0.01	16	5	2.1	0.33	$5.0 \cdot 10^{-4}$
22	3	25	10.3	0.01	16	5	2.1	0.10	$5.0 \cdot 10^{-4}$
23	10	25	10.3	0.0001	16	5	2.1	0.003	$5.0 \cdot 10^{-4}$
24	3	25	10.3	0.0001	16	5	2.1	0.001	$5.0 \cdot 10^{-4}$
25	10	15	10.3	0.1	16	3	2.1	3.3	$5.0 \cdot 10^{-4}$
26	3	15	10.3	0.1	16	3	2.1	1.0	$5.0 \cdot 10^{-4}$
27	10	15	10.3	0.01	16	3	2.1	0.33	$5.0 \cdot 10^{-4}$
28	3	15	10.3	0.01	16	3	2.1	0.10	$5.0 \cdot 10^{-4}$
29	10	15	10.3	0.0001	16	3	2.1	0.003	$5.0 \cdot 10^{-4}$
30	3	15	10.3	0.0001	16	3	2.1	0.001	$5.0 \cdot 10^{-4}$
31	10	35	10.3	0.1	16	7	2.1	3.3	$5.0 \cdot 10^{-4}$
32	3	35	10.3	0.1	16	7	2.1	1.0	$5.0 \cdot 10^{-4}$
33	10	35	10.3	0.01	16	7	2.1	0.33	$5.0 \cdot 10^{-4}$
34	3	35	10.3	0.01	16	7	2.1	0.10	$5.0 \cdot 10^{-4}$
35	10	35	10.3	0.0001	16	7	2.1	0.003	$5.0 \cdot 10^{-4}$
36	3	35	10.3	0.0001	16	7	2.1	0.001	$5.0 \cdot 10^{-4}$

Table 5.2: *Parameters used for parametric study. The quantities S and s is defined in Eq. 5.8 and Eq. 5.13, respectively.*

5.5 Computational Mesh

The build-in mesh generator in COMSOL is used to generate the computational mesh (Fig. 5.6). The complete computational mesh is divided into 76 domains. The pile consists of one domain, and the soil consist of a second domain. The remaining 74 domains are used to simulate the infinite domains. Tab. 5.3 present an overview of the mesh elements used in the computational domain (test $1-6$ and test $19-24$).

Domain	Element type	No. of elements	Avg. qual.	Min. qual.
Soil	Tetrahedral	9295	0.76	0.28
Pile	Prism	8100	0.83	0.64
Infi.	Tetrahedral	360	0.23	0.12
	Pyramid	900	0.50	0.19
	Hexahedral	3492	0.62	0.13
Total		22147		

Table 5.3: *Mesh overview of computational domain, test* $1-6$ *and test* $19-24$.

In order to obtain robust and faster convergence the minimum mesh quality should be larger then 0.1. This requirement is fulfilled for the computational mesh used. For the tests $7-12, 25-30$ and $13-18, 30-36$ the number of elements were 20022 and 23774 respectively.

Fig. 5.7 shows a detail of the mesh near the pile. The computational mesh has been stresses from the center of the domain, thus the mesh density is largest around the pile.

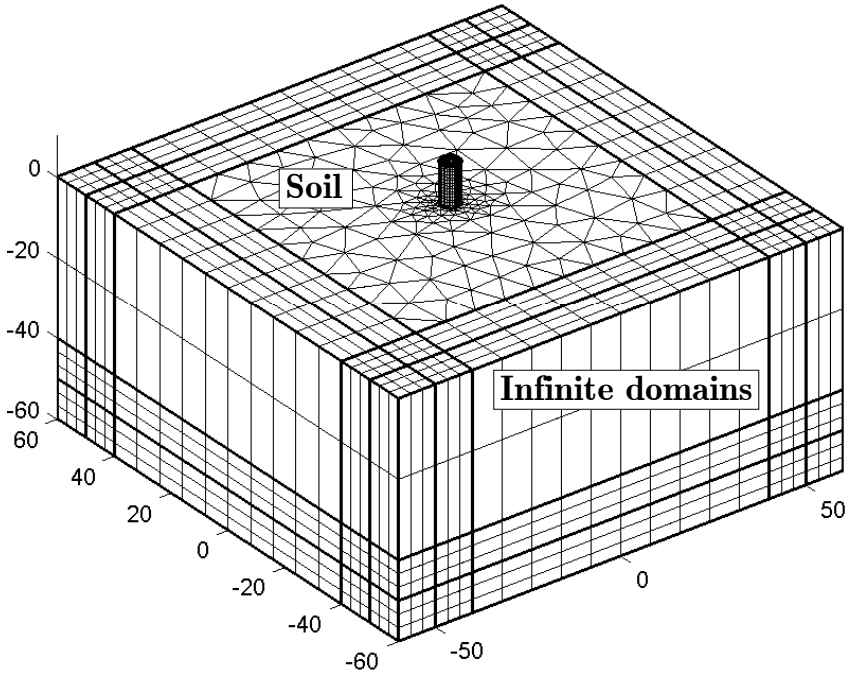

Figure 5.6: *Example of computational mesh used for rocking pile simulations. The complete mesh consist of* 22147 *elements.*

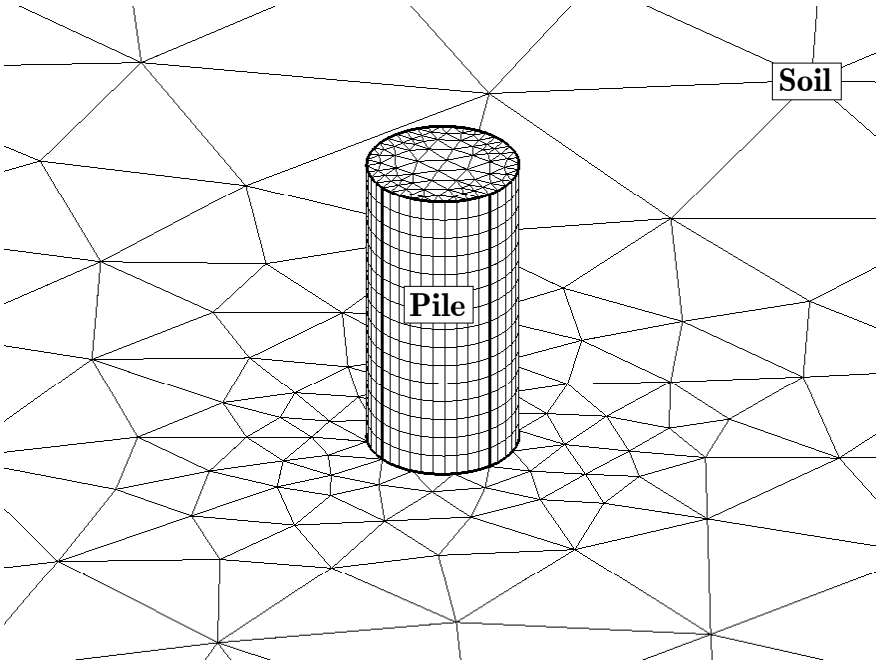

Figure 5.7: *Detail of computational mesh around the pile.*

5.6 Pile Bending

When dealing with lateral loaded piles, generally the lateral pile response is distinguished into two categories, namely flexible pile behavior or rigid pile behavior. In rigid pile behavior a "toe kick" occurs. Various studies have formulated stiffness criteria for lateral loaded piles in cohesionless soils, e.g. (Budhu and Davies, 1987), (Dobry *et al.*, 1982) and (Poulos and Hull, 1989). Here the flexibility criterion formulated by Poulos and Hull (1989) is adopted,

$$L_c = 4.44 \left(\frac{E_p I_p}{E} \right)^{0.25} \tag{5.14}$$

where L_c is the critical length of the pile. If $L < L_c/3$ the pile is a rigid pile, whereas if $L > L_c$ the pile is a flexible pile. In between, the pile is defined as an intermediate pile. By adopting Eq. 5.14 the lateral pile behavior in the numerical model can be summarized as in Tab. 5.4.

Test	Type	Length $[m]$	Behavior
$1-6$	Solid	25	Intermediate
$7-12$	Solid	15	Rigid
$13-18$	Solid	35	Intermediate
$19-24$	Hollow	25	Intermediate
$25-30$	Hollow	15	Intermediate
$31-36$	Hollow	35	Flexible

Table 5.4: *Pile behavior category.*

The lateral pile response in terms of pile bending is presented in Fig. 5.8 and Fig. 5.9. In the solid pile tests, it can be seen, that toe-kick occurs. It is clearly noticed, that the 15 m solid pile (Fig. 5.8 left) has a minimum flexure which is consistent with the rigid pile behavior expected according to the flexibility criterion. It may also be noticed that no toe kick occurs for the hollow 35 m pile which again is consistent with the flexibility criterion. For the remaining set of the tests, the pile behaves as an intermediate pile, where both toe-kick and large flexural behavior occurs.

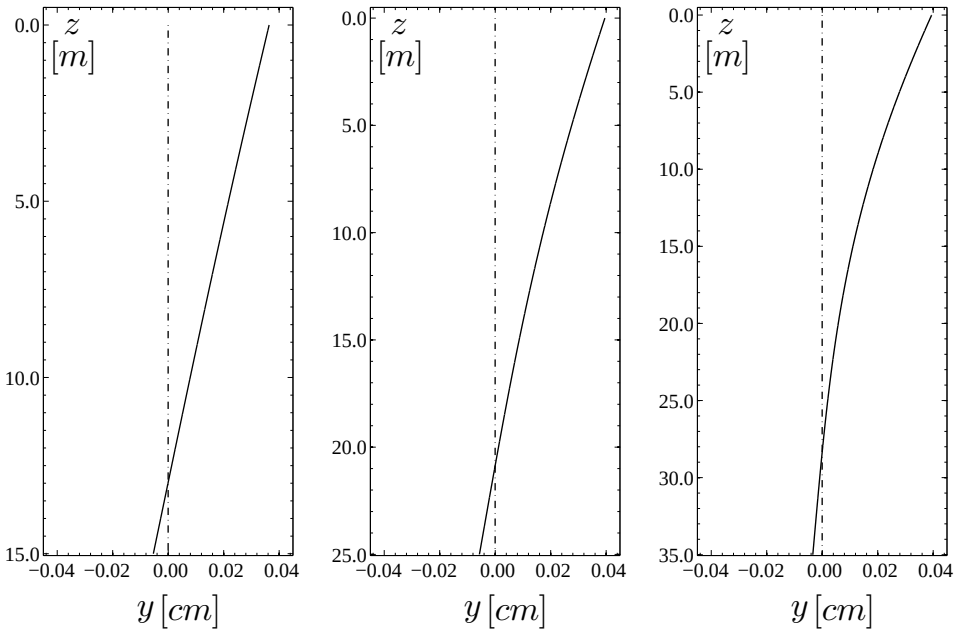

Figure 5.8: *Pile bending for group* 1 *(Solid pile). Left: foundation depth* $e_d = 15$ m, *middle: foundation depth* $e_d = 25$ m *and right: foundation depth* $e_d = 35$ m.

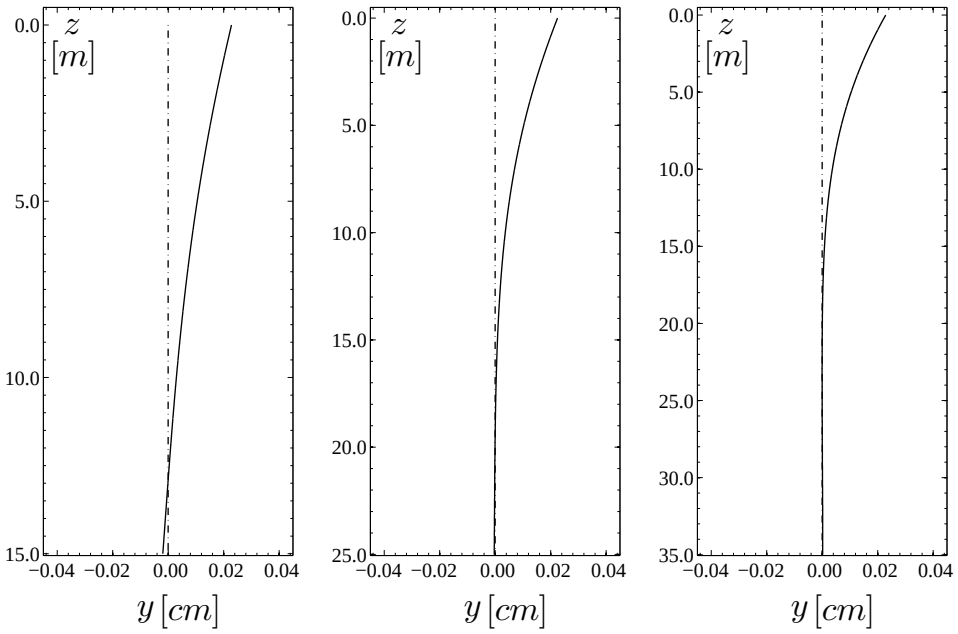

Figure 5.9: *Pile bending for group* 2 *(Hollow pile). Left: foundation depth* $e_d = 15$ m, *middle: foundation depth* $e_d = 25$ m *and right: foundation depth* $e_d = 35$ m.

5.7 Soil Resistance Distribution and Non-Dimensional p-y curves

As described in Sec. 2.5.3, the pile/soil interface is modelled using *weak constraints*, which means that a Lagrange multiplier λ_L is introduced at the pile/soil interface. The Lagrange multiplier can be interpreted as a reaction force when working in solid mechanics. The reaction force is equivalent to the soil resistance. The soil resistance force p (force per unit length) can therefore be obtained by integrating the Lagrange multiplier around the pile,

$$p = \int_0^{2\pi} \lambda_L (r_0 d\theta) \tag{5.15}$$

where r_0 is the pile radius and θ is the angle defined in Fig. 1.2. The pile displacement y along the length of the pile is directly extracted from the numerical model. Fig. 5.10 and Fig. 5.11 show the soil resistance distributions along the pile length.

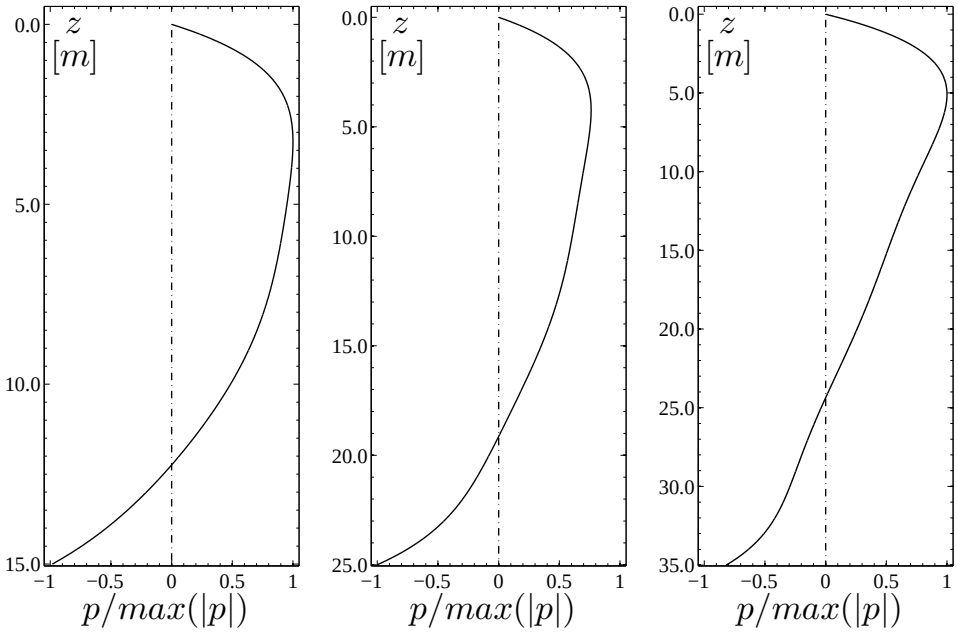

Figure 5.10: *Soil resistance distribution for group* 1 *(Solid pile* $s = 3.8 \cdot 10^{-5}$, $S = 0.33$*). Left: foundation depth* $e_d = 15$ m, *middle: foundation depth* $e_d = 25$ m *and right: foundation depth* $e_d = 35$ m.

As seen, there is roughly two different shapes of soil resistance curves. Common for both, the soil resistance tends towards zero at the mudline as expected, since the soil strength at the mudline is assumed zero. For the rigid piles (Fig. 5.10) the soil resistance reaches its maximum within the first 5 m of soil depth. Then the soil resistance decrease. This is clearly related

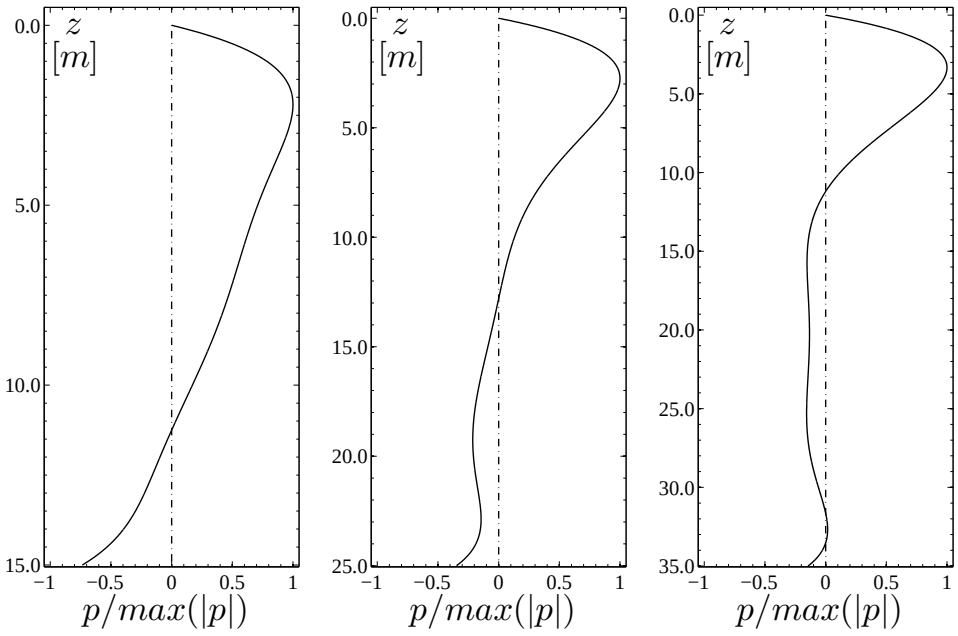

Figure 5.11: *Soil resistance distribution for group* 2 *(Hollow pile* $s = 5.0 \cdot 10^{-4}$*,* $S = 0.33$*). Left: foundation depth* $e_d = 15$ m*, middle: foundation depth* $e_d = 25$ m *and right: foundation depth* $e_d = 35$ m*.*

to the decrease in deflection y as moving towards the pile toe. As "toe kick" occurs, the soil resistance starts acting in the opposite direction. A qualitative comparison of the soil resistance curves for the rigid piles obtained in the present study and the study of Zania and Hededal (2011).Fig.9 can be done. A similar shape is observed. For the flexible piles, the soil resistance tends towards zero at the pile toe. This is clearly related to the zero deflection at the pile toe for the flexible pile.

Fig. 5.12 and Fig. 5.13 show the p-y curves obtained from test 1-6 ($e_d/D = 5$) at the depth $z/D = 1$ and $z/D = 2$ respectively. Also plotted are the soil response predictions obtained accordantly to the design recommendations (DNV, 2004).

The following two observations are noticed; 1) The reaction modulus obtained in the numerical model by calculating,

$$E_{py,num} = \left(\frac{dC_p}{dy}\right)_{At\ y/D=0.01} \tag{5.16}$$

is comparable to the design recommendations. This will be discussed in Sec. 5.8. 2) The change in reaction modulus $E_{py,num}$ in general is consistent with the change of the non-dimensional spreading parameter S. As described in Sec. 5.2 the spreading parameters governs the magnitude of PWP. When the

spreading parameter S is large, the magnitude of PWP is small compared to small spreading parameters. Recalling the relation between PWP and effective stresses in a soil, namely $\sigma = \sigma' + P$, it is clear that when the PWP increases, the effective stress decreases which leads to a "softer" soil response. To underline this, consider the extreme case, where liquefaction occurs. Here the effective stresses are null, thus the soil having no stiffness. Fig. 5.14 and Fig. 5.15 show the p-y curves for test 7-12 ($e_d/D = 3$) while Fig. 5.16 and Fig. 5.17 show the p-y curves for test 15-18 ($e_d/D = 7$). It is clear that the results are consistent with respect to the spreading parameter S.

For the flexible pile case (Fig. 5.18, Fig. 5.19, Fig. 5.20, Fig. 5.21, Fig. 5.22 and Fig. 5.23), a relation between the spreading parameter S and the reaction modulus $E_{py,num}$ is also seen. However the results are inconsistent with the spreading parameter for depth $z/D = 2$. This will be discussed in Sec. 5.8.

Fig. 5.24 depicts the soil resistance C_p as function of the non-dimensional foundation depth at level $z/D = 1$. Here the influence of the non-dimension foundation can be seen. As the foundation length increase, the soil resistance is distributed over a wider span of the pile foundations, thus the resistance decrease.

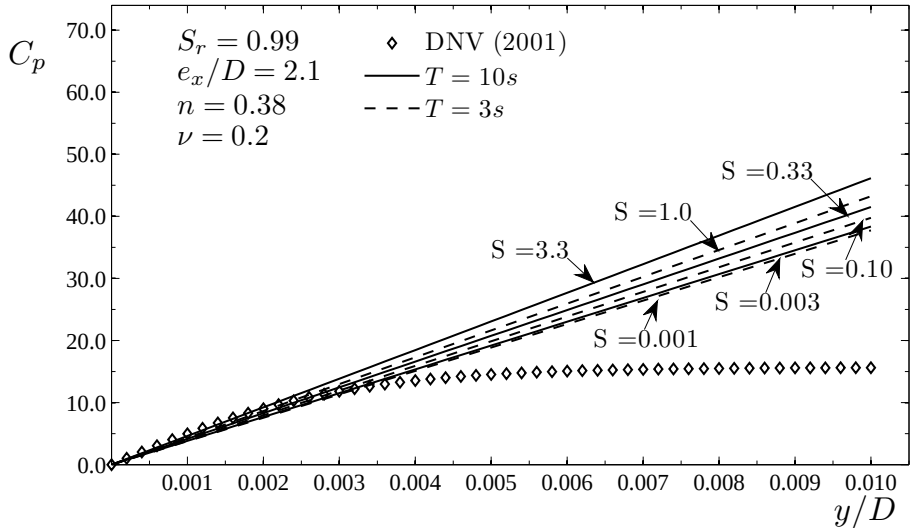

Figure 5.12: *Non-dimensional p-y curves at the depth $z/D = 1$. Rigid pile simulations, foundation depth $e_d/D = 5$, $s = 3.8 \cdot 10^{-5}$, test 1-6.*

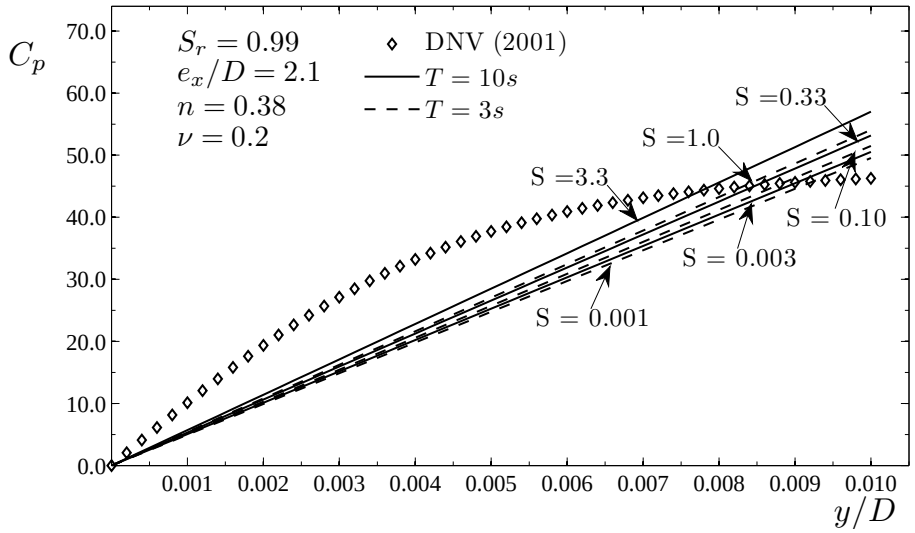

Figure 5.13: *Non-dimensional p-y curves at the depth $z/D = 2$. Rigid pile simulations, foundation depth $e_d/D = 5$, $s = 3.8 \cdot 10^{-5}$, test 1-6.*

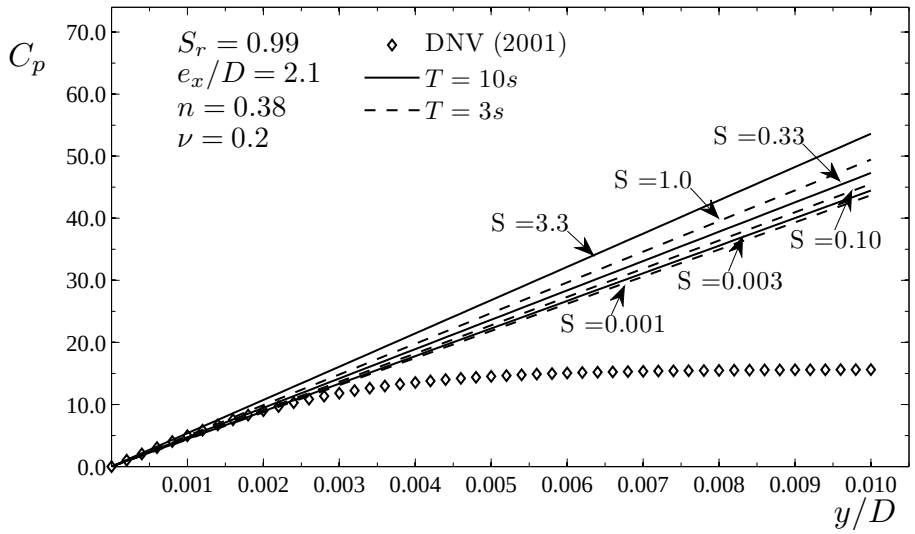

Figure 5.14: *Non-dimensional p-y curves at the depth $z/D = 1$. Rigid pile simulations, foundation depth $e_d/D = 3$, $s = 3.8 \cdot 10^{-5}$, test 7-12.*

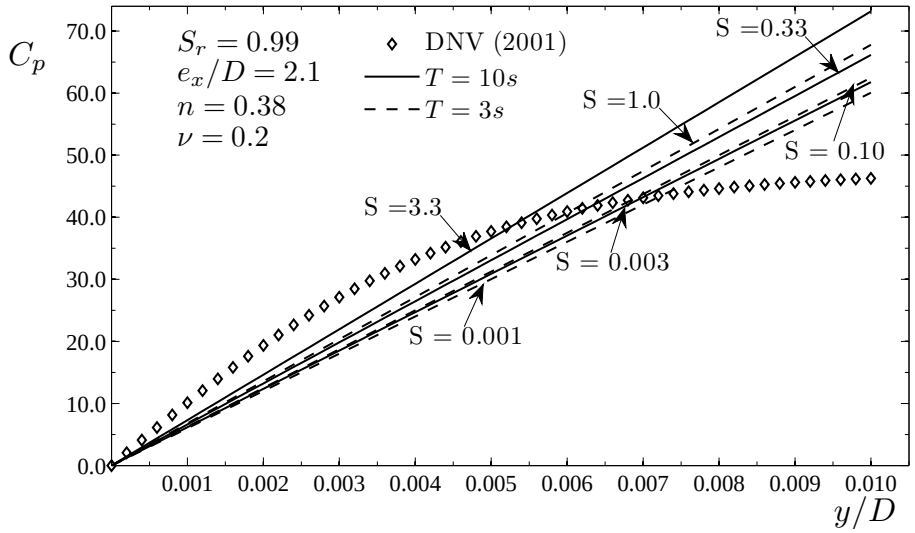

Figure 5.15: *Non-dimensional p-y curves at the depth $z/D = 2$. Rigid pile simulations, foundation depth $e_d/D = 3$, $s = 3.8 \cdot 10^{-5}$, test 7-12.*

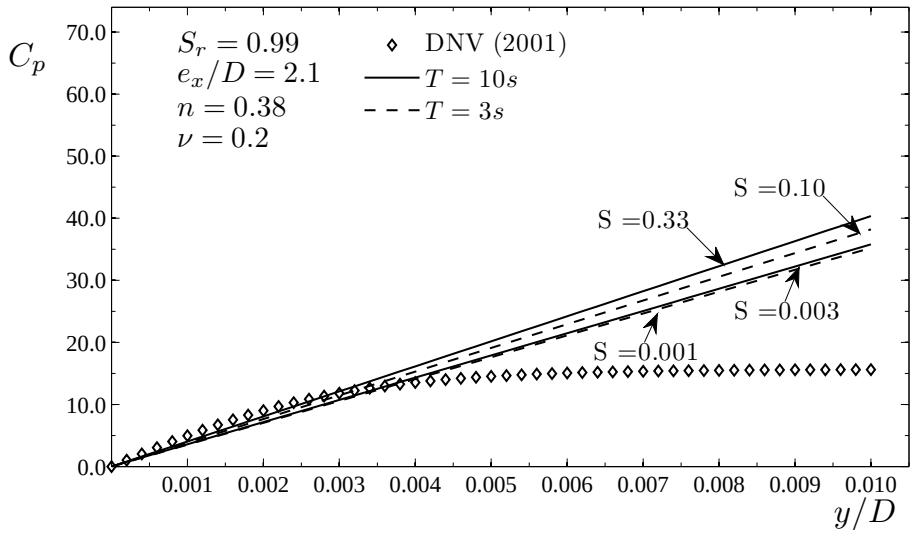

Figure 5.16: *Non-dimensional p-y curves at the depth $z/D = 1$. Rigid pile simulations, foundation depth $e_d/D = 7$, $s = 3.8 \cdot 10^{-5}$, test 15-18.*

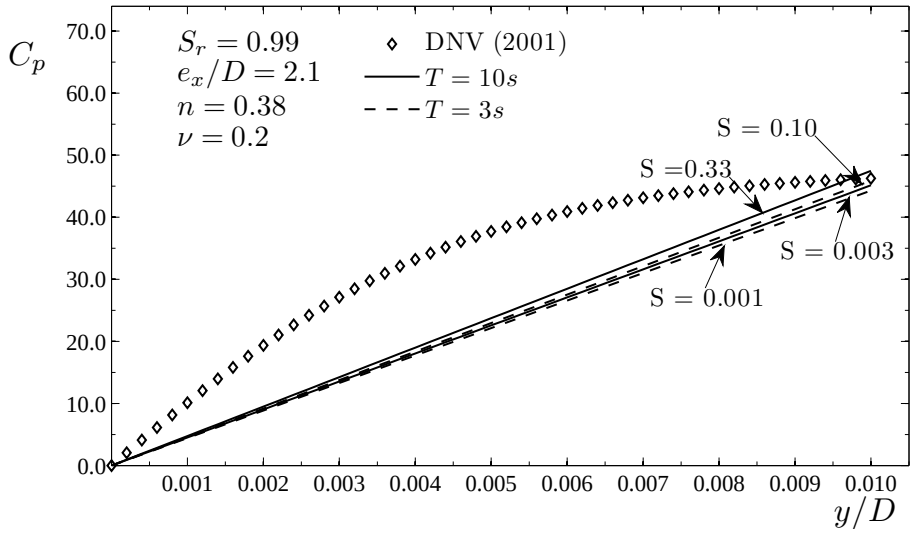

Figure 5.17: *Non-dimensional p-y curves at the depth $z/D = 2$. Rigid pile simulations, foundation depth $e_d/D = 7$, $s = 3.8 \cdot 10^{-5}$, test 15-18.*

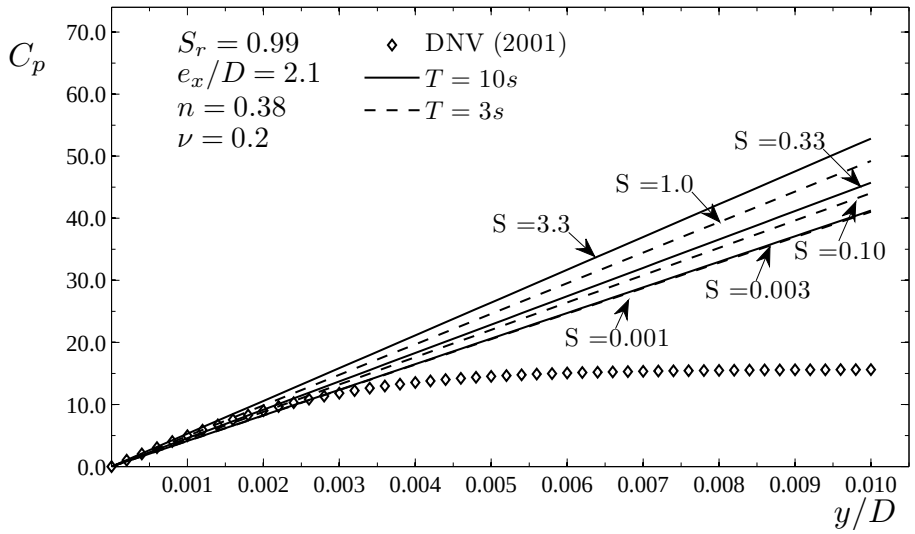

Figure 5.18: *Non-dimensional p-y curves at the depth $z/D = 1$. Flexible pile simulations, foundation depth $e_d/D = 5$, $s = 5.0 \cdot 10^{-4}$, test 19-24.*

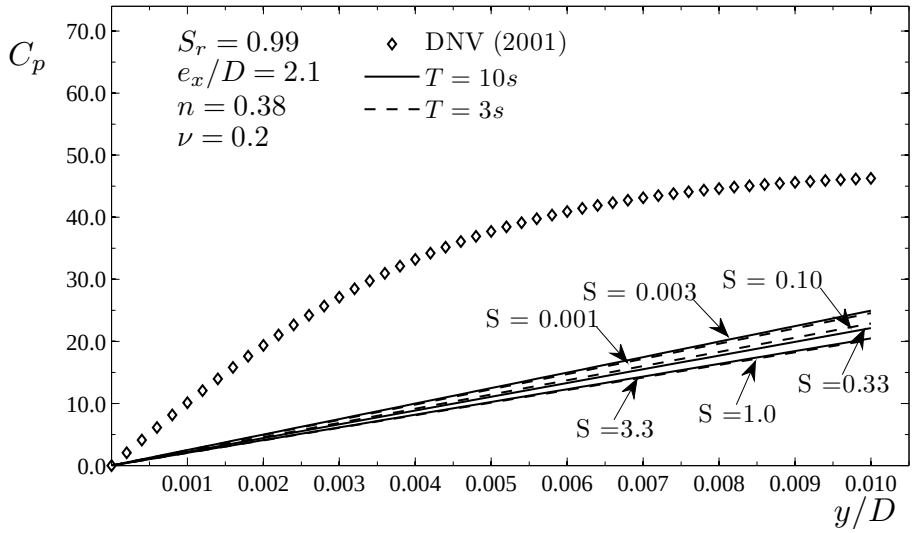

Figure 5.19: *Non-dimensional p-y curves at the depth $z/D = 2$. Flexible pile simulations, foundation depth $e_d/D = 5$, $s = 5.0 \cdot 10^{-4}$, test 19-24.*

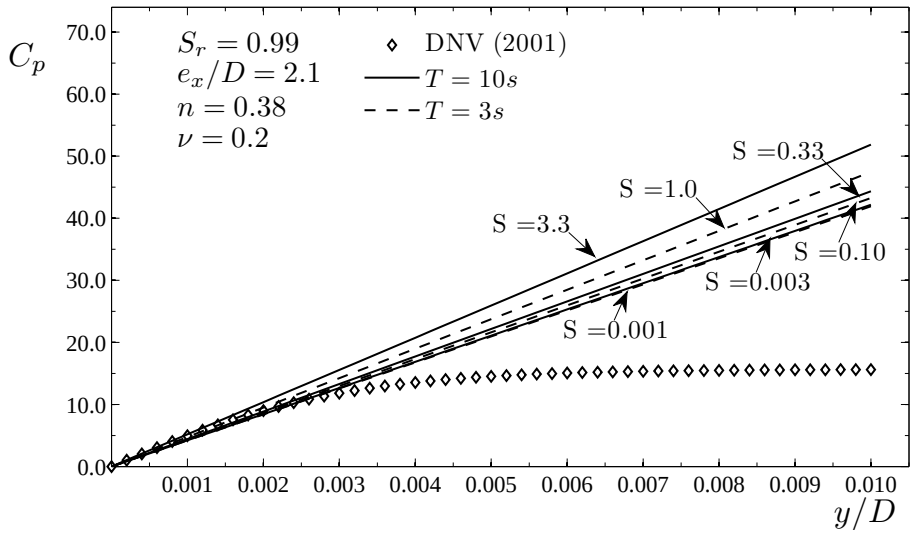

Figure 5.20: *Non-dimensional p-y curves at the depth $z/D = 1$. Flexible pile simulations, foundation depth $e_d/D = 3$, $s = 5.0 \cdot 10^{-4}$, test 25-30.*

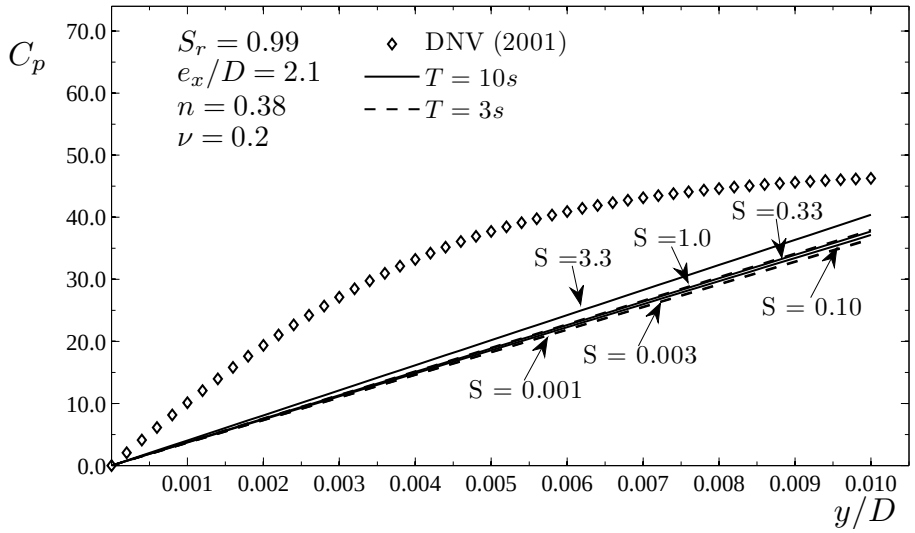

Figure 5.21: *Non-dimensional p-y curves at the depth $z/D = 2$. Flexible pile simulations, foundation depth $e_d/D = 3$, $s = 5.0 \cdot 10^{-4}$, test 25-30.*

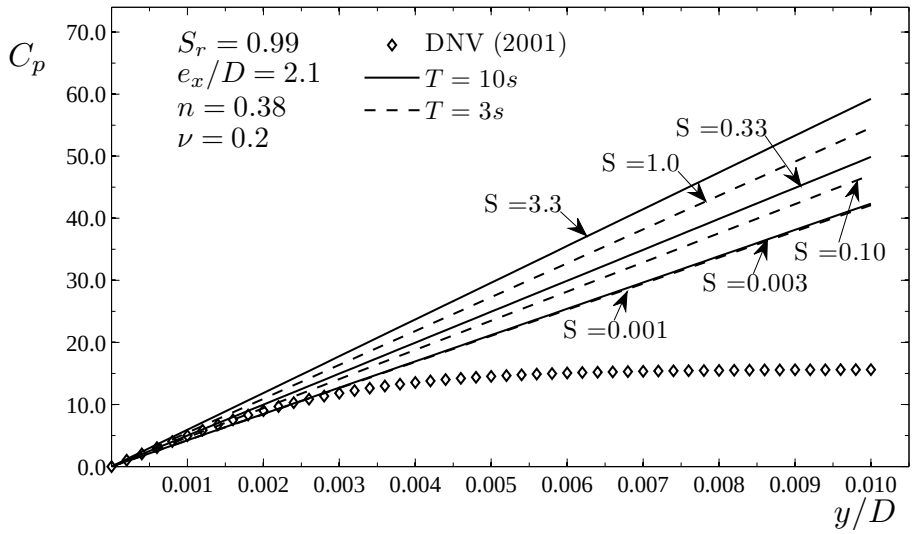

Figure 5.22: *Non-dimensional p-y curves at the depth $z/D = 1$. Flexible pile simulations, foundation depth $e_d/D = 7$, $s = 5.0 \cdot 10^{-4}$, test 31-36.*

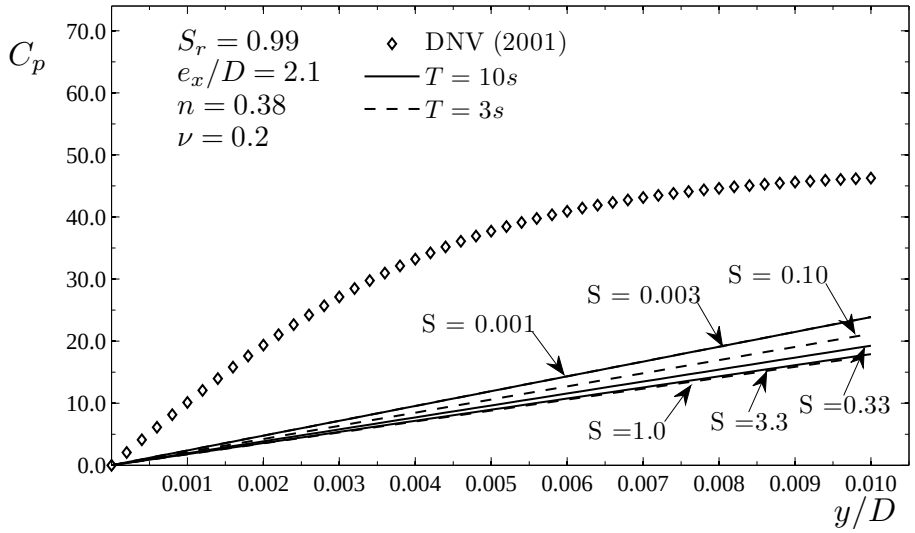

Figure 5.23: *Non-dimensional p-y curves at the depth $z/D = 2$. Flexible pile simulations, foundation depth $e_d/D = 7$, $s = 5.0 \cdot 10^{-4}$, test 31-36.*

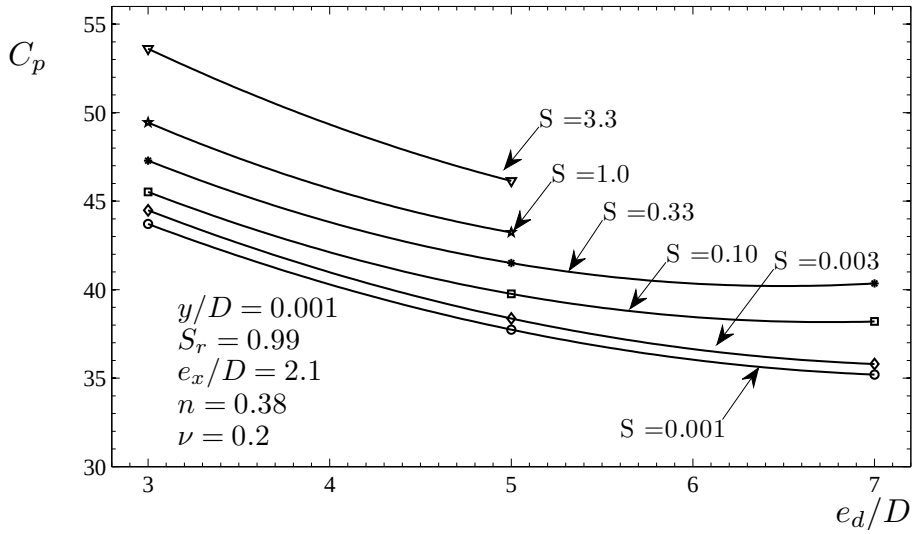

Figure 5.24: *Non-dimensional soil resistance force C_p as function of foundation depth e_d/D at vertical level $z/D = 1$,$s = 3.8 \cdot 10^{-5}$, test $1 - 18$.*

5.8 Reaction Modulus Comparison

This section shortly presents an overview of the reaction modulus obtained in the numerical model, with the reaction modulus obtained from the design recommendations. The reaction modulus was evaluated for a pile displacement y equivalent of 1 % of the pile diameter, see. Eq. 5.16. Tab 5.5 summarizes the reaction modulus obtained in the 36 simulations.

			Present study						DNV
s	e_d/D	z/D	S						
			3.3	1.0	0.33	0.1	0.003	0.001	
$3.8 \cdot 10^{-5}$	5	1	4614	4323	4150	3976	3837	3774	1562
			3.0	**2.8**	**2.7**	**2.5**	**2.5**	**2.4**	
		2	5700	5407	5316	5148	5051	4953	4628
			1.2	**1.2**	**1.1**	**1.1**	**1.1**	**1.1**	
$3.8 \cdot 10^{-5}$	3	1	5361	4943	4729	4552	4448	4371	1562
			3.4	**3.2**	**3.0**	**2.9**	**2.8**	**2.8**	
		2	7317	6777	6615	6248	6176	6006	4628
			1.6	**1.5**	**1.4**	**1.4**	**1.3**	**1.3**	
$3.8 \cdot 10^{-5}$	7	1	0	0	4035	3820	3580	3522	1562
			NA	**NA**	**2.6**	**2.4**	**2.3**	**2.3**	
		2	0	0	4748	4589	4515	4430	4628
			NA	**NA**	**1.0**	**1.0**	**1.0**	**1.0**	
$5.0 \cdot 10^{-4}$	5	1	5283	4922	4572	4404	4123	4105	1562
			3.4	**3.2**	**2.9**	**2.8**	**2.6**	**2.6**	
		2	2048	2026	2215	2289	2495	2455	4628
			0.4	**0.4**	**0.5**	**0.5**	**0.5**	**0.5**	
$5.0 \cdot 10^{-4}$	3	1	5187	4746	4435	4325	4218	4293	1562
			3.3	**3.0**	**2.8**	**2.8**	**2.7**	**2.7**	
		2	4039	3796	3770	3642	3714	3655	4628
			0.9	**0.8**	**0.8**	**0.8**	**0.8**	**0.8**	
$5.0 \cdot 10^{-4}$	7	1	5923	5458	4988	4698	4236	4210	1562
			3.8	**3.5**	**3.2**	**3.0**	**2.7**	**2.7**	
		2	1791	1762	1927	2118	2387	2388	4628
			0.4	**0.4**	**0.4**	**0.5**	**0.5**	**0.5**	

Table 5.5: *Overview of non-dimensional reaction modulus* $(dCp/d(y/D))_{At\ y/D=0.01}$ *compared with DNV (2004). Boldface numbers correspond to the ratio of the present result and the DNV result.*

For the rigid pile experiments ($s = 3.8 \cdot 10^{-5}$) the reaction modulus found are in general higher than predicted by the DNV recommondations. A maximum

ratio $E_{py,num}/E_{py,DNV} = 3.4$ is found. In addition it can be noticed that the reaction modulus is consistant with the change in spreading parameter S. For the flexible pile simulations, the reaction modulus found, for the first 5 m is larger than compared with the DNV. However for a soil depth of 10 m the DNV predicts a more stiff response. It may also be seen, that the reaction modulus in the case of the flexible piles ($s = 5.0 \cdot 10^{-4}$) is only consistant with the spreading parameter S for the first 5 m. For 10 m soil depth no clear relation between the spreading parameter and the reaction modulus is found. The inconsistancy is believed to be related to the rather large bending of the pile. In the flexible pile simulations, most of the PWP generated, is generated in the top soil. As the soil depth increase the effect from the PWP, and therefore the spreading parameter becomes less pronounced.

5.9 Cavitation

During the cyclic motion of the pile, negative PWP is generated. If the total pressure, i.e. the hydrostatic pressure plus the PWP, becomes negative, cavitation occurs and the soil will fail.

Fig. 5.25 depicts the total pressure distribution for test at phase 270° (pile is at its maximum displacement).
From the pressure distribution it can be noticed that cavitation do not occur. It should be noticed that the result presented, correspond the set of soil parameters, in which, the spreading parameter $S = 0.1$. Had cavitation been considered for spreading parameters in the range $S = 0.003 - 0.001$ cavitation would occur. However this range correspond to the case of a seabed composed of a low permeable soil, such as silt ($k = 0.0001$ cm/s).

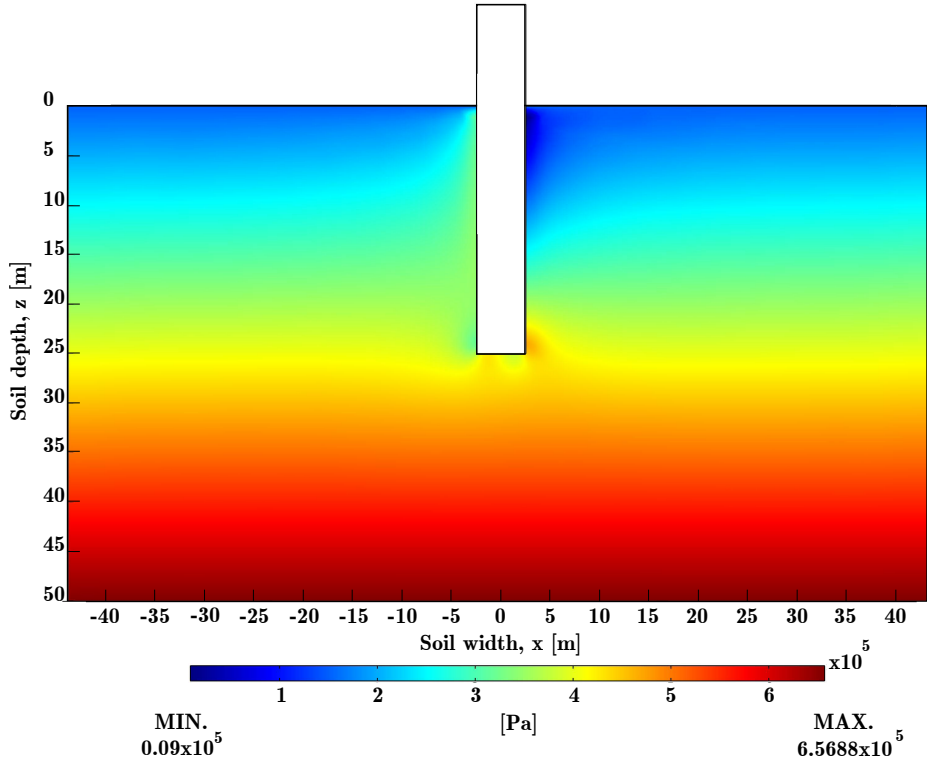

Figure 5.25: *Total pressure distribution, phase* $\omega t = 270°$. *Permeability* $k =$ 0.01 cm/s. *Rigid Pile, test 4.*

Chapter 6

Conclusion

A 3D numerical model was developed to describe the seabed response under cyclic loading of a monopile foundation. The model is based on the Biot consolidation equations, a set of equations that governs the process of soil deformations and the resulting pore-water flow and is therefore able to handle the pore-water pressure generated during the cyclic loading of a pile. The model was developed for field conditions, thus a pile with a diameter of 5 m was simulated.

The model was validated against (1) simplified analytical solutions for the soil response under progressive waves, and (2) against experimental data obtained in a lab scale experiment. The validation exercise showed that the numerical model was able (with some model tuning) to replicate the pore-water pressure (in excess of hydrostatic pressure) measured in the experimental tests for some portion of the pore-water pressure time-series.

The model, validated and tested was used to conduct a parametric study, where the influence of various parameters, including the soil permeability on the soil response was investigated.

Based on the Biot equations and the properties of the pile foundation, a set of non-dimensional parameters, governing the soil response was derived. The familiar soil resistance curves (p-y curves) was derived from the numerical model and presented in non-dimensional form, and the influence of the derived non-dimensional parameters was discussed.

The parametric study showed that, for a given displacement, y, the soil resistance p, increased with increasing S, a non-dimensional parameter responsible for generation and further dissipation of the pore-water pressure. The parametric study also showed that, again for a given y, the soil resistance increased with decreasing bending stiffness of the pile, expressed in terms of a non-dimensional quantity s. Finally, when the non-dimensional foundation

depth decreased, the soil resistance increased,

References

Achmus, M., Kuo, Y.-S., and Abdel-Rahman, K. (2009). Behavior of monopile foundations under cyclic lateral load. *Computers and Geotechnics*, **36**, 725–735.

Bear, J. (1988). *Dynamics of Fluids in Porous Media*. Dover Publications, INC, New York.

Bhattacharya, S., Lombardi, D., and Wood, D. M. (2011). Similitude relationships for physical modelling of monopile-supported offshore wind turbines. *International Journal of Physical Modelling in Geotechnics*, **11**(2), 58–68.

Biot, M. A. (1941). General theory of three-dimensional consolidation. *Journal of Applied Physics*, **12**(2), 155–164.

Broms, B. B. (1964). Lateral resistance of piles in cohesionless soils. *ASCE – Proceedings – Journal of the Soil Mechanics and Foundations Division*, **90**, 123–156.

Budhu, M. and Davies, T. G. (1987). Nonlinear-analysis of laterally loaded piles in cohesionless soils. *Canadian Geotechnical Journal*, **24**(2), 289–296.

Carrier, W. D. (2003). Goodbye, Hazen; Hello, Kozeny-Carman. *Journal of Geotechnical and Geoenvironmental Engineering*, **129**(11). Technical Notes.

Chung, J. and Hulbert, G. M. (1993). Time integration algorithm for structural dynamics with improved numerical dissipation: the generalized-α method. *Journal of Applied Mechanics, Transactions ASME*, **60**(2), 371–375.

Cuéllar, P. (2011). *Pile Foundations for Offshore Wind Turbines: Numerical and Experimental Investigations on the Behaviour under Short- Term and Long-Term Cyclic Loading*. Ph.d-thesis, Technical University of Berlin, Berlin.

DNV (2004). *Offshore Standard DNV-OS-J101 "Design of offshore wind turbine structures"*. Det Norske Veritas.

DNV and Risø (2001). Guidelines for design of wind turbines. Technical report, Det Norske Veritas & Risø.

Dobry, R., Vicente, E., Oroueke, M. J., and Roesset, J. M. (1982). Horizontal stiffness and damping of single piles. *Journal of the Geotechnical Engineering Division-ASCE*, **108**(3), 439–459.

Eskesen, M., Buhrkall, J., and Henningsen, J. (2010). 11761 - laboratoriepraktik. Technical report, Technical Universty Of Denmark, Civil Engineering, Brovej, building 118, DK-2800 Kgs. Lyngby.

European Commission (2008). Memo on the renewable energy and climate change package. Memo.

EWEA (2009). Oceans of opportunity. Technical report, European Wind Energy Association.

Fan, C.-C. and Long, J. H. (2005). Assessment of existing methods for predicting soil response of laterally loaded piles in sand. *Computers and Geotechnics*, **32**.

Fetter, C. W. (2001). *Applied Hydrogeology*. Prentice Hall., Upper Saddle River, New Jersey, 4. international edition.

Fredsøe, J. and Deigaard, R. (2002). *Mechanics of Coastal Sediment Transport*. World Scientific, River Edge,NJ. Advanced series on ocean engineering : 3.

Grashuis, A. J., Dietermann, H. A., and Zorn, N. F. (1990). Calculation of cyclic response of laterally loaded piles. *Computers and Geotechnics*, **10**(4), 287–305.

Hazen, A. (1892). "Some physical properties of sands and gravels, with special reference to their use in filtration.". *24th Annual Rep., Massachusetts State Board of Health*, (Pub. Doc. No. 34), 539–556.

Holeyman, A., Huebner, A., Saal, H., and Tomboy, O. (2006). Comparison of different methods for simulating the behavior of laterally loaded piles. *Proceedings of the sixteenth International Offshore and Polar Engineering Conference*, **2**, 502–509.

Hsu, J. R. C. and Jeng, D. S. (1994). Wave-induced soil response in an unsaturated anisotropic seabed of finite thickness. *International Journal for Numerical and Analytical Methods in Geomechanics*, **18**(11), 785–807.

Hsu, J. R. C., Jeng, D. S., and Tsai, C. P. (1993). Short-crested wave-induced soil response in a porous seabed of infinite thickness. *International Journal for Numerical and Analytical Methods in Geomechanics*, **17**(8), 553–576.

Ibsen, L. B. and Liingaard, M. (2009). Prototype bucket foundation for wind turbines - natural frequency estimation. Technical Report DCE Technical Report No. 9, Aalborg University.

Jeng, D.-S. and Cheng, L. (2000). Wave-induced seabed instability around a buried pipeline in a poro-elastic seabed. *Ocean Engineering*, **27**(2), 127–146.

Jeng, D. S., Zhou, X. L., Luo, X. D., Wang, J., Zhang, J., and Gao, F. P. (2010). Response of porous seabed to dynamic loadings. *Geotechnical Engineering Journal of the SEAGS and AGSSEA*, **41**(4).

Jensen, B. C. (2004). *Teknisk ståbi*. Teknisk Forlag, Århus, 18 edition.

Kim, Y. and Jeong, S. (2011). Analysis of soil resistance on laterally loaded piles based on 3d soil-pile interaction. *Computers and Geotechnics*, **38**(2), 248 – 257.

Lade, P. V. and Nelson, R. B. (1987). Modelling the elastic behaviour of granular materials. *International Journal for Numerical and Analytical Methods in Geomechanics*, **11**(5), 521–542.

Lambe, T. W. and Whitman, R. V. (1969). *Soil Mechanics*. Series in Soil Mechanics. John Wiley and Sons, Inc, New York.

Leblanc, C., Houlsby, G., and Byrne, B. (2010). Response of stiff piles to long term cyclic loading. *Géotechnique*, **60 (2)**, 79–90.

Liu, X. and Garcia, M. H. (2007). Numerical investigation of seabed response under waves with free-surface water flow. *International Journal of Offshore and Polar Engineering*, **17**(2), 97–104.

Madsen, O. S. (1978). Wave-induced pore pressures and effective stresses in a porous bed. *Geotechnique*, **28**(4), 377–393.

Matlock, H. and Reese, L. C. (1960). Generalized solutions for laterally loaded piles. *ASCE – Proceedings – Journal of the Soil Mechanics and Foundations Division*, **86(5)**, 63–91.

DGF Laboratoriekomité (2001). *Laboratoriehåndbogen*. dgf-Bulletin no. 15. Danish Geotechnical Society.

Mei, C. C. and Foda, M. A. (1981). Wave-induced responses in a fluid-filled poro-elastic solid with a free-surface - a boundary-layer theory. *Geophysical Journal of the Royal Astronomical Society*, **66**(3), 597–631.

Ovesen, N. K., Fuglsang, L., and Bagge, G. (2007). *Geoteknik*. Polyteknisk Forlag, 2800 Kgs. Lyngby, 1. edition.

Poulos, H. G. and Hull, T. S. (1989). Role of analytical geomechanics in foundation engineering. TY: GEN.

Press, W. H., Teukolsky, S. A., Vetteling, W. T., and Flannery, B. P. (2007). *"Section 14.9 Savitzky-Golay Smoothing Filters". Numerical Recipes: The Art of Scientific Computin*. Cambridge University Press, New York, 3. edition.

Randolph, M. F. (1981). Response of flexible piles to lateral loading. *Geotechnique*, **31**(2), 247–259.

Reese, L. C. and Impe, W. F. V. (2001). *Single piles and pile groups under lateral loading*. A.A. Balkema, Rotterdam, Netherlands.

Reese, L. C., Cox, W. R., and Koop, F. D. (1974). Analysis of laterally loaded piles in sand. In *Proceedings of the Sixht annual offshore technology conference*, Paper no. 2080, Houston (TX).

Rietdijk, J., Schenkeveld, F. M., Schaminée, P. E. L., and Bezuijen, A. (2010). The drizzle method for sand sample preparation. In P. 6th Int. Conf. on Physical Modelling, editor, *Laue, Springman, Seward*, pages 267–272, London. Taylor and Francis.

Sumer, B. M. (2007). *Lecture Notes On Turbulence*. Technical University of Denmark, DTU Mechanical Engineering, Section for Fluid Mechanics, Coastal and Maritime Engineering.

Sumer, B. M. (2013). *Liquefaction around Marine Structures*. World Scientific, River Edge,NJ. Advanced series on ocean engineering.

Sumer, B. M. and Fredsøe, J. (2002). *The mechanics of scour in the marine environment*. World Scientific, River Edge,NJ. Advanced series on ocean engineering : 17.

Sumer, B. M. and Fredsøe, J. (2006). *Hydrodynamics Around Cylindrical Structures*. World Scientific, River Edge,NJ. Advanced series on ocean engineering : 26.

Sumer, B. M., Fredsøe, J., Christensen, S., and Lind, M. T. (1999). Sinking/floatation of pipelines and other objects in liquefied soil under waves. *Coastal Engineering*, **38**(2), 53–90.

Sumer, B. M., Hatipoglu, F., Fredsøe, J., and Hansen, N.-E. O. (2006a). Critical flotation density of pipelines in soils liquefied by waves and density of liquefied soils. *Journal of Waterway, Port, Coastal and Ocean Engineering*, **132**(4), 252–265.

Sumer, B. M., Hatipoglu, F., Fredsøe, J., and Sumer, S. K. (2006b). The sequence of sediment behaviour during wave-induced liquefaction. *Sedimentology*, **53**(3), 611–629.

Sumer, B. M., Kirca, V. S. ., and Fredsøe, J. (2011). Experimental Validation of a Mathematical Model for Seabed Liquefaction in Waves. *Proceedings of the 21st International Offshore and Polar Engineering Conference, Maui, Hawai, USA, June 19-24*, pages 1010–1018.

Sumer, B. M., Kirca, V. S. ., and Fredsøe, J. (2012). Experimental Validation of a Mathematical Model for Seabed Liquefaction in Waves. *International Journal of Offshore and Polar Engineering*.

Sumer, S. K., Sumer, B. M., Dixen, F. H., and Fredsøe, J. (2008). Pore pressure buildup in the subsoil under a caisson breakwater. *Proceedings of the 18.International Offshore (Ocean) and Polar Engineering Conference, Vancouver, British Columbia, Canada, July 6-11, 2008*, pages 664–671.

Taha, M. R., Abbas, J. M., Shafiqu, Q. S. M., and Chik, Z. H. (2009). The performance of laterally loaded single pile embedded in cohesionless soil with different water level elevation. *Journal of Applied Sciences*, **9**(5), 909–916.

Taiebat, H. A. (1999). *Three Dimensional Liquefaction Analysis of Offshore Foundations*. Ph.d-thesis, The University of Sydney, Sydney.

Terzaghi, K. (1955). Evaluation of coefficients of subgrade reaction. *Geotechnique*, **5**(5), 297–326.

Terzaghi, K., Peck, R. B., and Mesri, G. (1996). *Soil mechanics in engineering practice*. Wiley., New York, 3 edition.

Ulker, M. B. C., Rahman, M. S., and Guddati, M. N. (2012). Breaking wave-induced response and instability of seabed around caisson breakwater. *International Journal for Numerical and Analytical Methods in Geomechanics*, **36**(3), 362–390.

Wittrup, S. (2012). Hesteskohvirvler vasker bunden omkring havvindmøller væk. http://ing.dk/artikel/125792-hestesko-hvirvler-vasker -bunden-omkring-havvindmoeller-vaek. [Online; accessed 19-January-2012].

Yamamoto, T., Koning, H. L., Sellmeijer, H., and Hijum, E. V. (1978). Response of a poro-elastic bed to water-waves. *Journal of Fluid Mechanics*, **87**(JUL), 193–206.

Yang, K. and Liang, R. (2007). Methods for deriving p-y curves from instrumented lateral load tests. *Geotechnical Testing Journal*, **30**(1), 31–38.

Yang, Z. and Jeremic, B. (2002). Numerical analysis of pile behaviour under lateral loads in layered elastic–plastic soils. *International Journal for Numerical and Analytical Methods in Geomechanics*, **26**(14), 1385–1406.

Zania, V. and Hededal, O. (2011). The effect of soil-pile interface behaviour on laterally loaded piles. In *Proceedings of the Thirteenth International Conference on Civil, Structural and Environmental Engineering Computing*, Paper no. 84, Stirlingshire, U. Civil-Comp Press.

Zienkiewicz, O. C., Emson, C., and Bettess, P. (1983). A novel boundary infinite element. *International Journal for Numerical Methods in Engineering*, **19**(3), 393–404.

Appendix A

Additional Data from the Coarse Sand Experiments.

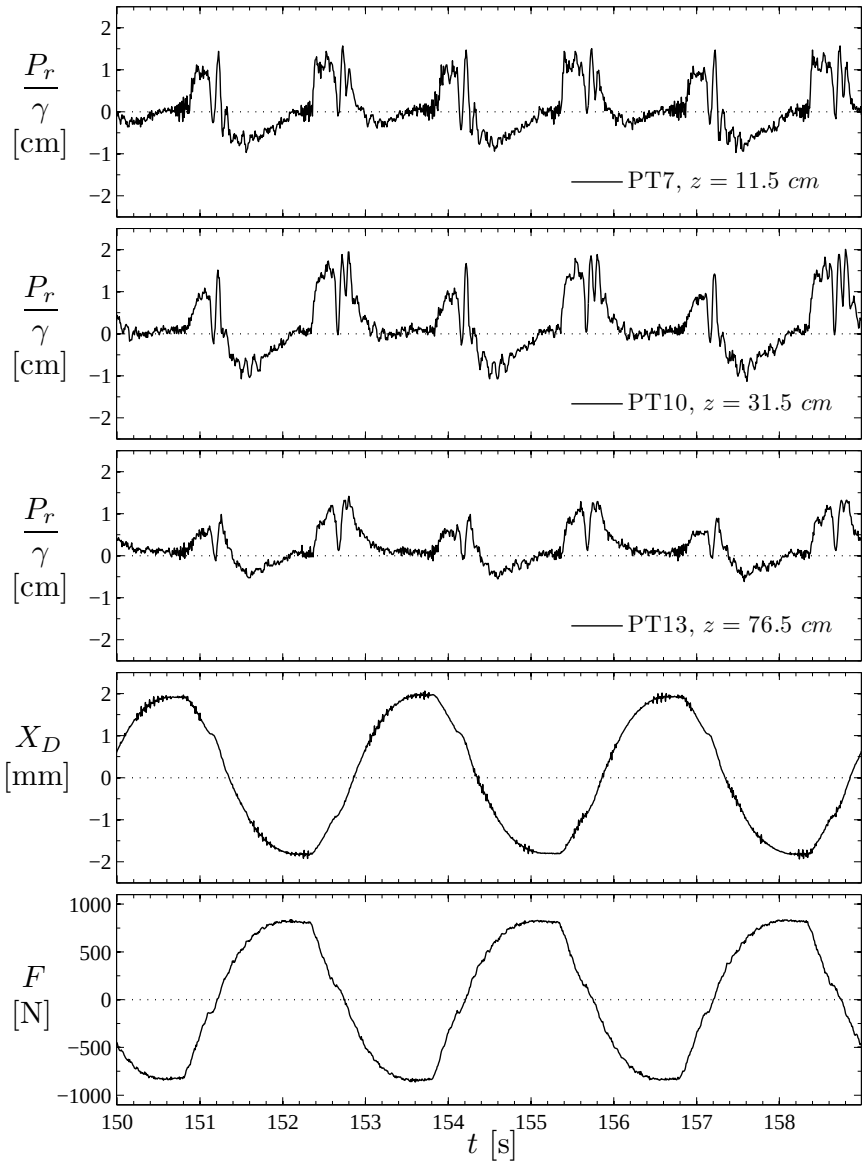

Figure A.1: *Time-series of coarse sand experiment. Unfiltered data, P_r denotes the raw unfiltered PWP time-series.*

Appendix B

Constant Head Permeability Test (Coarse Sand)

B.1 Introduction

The permeability coefficient k is, among others, an important parameter governing the pore-water pressure generated during cyclic deformation of a soil element. One commonly used method in determining the permeability coefficient for saturated sands, is the following empirical formula, (Lambe and Whitman, 1969, pg. 290),

$$k = C_H d_{10}^2 \tag{B.1}$$

where k is the permeability coefficient (cm/s), C_H is Hazen empirical coefficient and d_{10}^2 is the particle size (cm) for which 10% of the soil is finer. Usually the Hazen coefficient C_H is assummed to be 100. However Hazen coefficients ranging from $80 - 200$ for coarse sand have been reported, (Fetter, 2001, pg. 86) and (Terzaghi *et al.*, 1996, pg. 73). Originally the Hazen formula (B.1) included a temperature correction (Hazen (1892)),

$$k = C_H d_{10}^2 \cdot (0.70 + 0.03t) \tag{B.2}$$

where t is the temperature of the water. According to Eq. B.2, the permeability would be 30% greater at 20 °C, than at 10 °C. Usually the temperature correction in Eq. B.2, is ignored in common geotechnical textbooks, Carrier (2003).

The rather large span of Hazen coefficient C_H and the exclusion of the temperature correction, implies the uncertainty of using the Hazen formula in estimating the permeability coefficient. Therefore the permeability coefficient of the coarse sand was determined experimentally.

B.2 Method

B.2.1 Constant Head Permeameter setup

The permeability coefficient for the coarse sand was determined by the constant head permeability test setup (see Fig. B.1). The permeameter used

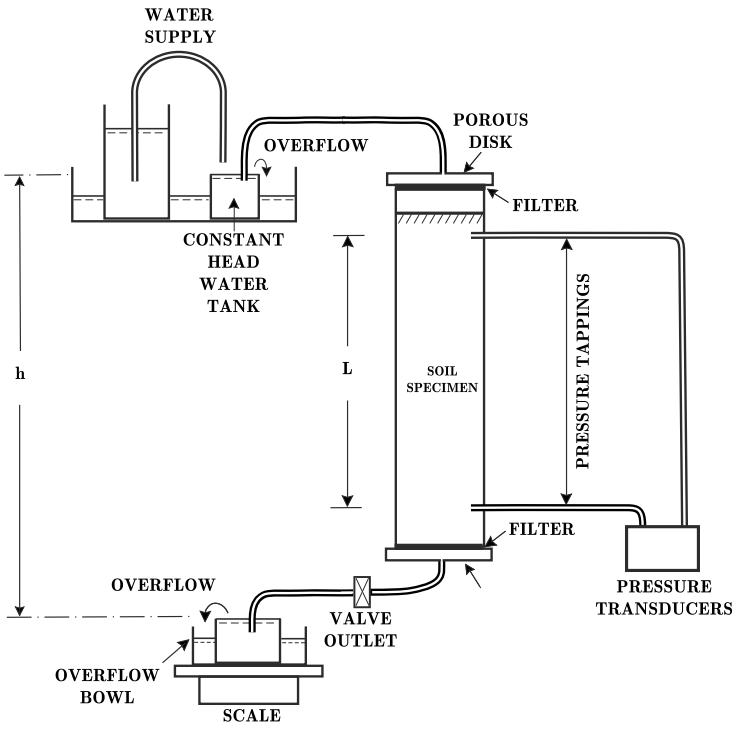

Figure B.1: *Sketch of Constant Head Permeameter setup.*

for the permeability tests consisted of a transparent PVC tube. The inner diameter was 5.35 cm and the height of the permeameter was 40 cm. The bottom of the permeameter was fitted with a porous disk on which a 38 μm filter was placed to prevent movement of the soil particles. A transparent plastic piezometer tube was connected from the bottom disk to an outlet valve. Another piezometer tube was connected from the outlet valve to an overflow bowl placed on a scale. The top of the permeameter was closed by another porous disk. The top disk was connected to a constant head water tank.

To measure the head difference, two pressure tappings were installed 20 cm apart. Transparent plastic piezometer tubes were connecting the pressure tappings and the pressure transducers. The pressure transducers used were of the type Honeywell RS395.

B.2.2 Preparation of Specimens

The permeameter was filled with de-aired demineralised water to the level of the lower most pressure tapping while the outlet valve was open. The outlet valve was then closed and the piezometer tube connecting the pressure tapping and the pressure cell was then filled. A funnel was used to fill the permeameter with sand. The exit of the funnel was held just beneath the water surface. When the second pressure tapping was reached, the tube connecting it to the pressure transducer was filled. Filling the permeameter was then continued until the soil was approximately 2 cm from the top disk. The soil surface was gently levelled off. The permeameter was filled with water and closed with the top disk. The outlet valve was opened and the collecting bowl was raised to a level by which the water started to flow from the bottom and up until inlet tube was filled.

B.2.3 Procedure and Calculation of the Permeability Coefficient

Before starting the permeability tests, the geometric head h between the two bowls was set to 10 cm. The outlet valve was then opened. The time, it took to fill the collecting bowl with 10 g of water, was then recorded. Also, the head difference between the two pressure tappings was recorded. The permeability was then determined by following expression,

$$k = \frac{Q}{t} \cdot \frac{L}{A} \cdot \frac{1}{h} \tag{B.3}$$

where k is the permeability coefficient, Q is the water discharge, t is the total time of discharge, L is the distance between the pressure tappings, A is the cross-sectional area of the soil sample and h is the difference in head. A total of three test for each compaction degree were performed.

B.3 Results and Discussion

Fig. B.2 gives the permeability coefficient k as function of the void ratio e , while Fig. B.3 gives the permeability coefficient as function of the relative density D_r.

With some approximation, the results indicate that the permeability coefficient can be expressed, as a function of the void ratio e and relative density D_r respectively, by following expressions,

$$k = 0.53 \cdot e - 0.009 \text{ cm/s} \tag{B.4}$$

$$k = -0.15 \cdot D_r + 0.45 \text{ cm/s} \tag{B.5}$$

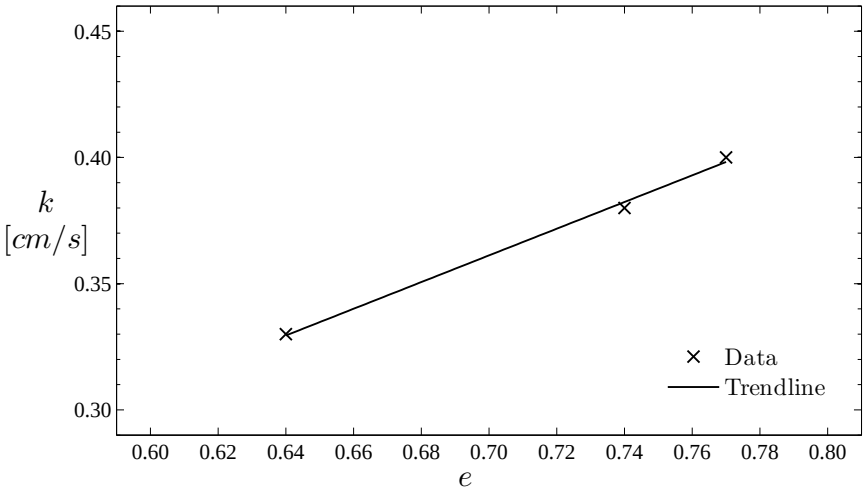

Figure B.2: *Permeability k versus void ratio e.*

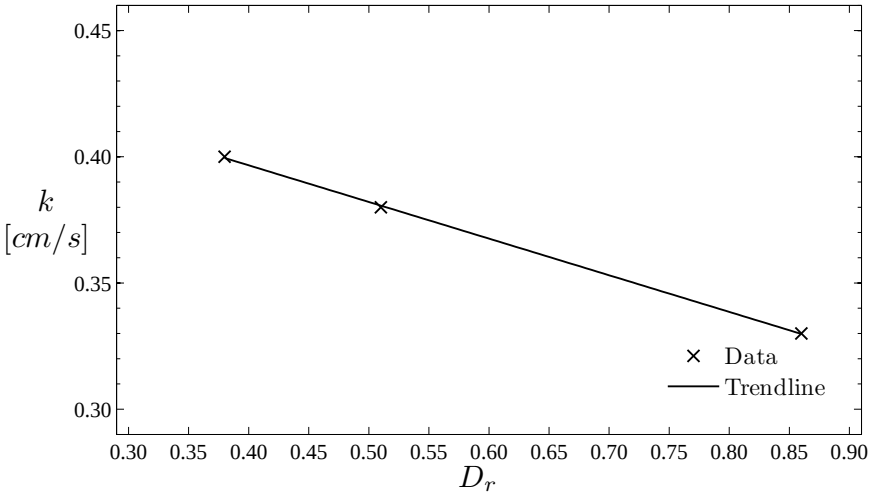

Figure B.3: *Permeability k versus relative density D_r*

The permeability coefficient is seen to vary from 0.33 cm/s to 0.40 cm/s when the soil is in a medium to a very dense condition. The soil may be termed as a high permeable soil according to Lambe and Whitman (1969, pg. 286). Based on an effective grain diameter $d_{10} = 0.05$ cm, the C_H coefficient is in the range $132 - 161$, thus within the range reported by Fetter (2001, pg. 86) and Terzaghi *et al.* (1996, pg. 73).

This page is intentionally left blank.

Appendix C

Soil Sampling - Coarse Silt

As described in Sec. 3.2, the void ratio e (or relative density D_r) for the coarse silt experiments, were determined by conventional soil sampling where the sampler height was 15 cm. This method was therefore only feasible for the first 0 cm - 20 cm. To determine the void ratio for the entire soil column, an acrylic tube with an outer diameter of 50 mm and a wall thickness of 3 mm, was used as sampler. The tube was sharpen in one end. This should ensure a minimum disturbance during penetration.

C.1 Method

When extracting the soil, following procedure was followed: 1) The tube was slowly driven through the soil column. 2) The remaining upper part of the acrylic tube was filled with water. 3) The tube upper end was sealed with a rubber cork. 4) The acrylic tube was slowly extracted from the soil. 5) The lower end of the tube was blocked by a plastic plate the instant the lower end of the tube came to the mudline. 6) The rubber cork was removed and the water was sucked out from the tube. 7) Next, a ruler was taped to the tube. 8) The tube with the plate under it, was then placed in an alu tray. 9) The tube was then slowly lifted from the alu tray, allowing the soil to slide. The soil was cut in chunks of approximately 10 cm in length, each of them placed in a new alu tray. The location for each position of the mudline was noted.

C.2 Results

Before the soil sampling tests, the seabed was prepared, as described in Sec. 3.1.4. Two sets of soil sampling test were conducted. The variation of the relative density as function of soil depth (Fig C.1) reveal "pockets" in the soil column where the soil suddenly become very loose. This is consistent with

the resistance felt, during penetration of the acrylic tube. From the two sets of tests, a mean relative density of $D_r = 0.35$ was found. Overall the seabed may by termed as a medium dense seabed (Lambe and Whitman, 1969, pg. 31).

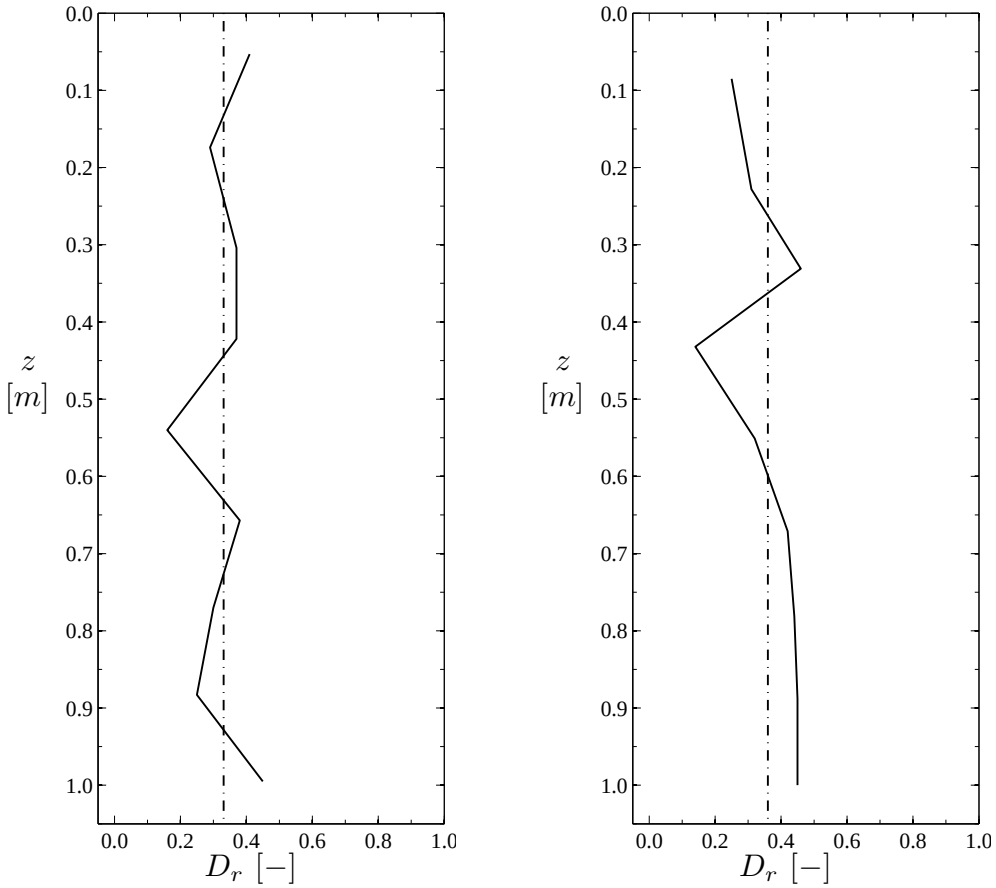

Figure C.1: *The relative density (D_r) as function of soil as function of soil depth z, soil sampling test 1 (left) and soil sampling test 2 (right).*

Appendix D

Strain Gauge Calibration

D.1 Introduction

This chapter describes the method used to calibrate the strain gauges mounted on the pile. To calibrate the strain gauges, a three point bending test was performed.

D.2 Method

The pile was suspended between two rollers (Fig. D.1). One of the rollers were locked, hence the pile acted as a simple supported beam.

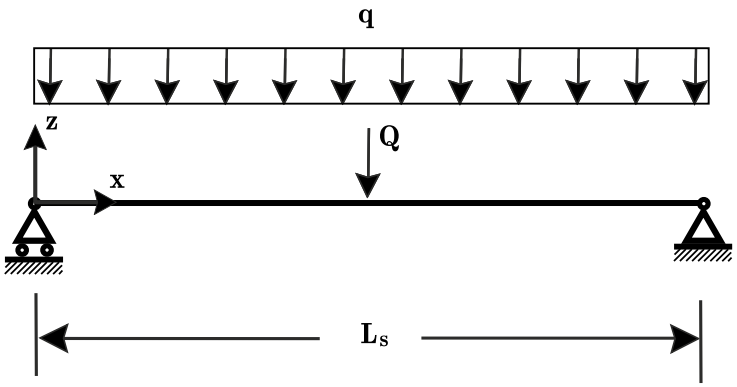

Figure D.1: *Skecth of three point bending test.*

To relate the bending moment in the pile with the output from the strain gauge measurements, the Naviers formula was used,

$$\sigma = \frac{N}{A} - \frac{M}{I}y \tag{D.1}$$

where σ is the normal stress, N is the normal force, A is the cross-sectional area, M being the bending moment, I being the second moment of inertia

and y being the distance from the neutral axis to the point of interest. For a simply supported beam, the normal force $N = 0$. From Hooke's law ($\sigma = E\epsilon$) it can be seen, that there is a linear relation between strain and bending moment,

$$M = -EI\epsilon\frac{1}{y} \tag{D.2}$$

The bending moment of a simply supported beam loaded by a center load is from classical Euler-Bernoulli beam theory expressed as follows (Jensen, 2004, pg. 101),

$$M_C(x) = \frac{1}{2}Qx \qquad for\ x \leq \frac{L_s}{2} \tag{D.3}$$

$$M_C(x) = \frac{1}{2}Q(L_s - x) \quad for\ x \geq \frac{L_s}{2} \tag{D.4}$$

where Q is the load applied in terms of force, L_s being the beam length (the span) and x being the coordinate in the longitudinal direction. Additionally the pile is loaded by an uniform distributed (self weight of the pile) load (Jensen, 2004, pg. 99),

$$M_U(x) = \frac{1}{2}qx(l - x) \tag{D.5}$$

where q is force per unit length. The total moment can be determined from superposition,

$$M_T(x) = M_C(x) + M_U(x) \tag{D.6}$$

The moment distribution along the pile may be calculated by the equations D.3, D.4, D.5 and D.6.

To load the pile with a load Q, concrete stones were laid in a basket hanging under the pile.

D.3 Results

The results from the bending test are shown in Fig D.6. It is noticed that a good relation between moment and measured non-calibrated strain was obtained. Only four out of eight strain gauges were functioning correctly, namely strain gauge B, C, E and F. The calibration plots are given as the relation between applied moment M_{TOT} and voltage strain ε_V. The voltage strain should be considered as voltage converted to strains. However the strains given are not related to the actual strain experienced by the strain gauges.

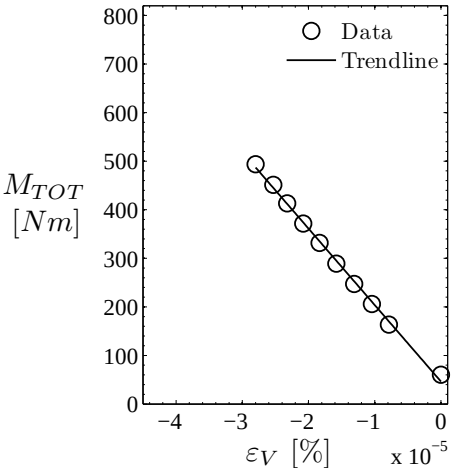

Figure D.2: *Strain gauge B*

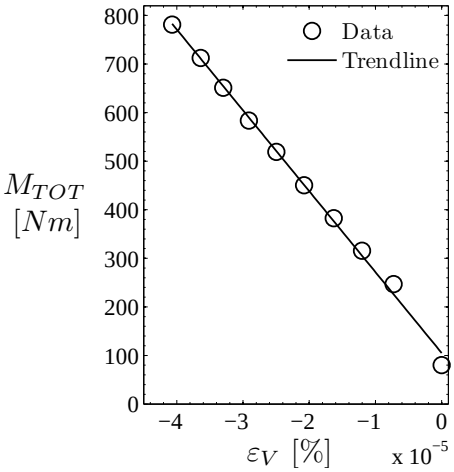

Figure D.3: *Strain gauge C*

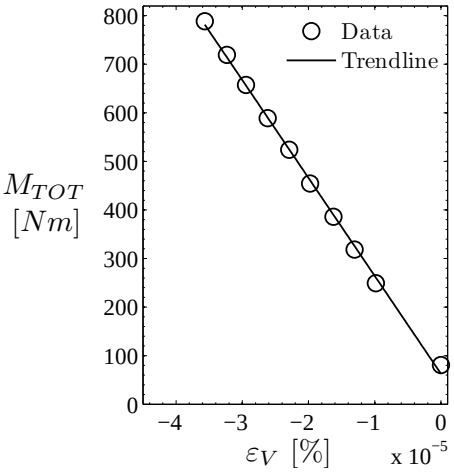

Figure D.4: *Strain gauge E*

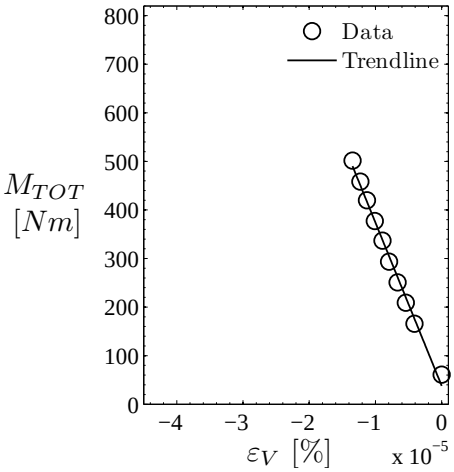

Figure D.5: *Strain gauge F*

Figure D.6: *Plots of the strain gauge calibration from three point bending test.*

This page is intentionally left blank.

Appendix E

Coarse Soil Elastic- and Strength Properties

This chapter provides a description of the method used to determine the coarse soil elastic- and strength properties. Geotechnical textbooks (e.g. Lambe and Whitman (1969)) provide tabulated data for common soil properties, e.g. Young's modulus of elasticity, shear modulus, friction angle, etc. However, the soil properties tabulated are based on a stress condition equivalent to approximately 10 m of soil depth. Since the rocking pile experiments were conducted within a soil depth in the range of 0 m to 1.6 m, the stress field in the experimental tests was significant smaller than the stress field used in the textbooks, thus the soil properties should be determined though an experimental investigation.

E.1 Method

The soil properties were determined through a series of triaxial tests. The tests were performed at DTU Civil Engineering Geotechnics lab facility. The general principles and setup for triaxial testing are described in Lambe and Whitman (1969, pg. 117-119) and will not be given herein. It should be noted that the triaxial tests were performed on tests specimens measuring 7 cm in diameter and 7 cm in height, thus having an aspect ratio of unity.

To achieve a well described soil response in a triaxial test, the test specimen should have a certain strength and stiffness. This means, that there exist a lower limit of confinement pressure, for which the soil specimen can be tested. Therefore a chamber pressure from $15kPa - 100kPa$ was used during the tests. To evaluate the soil properties at small stress levels, a series of relations between the soil properties and confinement pressures should be established.

To establish those relations an extensive number of tests were performed. The test conditions are summarized in Tab. E.1. The triaxial tests were performed as consolidated isotropically drained triaxial tests (CID-tests).

Test number	Chamber pressure $[kPa]$	Relative density [-]
1	25	0.50
2	50	0.50
3	100	0.50
4	25	0.60
5	50	0.60
6	100	0.60
7	25	0.70
8	50	0.70
9	100	0.70
10	15	0.80
11	25	0.80
12	50	0.80
13	100	0.80

Table E.1: *Test conditions for triaxial test on coarse sand.*

E.2 Results

E.2.1 Strength properties

Based on the CID triaxial test, the drained compressive strength was determine as function of the confining pressure (σ_3'). The result is depicted in Fig. E.1. The compressive strength is seen to form a straight line according to the Coulombs failure condition.
The friction angle φ and cohesion c' may be determined by,

$$\sin\varphi = \frac{1}{1+2\tan\beta} \tag{E.1}$$

$$c' = b\tan\beta\tan\varphi \tag{E.2}$$

where b is the intersect between the slope of the failure line and the abscissa and β is the slope of the failure line. The sand appear to be a cohesive material, since the intersect with abscissa is $b \neq 0$. It is not unusual to encounter an effective cohesion of 10 kPa. In the present triaxial test an effective cohesion of 11 kPa is found. However sand is usually considered as a non-cohesive soil (frictional soil) (Ovesen *et al.*, 2007). In the following the friction angle is determined by neglecting the measured cohesion. The friction angles are tabulated in Tab. E.2.
It may be noticed, that the friction angles measured are slightly larger than

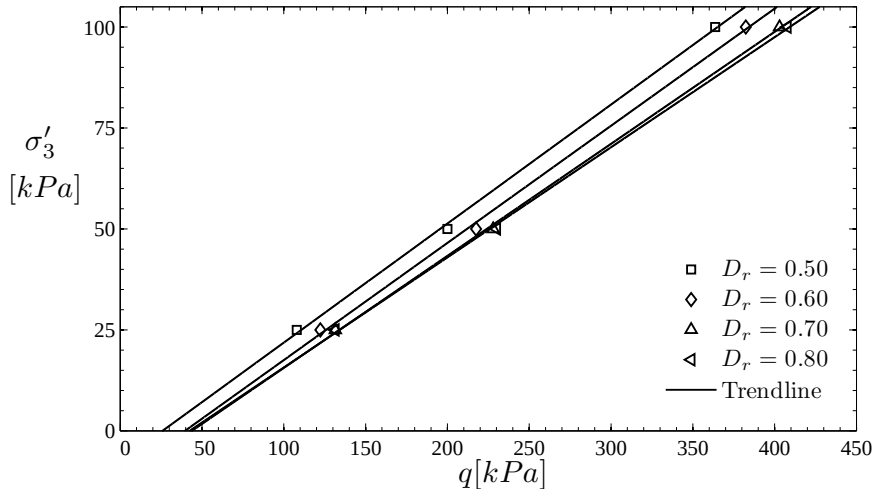

Figure E.1: *Failure condition plotted in a $q - \sigma_3'$-diagram*

Relative density (D_r)	0.50	0.60	0.70	0.80
Friction angle [$^\circ$]	40.3	42.5	44.4	44.7

Table E.2: *Friction angle for coarse sand as function of relative density D_r.*

anticipated (Ovesen *et al.*, 2007, pg. 170). However the maximum friction angle measured, is still less than 45° which is considered as a maximum value in design applications (Ovesen *et al.*, 2007).

E.2.2 Elastic properties

Fig. E.2 shows a typical $\varepsilon_a - q$ relationship from a triaxial test. The effective Young's modulus of elasticity may be evaluated as $E = \Delta q/\Delta\varepsilon_a$ (Secant modulus). In the rocking pile experiments, the soil will experience a loading/unloading sequence. Therefore the Young's modulus was taken as the $E_{URL} = \Delta q/\Delta\varepsilon_a$ during the stage of unloading/reloading.
Fig. E.3 depicts the Young's modulus of elasticity as function of the confinement pressure. From the data it can be concluded that; (1) the Young's modulus for test 2 and test 12 are somewhat larger than the general trend and (2) it appears that the Young's modulus, is to a small degree, dependent on the relative density for the given sand.
It is common practice to express the relationship between Young's modulus of elasticity and confinement pressure with a function similar to that of Lade and Nelson (1987),

$$E = E_{ref} \left(\frac{\sigma_3'}{\sigma_{3,ref}'} \right)^{\alpha} \tag{E.3}$$

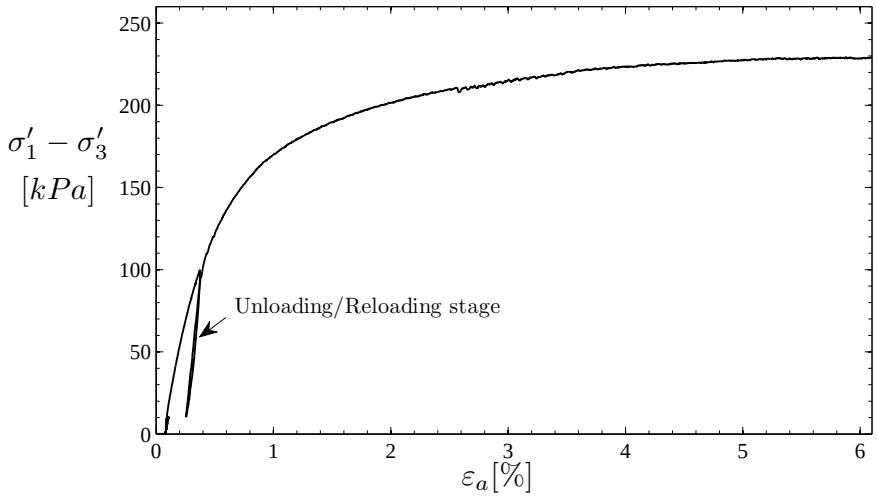

Figure E.2: $\varepsilon_a - q$-*diagram, Relative density* $D_r = 80$ *confinement pressure* $\sigma_3' =$ 50 kPa

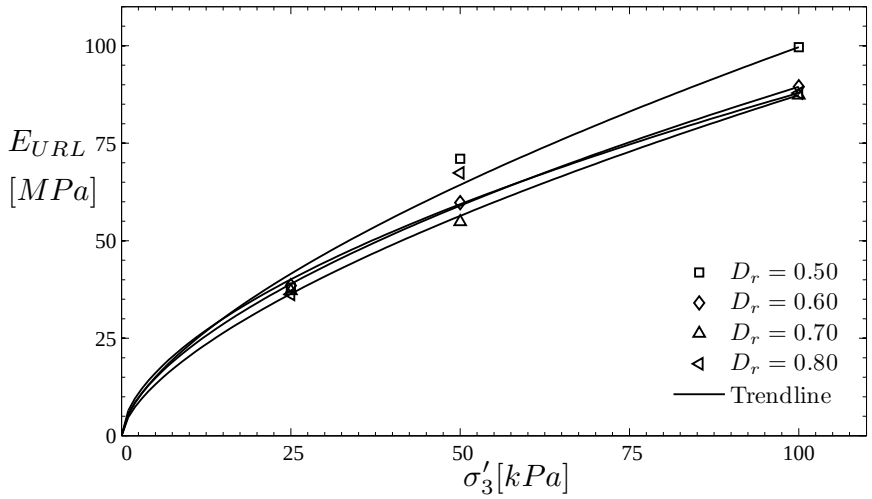

Figure E.3: *Young's modulus of elasticity as function of confinement pressure* σ_3'.

where $\sigma'_{3,ref}$ is a reference confinement pressure used during the triaxial tests and α is a value typically between $0.5 - 0.7$ for sand. Here $\sigma'_{3,ref} = 100$ kPa. The α-value is tabulated in Tab. E.3

Relative density (D_r)	0.50	0.60	0.70	0.80
α-value	0.63	0.60	0.63	0.57
MEAN				0.61

Table E.3: *α-value for coarse sand as function of relative density D_r.*

The averaged Young's modulus (averaged over the relative density) may be expressed as follows;

$$E = 91 \text{ MPa} \left(\frac{\sigma'_3}{100 \text{ kPa}} \right)^{0.61} \tag{E.4}$$

The Poison ratio may be determined by different methods. One method is to determine the shear modulus in a $\varepsilon_q - q$-diagram in which ε_q is the triaxial shear strain and utilize the relation,

$$G = \frac{E}{2(1+\nu)} \tag{E.5}$$

However ε_q is a somewhat uncertain quantity to measure. A more direct method to determine the Poison ratio is to express the Poison ratio as,

$$\nu = -\frac{\Delta\varepsilon_r}{\Delta\varepsilon_a} \tag{E.6}$$

where the change in radial strain $\Delta\varepsilon_r$ can be directly related to the axial strain ε_a and the volume strain ε_p by,

$$\Delta\varepsilon_r = \frac{\Delta\varepsilon_p - \Delta\varepsilon_a}{2} \tag{E.7}$$

Combining the two preceding equations yields,

$$\nu = -\frac{1}{2}\left(1 - \frac{\Delta\varepsilon_p}{\Delta\varepsilon_a}\right) \tag{E.8}$$

From the 13 triaxial tests, a Poison ratio in the range $0.13 - 0.25$ was found. There was no clear tendency between relative density, confinement pressure and the Poison ratio. An average Poison ratio yielded 0.20.

This page is intentionally left blank.

Appendix F

Derivation of Eq. 5.13

Here the derivation of Eq. 5.13 is presented. The bending strain ϵ_p in the monopile is expressed as being a function of the following non-dimensional group,

$$\epsilon_p = f\left(\frac{Qe_x}{E_p D^2 t_w}\right) \tag{F.1}$$

where Q is the lateral load at the pile head, e_x is the load eccentricity, E_p is the pile's Young's modulus, D is the pile diameter and t_w is the wall thickness of the pile. Consider the product $D^2 t_w$. This product related to the area moments of inertia.

The area moments of inertia for a pile is given as,

$$I_p = \alpha(D_1^4 - D_2^4) \tag{F.2}$$

where D_1 and D_2 is the outer and inner diameter of the pile, respectively. Eq. F.2 can be rewritten as,

$$I_p = \alpha(D_1 + D_2)(D_1 - D_2)(D_1^2 + D_2^2) \tag{F.3}$$

A mean diameter D can be defined as,

$$D = \frac{1}{2}(D_1 + D_2) \tag{F.4}$$

The inner diameter D_2 can be expressed as,

$$D_2 = D_1 - 2t_w \tag{F.5}$$

Also the term $(D_1^2 + D_2^2)$ can be written as,

$$D_1^2 + D_2^2 = D_1^2 + D_1^2\left(1 - \frac{2t_w}{D_1}\right)^2 \tag{F.6}$$

Assuming the wall thickness of the monopile being much less than the pile diameter $t_w << D_1$, Eq. F.6 can be written as,

$$D_1^2 + D_2^2 \approx 2D_1^2 \approx 2D^2 \tag{F.7}$$

Inserting Eq. F.4, Eq. F.5 and Eq. F.7 into Eq. F.2 yeilds,

$$I_p = 4\alpha t_w D D^2 = \kappa t_w D D^2 \tag{F.8}$$

where κ is a constant. Neglecting the constant κ and solving for $t_w D^2$,

$$t_w D^2 = \frac{I_p}{D} \tag{F.9}$$

which can be inserted into the non-dimension group (Eq. F.1),

$$\epsilon_p = f\left(\frac{Qe_x D}{E_p I_p}\right) \tag{F.10}$$

from which a non-dimensional parameter (strain parameter) can be expressed as,

$$s = \frac{Qe_x D}{E_p I_p} \tag{F.11}$$

DTU Mechanical Engineering
Section of Coastal, Maritime and Structural Engineering
Technical University of Denmark

Nils Koppels Allé, Bld. 403
DK- 2800 Kgs. Lyngby
Denmark
Phone (+45) 45 25 13 60
Fax (+45) 45 88 43 25
www.mek.dtu.dk

ISBN: 978-87-90416-80-5

DCAMM
Danish Center for Applied Mathematics and Mechanics

Nils Koppels Allé, Bld. 404
DK-2800 Kgs. Lyngby
Denmark
Phone (+45) 4525 4250
Fax (+45) 4593 1475
www.dcamm.dk
ISSN: 0903-1685